High-throughput phenotyping reveals expansive genetic and structural underpinnings of immune variation

Lucie Abeler-Dörner[1,2], Adam G. Laing[1,2,3], Anna Lorenc[1,2,3], Dmitry S. Ushakov[2,3], Simon Clare[4], Anneliese O. Speak[4], Maria A. Duque-Correa[4], Jacqueline K. White[4], Ramiro Ramirez-Solis[4], Namita Saran[2], Katherine R. Bull[5], Belén Morón[6], Jua Iwasaki[7], Philippa R. Barton[8], Susana Caetano[2,4], Keng I. Hng[2], Emma Cambridge[4], Simon Forman[9], Tanya L. Crockford[5,] Mark Griffiths[4], Leanne Kane[4], Katherine Harcourt[4], Cordelia Brandt[4], George Notley[4], Kolawole O. Babalola[10], Jonathan Warren[10], Jeremy C. Mason[10], Amrutha Meeniga[10], Natasha A. Karp[11], David Melvin[4], Eleanor Cawthorne[5], Brian Weinrick[12], Albina Rahim[13], Sibyl Drissler[13], Justin Meskas[13], Alice Yue[13], Markus Lux[13], George X. Song-Zhao[6], Anna Chan[2], Carmen Ballesteros Reviriego[4], Johannes Abeler[15], Heather Wilson[4], Agnieszka Przemska-Kosicka[2], Matthew Edmans[5], Natasha Strevens[4], Markus Pasztorek[2,16], Terrence F. Meehan[10], Fiona Powrie[17], Ryan Brinkman[13,14], Gordon Dougan[4], William Jacobs Jr[12], Clare M. Lloyd[7], Richard J. Cornall[5], Kevin J. Maloy[18], Richard K. Grencis[9], Gillian M. Griffiths[8], David J. Adams[4,19], and Adrian C. Hayday[2,3,19]

[1]These authors contributed equally to this work

[2]Department of Immunobiology, King's College London, London, UK

[3]The Francis Crick Institute, London, UK

[4]Wellcome Sanger Institute, Hinxton, UK

[5]MRC Human Immunology Unit, University of Oxford, Oxford, UK

[6]Sir William Dunn School of Pathology, University of Oxford, Oxford, UK

[7]National Heart and Lung Institute, Imperial College London, London, UK

[8]Cambridge Institute of Medical Research, University of Cambridge, Cambridge, UK

[9] Lydia Becker Institute of Immunology and Inflammation, Wellcome Trust Centre for Cell Matrix Research, School of Biology, Medicine and Health, University of Manchester, UK

[10] European Bioinformatics Institute (EMBL-EBI), European Molecular Biology Laboratory, Hinxton, UK

[11]Data Sciences & Quantitative Biology, Discovery Sciences, R&D Biopharmaceuticals, AstraZeneca, Cambridge, UK

[12]Department of Microbiology and Immunology, Department of Molecular Genetics, Albert Einstein College of Medicine, Bronx, New York, US

[13]Terry Fox Laboratory, British Columbia Cancer Agency, Vancouver, BC, Canada

[14]Department of Bioinformatics, University of British Columbia, Vancouver, BC, Canada
[15]Department of Economics, University of Oxford, Oxford, UK
[16]Department of Biomedical Science, University of Applied Sciences FH Campus Wien, Vienna, Austria
[17]The Kennedy Institute of Rheumatology, University of Oxford, Oxford, UK
[18]Institute of Infection, Immunity & Inflammation, University of Glasgow, Glasgow, UK
[19]co-corresponding authors

ABSTRACT

By developing a high-density murine immunophenotyping platform compatible with high-throughput genetic screening, we have established profound contributions of genetics and structure to immune variation (www.immunophenotype.org). Specifically, high-throughput phenotyping of 530 unique mouse gene knockouts identified 140 monogenic "hits", of which most had no previous immunological association. Furthermore, hits were collectively enriched in genes for which humans show poor tolerance to loss-of-function. The immunophenotyping platform also exposed dense correlation networks linking immune parameters with one another and with specific physiologic traits. Such linkages limit freedom-of-movement for individual immune parameters, thereby imposing genetically regulated "immunological structures", whose integrity was associated with immunocompetence. Hence, we provide an expanded genetic resource and structural perspective for understanding and monitoring immune variation in health and disease.

The increasing implication of immunology in myriad arenas of pathophysiology emphasises the importance of understanding and appropriately measuring inter-individual immune variation. Reflecting this are highly informative studies describing human immune system dynamics[1-4], and investigations of the factors contributing to it[5-8]. Thus, SNP-based and deep sequencing-based Genome-Wide Association Studies (GWAS) and Twin-studies have associated defined genetic loci with autoimmunity and/or immunodeficiency[9-14]. However, it can be challenging to link discrete immunophenotypes to specific genes and/or genetic variants[15]. Conversely, Mendelian trait analysis, that is expanding through genome sequencing of "rare diseases"[16,17], has established concrete links between specific genes and immune function. Nonetheless, this approach can be limited by the infrequency and uncertain clinical annotation of patients, and by practical limitations on phenotypic assays.

At the same time, sex, age, and environmental factors, including diet and the microbiome, make major contributions to human immune variation[5,6,8], but assessing their full impacts is limited by appropriate constraints on interventions, and by human genetic diversity. In sum, immunoregulatory factors seem so numerous and diverse that resolving their individual contributions can seem intractable.

In this regard, animal model studies offer unique opportunities. Specifically, use of an inbred strain limits genetic variation; co-housing reduces microbiome and dietary variation; and age-matching limits physiologic variation. Thus, their study can establish a frame-of-reference for the nature and sources of variation in the "baseline immune system". That frame-of-reference can aid myriad investigations of rodent immunology, and guide the design and interpretation of human immunological studies. Indeed, despite their limitations, gene knockout mouse studies have usefully modelled several human immunopathologies and the actions of many of the most widely prescribed medicines[18]. Superimposed upon this, the use of co-housed, age-matched mice for a genetic screen could offer insight into the fraction and nature of genes whose loss-of-function perturbs the immune system.

To achieve these goals at scale, we have developed a robust, broadly transferrable, high-density, high-throughput Infection and Immunity Immunophenotyping ("3i") platform that has facilitated analysis of the baseline immune system and its response to challenge in aged-

matched, co-housed, isogenic mouse strains collectively mutated in 530 genes (www.immunophenotype.org). Additionally, by integrating 3i into the International Mouse Phenotyping Consortium (IMPC) pipeline (www.mousephenotype.org), immune variation could be related to measures of general physiology. The expansive outputs (>1million data-points) have provided many discrete insights and data-rich resources that collectively build a revised frame-of-reference for viewing immune variation. Moreover, of 530 genes screened, the baseline immunophenotype and/or responses to challenge were affected by mutations in 140 genes (>25% hit-rate), most of which (57%) were never hitherto associated with immunobiology, but which were strikingly enriched in genes for which humans show little tolerance to loss-of-function.

Results

Immunophenotyping of mutant mice at scale

The IMPC aims to obtain and publicly disseminate phenotyping data for mice with targeted disruptions in each of ~18,000 annotated protein-coding genes, generated using either embryonic stem cells generated by the International Knockout Mouse Consortium[19] or CRISPR technology. Although full-gene knockouts do not model most forms of human genetic variation, they can irrefutably implicate defined molecular processes in immunophenotypes, and those phenotypes may be directly related to biallelic human loss-of-function variants, revealed by studies of communities with parental relatedness[20].

Contributing to IMPC, the Wellcome Trust Sanger Institute (WTSI) generated ~3 mutant lines per week. Given this scale, immunological assays were limited to peripheral blood lymphocytometry and responses to *Salmonella* and *Citrobacter* infection[21] (Fig 1a; Supplementary Fig. 1a), potentially missing many immunoregulatory genes. We therefore developed a high-density infection and immunity immunophenotyping platform (3i) compatible with the IMPC high-throughput screen (HTS), that permitted us to assess the proportion and types of genes that may underpin immune variation. Moreover, by integration into IMPC, 3i could relate immunophenotypes to general physiological traits.

At homeostasis, the baseline immune system is simultaneously poised to respond to infectious or toxic challenges and regulated to limit immunopathology. Hence, inter-

individual baseline variation is likely manifest in differential immunocompetence and susceptibilities to autoimmune diseases. To capture this, 3i featured high-content flow cytometry analysis of lymphoid and myeloid cells and their activation states in spleen (SPL), mesenteric lymph nodes (MLN), bone marrow (BM) and peripheral blood (PB) at steady-state (Fig 1a; panels in Supplementary Table 1; populations quantitated in Supplementary Table 2; illustrative gating strategy for MLN T, NKT, and NK cell subsets shown in Supplementary Fig 1b; for other gating, see materials and methods). To sample an extra-lymphoid immune system, quantitative object-based imaging was applied to intraepidermal lymphoid and myeloid cells *in situ* (Supplementary Fig 1c). Anti-nuclear antibodies (ANA) were quantitated, since they commonly reflect impaired immunological tolerance (Supplementary Fig 1d), while effector potential was gauged by measuring SPL CD8 T cell-mediated cytolysis.

All observational assays requiring sacrifice were conducted at the IMPC termination-point of 16 weeks so that they neither diverted tissue from, nor operationally interfered with the basic phenotyping programme. Measuring absolute numbers of cells was largely precluded by IMPC requirements on organ usage, although the focus on percentage representation reflects common practice in immune monitoring[2,3,5]. In parallel, mice were assayed for responses to infection by a parasite (*Trichuris muris*), a virus (influenza), and a bacterium (*Salmonella typhimurium*), and to sodium dextran sulphate (DSS) that causes gut epithelial erosion and microbial translocation (Fig 1a; Supplementary Fig 1e). For each 3i component, experimental standard-operating procedures were established and stringently quality-controlled; instruments were well calibrated; and data reproducibility monitored longitudinally, with automated analysis minimizing any temporal variation (Supplementary Fig 1f). Additionally, and to comply with time and budgetary constraints typical of an HTS, we chose minimum numbers of data-points required to establish significance following application of bespoke statistical analyses (Fig 1a; Supplementary Table 3).

This study represents a five-year phase in which 3i phenotyped knockout strains for 530 genes (Supplementary Table 4). Most strains were nulls or severe hypomorphs of protein-coding genes, whereas 1.8% were lncRNA or miRNA mutants. For ~30% of genes, heterozygotes were screened because homozygotes were embryonically lethal or sub-viable. Of genes selected, 9% had been identified in GWAS screens for inflammatory bowel disease (IBD) or were linked

to infection; some others had GWAS associations to non-immunological traits; and the majority were poorly understood genes, thereby maximising the potential for discovery. Panther Biological Process Gene Ontology showed that relative to the whole genome, the selected genes were neither enriched nor depleted in categories with immunological annotations, a point illustrated by a GO-Slim analysis in which the only categories with low but significant deviation from the whole genome were reproduction and protein modification (Supplementary Fig 1g – indicated by asterisks).

Overall, >1 million data-points were collected from 7 distinct steady-state assay systems applied to 2,100 -10,000 mice (Fig 1a), while additional cohorts of mice were subjected to challenges. Moreover, minimization of technical variation; fastidious control over batch variation, e.g. by spreading phenotyping of each strain over several separate experiments; optimization of data collection and analysis[22]; and innovative data management across heterologous platforms permitted 3i to make rigorous assessments of naturally-arising variation in the baseline immune system of many hundreds of genetically identical, age-matched, co-located, adult C57BL/6N mice, thereby creating a precise backdrop for analyzing mutants.

Immunophenotypic variation among controls

Most steady-state immune cell subsets in adult C57BL/6N controls showed low coefficients of variation (CV), which were further reduced by dynamic automated gating of flow cytometry data, particularly for numerically small cell subsets whose reproducible quantitation can be challenging (Supplementary Fig 1h). Hence, automated gating was adopted screen-wide to obtain the population sizes and CVs described in Fig 1b (see also Materials and Methods)[22]. The screen revealed greater variation for some cell types, including germinal centre (GC) B cells and various αβ and γδ T cell subsets expressing an activation marker, KLRG1 (Fig 1b; bottom-most panel). Activation-driven variation of adaptive subsets was anticipated since non-heritable, antigen receptor gene rearrangements dictate that syngeneic individuals respond differently to shared environments. Nonetheless, effects were highly selective, as evidenced by low CVs of KLRG1$^+$ CD4 T helper cells and of KLRG1$^+$ regulatory T cells (T_{reg} cells) compared to a comparably-sized subset of KLRG1$^+$ CD8 T cells (Fig 1b, compare top and bottom-most panels for subsets denoted with blue arrows).

Compared to most innate immune cell subsets, SPL and PB neutrophils showed relatively high CVs, particularly in males. Indeed, sex was a consistent source of variation for ~50% of PB, SPL, BM, and MLN cell subsets, reflected either in significantly different variance for female (F) and male (M) mice, e.g. for PB neutrophils (Fig 1c; left panel) and displayed broadly in Fig 1b (bottom panel - CV^F, blue circles; CV^M, orange circles), and/or in sexually dimorphic mean-values, e.g. for BM B cell progenitors (Fig 1c; right panel), and displayed broadly in Fig 1b (middle panel; $mean^F/mean^M$ log2-transformed). Considered at scale, the impact of sex was such that principal component analysis (PCA) of 60 aggregated SPL, MLN, BM, and PBL flow cytometry parameters sex-segregated 451 mice with >99% accuracy, with the first two principal components explaining 34% of total variation (Fig 1d).

Several properties of $V\gamma5^+$ dendritic epidermal T cells (DETC) and Langerhans Cells (LC) were also sexually dimorphic, as were ANA outputs, evoking frequent gender imbalances in human autoimmunity (Supplementary Fig 1i)[23]. Conversely, DSS outputs did not segregate by sex, evoking gender-neutral incidences of IBD (Supplementary Fig 1i)[24]. In sum, widespread but highly selective sexual dimorphism characterizes the baseline immune system of adult C57BL/6N mice. As a practical response to this, all statistical tests of 3i data accounted for sex.

Significant correlations of discrete immune parameters

Although the immune system is multi-component, the inter-connectedness of its constituent cell populations is poorly understood. In this regard, the 3i analysis of >650 age-matched, co-located, genetically identical control mice identified significant positive (red) and negative (blue) correlations, as illustrated for 46 steady-state SPL parameters in male and female mice (Fig 2a; Supplementary Fig 2): note, all correlations shown exclude contingent relationships reflecting nested or directly paired technical measurements (see Supplementary Fig 1b; Materials and Methods). Conversely, the strong, negative, steady-state relationship of effector $CD44^+CD62L^-CD8^+$ T cells to naive $CD44^-CD62L^+CD8^+$ T cells is not contingent, since there is a variable population of resting $CD44^+CD62L^+CD8^+$ T cells.

As illustrated by male and female SPL data-sets (Fig 2a, Supplementary Fig 2), correlations included a "lymphoid activation-cluster" embracing effector $CD4^+$, $CD8^+$, NK and $\gamma\delta$ T cells; T_{reg} cells; conventional DC; and plasma cells (Fig 2a, Supplementary Fig 2; central red core). While some such correlations were anticipated, e.g. effector Th with effector T_{reg} cells, others were not, e.g. effector $CD8^+$ T cells correlated positively with plasma cells (Fig 2a, 27 down, 23 across) but negatively with effector NK cells (Fig 2a, 27 down, 9 across). Such relationships may inform the design and monitoring of vaccines aimed at eliciting discrete effector responses.

Other correlations were related to immune homeostasis: thus, higher NK cell representation reflected increases in mature NK cells (Fig 2a, 5 down, 9 across), whereas higher $CD8^+$ T cell representation reflected increases in resting but not effector $CD8^+$ T cells (Fig 2a, 45 down *versus* 46 across or 27 across). Finally, some correlations seemed wholly unexplained; e.g. monocytes positively correlated with B1 B cells, and memory B cells positively correlated with $\gamma\delta$ T cells (Fig 2a, 34 down, 20 across; 18 down, 16 across).

Many correlations were comparable in male and female mice (Fig 2a**;** Supplementary Fig 2; Fig 2b, colorless circles along the 45^o axis), but some were sexually dimorphic, with R values and/or regression slopes being stronger in females (e.g. macrophages *versus* resting NK) or males (e.g. monocytes *versus* neutrophils) (Fig 2b, purple and orange circles, respectively). Whereas the spleen matrices shown are intra-organ, there were also many inter-organ correlations, collectively revealing that the baseline immune system of adult C57BL/6N mice is underpinned by dense, sexually dimorphic networks of >1000 correlations. These may reflect robust intercellular circuitry, such as exists for macrophages and fibroblasts[25].

Integrating immunology with physiology

By coupling 3i to the IMPC, all animals in the observational screen were subject to measures of general physiology (see Fig 1a; Supplementary Fig 1a). As is well established, many physiologic traits are correlated with one another. By limiting the freedom-of-movement of individual parameters, those correlations impose phenotypic structures for female and male mice, reflecting sex-specific physiologies (Supplementary Fig 3a,b). Of note, the correlation network appeared much less dense in females, possibly because its full elucidation was

masked by additional variation arising from sex-specific components, notably oestrous that cycles every 4-5 days[26]. This notwithstanding, core relationships were clearly conserved in females and males, e.g. positive correlations spanning cholesterol (Chol), HDL-cholesterol (HDL), insulin (Ins), and body-weight (Wght), and the relationship of total protein (Tp) to fructosamine (Fruct) which reflects blood protein glycation. Likewise, glucose (Gluc) correlated negatively with chloride (Cl) and sodium (Na). From a practical standpoint, the relatively low inter-individual variability of Na emphasised that prominent correlations did not merely reflect high dynamic ranges of specific parameters.

The more consistent variation of non-immunological parameters in males *versus* females allowed us to identify many highly significant correlations between those parameters and specific immunological parameters, with Chol, HDL, and Na being prominent (Fig 3). Although immunoregulatory roles for metabolic products and processes are well documented[27,28], identified correlations were conspicuously selective, with, for example, no overt immunophenotypic correlations with triglycerides, creatinine, or calcium, but many with red blood cell distribution width (RDW), a common marker of anaemia[29], frequently associated with chronic immune activation[30], and recently shown to predict all-cause mortality in humans[31].

Clearly, significant correlations of immune parameters one with another and with discrete non-immunological traits will limit the freedom-to-vary of any single immune parameter, thereby imposing an immunological structure, as shown for males (Fig 3a). Immunological structure may reflect a balance of immune and non-immunological components that delivers immunocompetence while limiting immunopathology. For females, the sparse correlation network of non-immunological parameters (Supplementary Fig 3b) dictated that the immunological structure was also more sparse, although HDL, RDW and Na were again prominent within it (Fig 3b).

Many diverse genes affect the immunophenotype

The establishment of robust ranges for myriad immune parameters across age-matched, co-located, wild-type mice, coupled with the application of bespoke statistical tests (see Fig 1a; Supplementary Fig 1f; Supplementary Table 3; Materials and Methods) facilitated high-

throughput screening of knockout lines collectively mutated in 530 genes. For steady-state immune parameters, "phenodeviants" ("hits") which exerted monogenic dysregulation of the immunophenotype were called when ≥60% of samples from a strain located outside the 95th percentiles of the wild-type distribution for that parameter.

To further limit batch effects, each mutant strain was assayed on at least two separate occasions, with hits called in a supervised manner; i.e. no data-points were discarded from the dataset, but those possibly attributable to batch effects would not be scored as hits. Effects of temporal data drift in flow-cytometric data were avoided by comparing each knockout mouse to the 70 wild-type mice examined closest in time for any given parameter (Supplementary Table 3). Additionally, there was expert review of raw data for all hits and borderline candidates identified by the statistical pipeline.

False positive rates (FPRs) for each parameter were estimated by randomly sampling sets of wild-type controls in accordance with the real work flow so as to mimic 10,000 different mutant strains, and then assessing their phenodeviance (Supplementary Fig 4a-d). Resulting FPRs were far below observed hit-rates that collectively identified 140 phenodeviants, an overall hit-rate of >25% for genes that *a priori* showed no collective enrichment of immunological GO-annotation (Fig 4; Supplementary Fig 4; see Supplementary Fig 1g). Approximately ~20% of hits were heterozygotes, that collectively accounted for ~30% of the strains analyzed. The relevant code is available at: https://github.com/AnnaLorenc/3i_heatmapping; note that precise hit counts for genes with borderline read-outs may be subject to minor adjustment, based on ongoing analyses and expert review.

Unsurprisingly, hit-rates varied among the assays (Supplementary Fig 5a), and the importance of assaying the same cell populations in different organs was emphasized by the fact that ~50% of flow cytometry hits showed no peripheral blood phenotype (hence would not have scored in IMPC), and of those 36% were unique to spleen, and 39% unique to MLN (Supplementary Fig 5b). Likewise, two thirds of challenge phenodeviants were unique to one pathogen (Supplementary Fig 5b).

Because most phenodeviants scored in only one or few assays, and because overall 3i hit-calling was conservative (Supplementary Table 3), a 25% hit-rate for monogenic effects may have under-estimated the contribution of genetics to immune variation. In short, 3i might have identified more hits if more immunological assays had been performed. For example, no direct assessments of immunological memory were made, and the steady-state gut was not analysed because of interference with IMPC phenotyping. Additionally, although sexually dimorphic trends were apparent for some hits, e.g. TCR$\alpha\beta^+$ CD8 T cell percentages in *Arpc1b*$^{-/-}$ mice; TCR$\alpha\beta^+$ T_{reg} cell percentages in *Setd5*$^{-/-}$ mice; and low TCR$\alpha\beta^+$CD44$^+$CD62L$^-$ effector CD4 cell percentages in male IL-27p28 deficient mice (see www.immunophenotype.org), some sexually dimorphic phenodeviants might not have scored because, other than for PB cytometry and ANA, too few mutant mice were examined. Furthermore, no thorough analysis was made of the genetic impact of non-coding regions.

These considerations notwithstanding, it was conspicuous that the overall hit-rate was largely comparable irrespective of how well-studied genes were, as assessed by PubMed. Specifically, the hit-rate for genes in the lowest quartile of citations (from 0-26) was 23.3%, with the rates for the 3rd, 2nd, and 1st quartiles being 22.5%, 25% and 34%, respectively. This observation, combined with the fact that the genes screened collectively lacked *a priori* enrichment in any immunological annotations, permitted 3i to identify monogenic impacts on the C57BL/6N immune system of 80 genes never hitherto implicated in immunoregulation. Four case-studies, briefly considered below, illustrate the diversity of impacts of different phenodeviants (Figs 5, 6), while all phenodeviants are described at www.immunophenotype.org.

Different classes of genetically regulated immune variation

Nacc2 (Nucleus accumbens-associated protein 2) is a little-studied gene[32] which specifically affected V$\gamma5^+$ DETC numbers (Fig 5a,b), a phenotype hitherto limited to mice mutant for V$\gamma5$ or for *Skint* genes that encode poorly understood, epithelial DETC-selecting elements[33,34]. Thus, the 3i screen identified a novel immune regulator with potential to inform how a prototypic tissue-resident T cell compartment is selected and/or maintained in adulthood. In

this regard, occasional mice scored as harboring wild-type DETC numbers, but those cells had low TCR expression, consistent with incomplete selection[33].

Dph6$^{-/-}$ mice displayed an immune-specific but broad phenotype, with several innate and adaptive cell lineages differing significantly from wild-type (Fig 5a,c). *Dph6* is ubiquitously expressed, encoding one of seven enzymes required for synthesizing diphthamide, a modified histidine residue incorporated into eukaryotic elongation factor 2[35]. However, whereas *Dph1, Dph3* or *Dph4* deficiencies are embryonically lethal[36,37], the 3i phenotype suggested an immune cell-specific, *Dph6*-dependent protein translation system of differential importance in different leukocyte subsets. This evokes growing evidence for immunoregulation by cell type-specific translation[38].

In the third case, the broad phenotypic perturbation of several physiologic traits in *Duoxa2*$^{-/-}$ mice (Fig 6a) was unsurprising, since Duoxa2 contributes critically to iodine utilisation in thyroid hormone synthesis[39]. By contrast, the significant expansions of specific immune cell subsets, particularly CD4^{+} T cells, neutrophils and eosinophils, and the decreased representation of blood Ly6C^{-} monocytes and KLRG1^{+} NK cells in *Duoxa2*$^{-/-}$ mice (Fig 6b) were unanticipated given little prior implication of the gene in immunobiology. Thus, 3i identified a potential immunoregulatory role of *Duoxa2*-dependent endocrine biology.

Finally, *Bach2*$^{-/-}$ mice illustrated how 3i could offer broader insights into a well-established, disease-related gene. *BACH2* deficiencies have been associated with autoimmunity, inflammation, and allergy, commonly attributed to increased effector CD4^{+} and CD8^{+} T cells, as reported in *Bach2*$^{-/-}$ mice[40-44]. However, 3i also identified a greatly expanded range of innate and adaptive immune phenotypes of *Bach2*$^{-/-}$ mice (orange bars in Fig 6c), of which the most significant was a >10-fold increase in KLRG1^{+}CD4^{-} NK cells. Thus, some components of *Bach2*-dependent disease may reflect precocious innate immune cell activation. Moreover, *Bach2*$^{-/-}$ CD8^{+} T cells showed abnormally high cytolytic activity, and most *Bach2*$^{-/-}$ mice were high susceptibility to DSS-colitis (Fig 6d,e).

Genetic regulators of challenge responses

Of 86 phenodeviants affecting steady-state PB, SPL, MLN, BM, CTL, ANA or epidermal phenotypes, ~25% also affected responses to challenges, as judged against wild-type controls assayed contemporaneously (Fig 7a; Supplementary Fig 5b). Once more, those hits included several sparsely-studied genes (Fig 7a, green circles in upper-right quadrant). The fraction of phenodeviants affecting steady-state responses that also affected challenge responses might have been higher if 3i had employed additional challenges and/or assays of response. However, given the breadth of challenges utilized, and the biologically significant post-challenge outcome metrics, including survival and weight-loss, our findings most probably point to greater genetic redundancy in immune function than in baseline immunophenotypes. Indeed, genes affecting challenge outcomes were enriched in those perturbing more than one steady-state parameter (Fig 7a; larger circles are relatively enriched in upper-right *vs* lower-right quadrant). High functional redundancy might ensure that immunocompetence would be resilient to wide-ranging inter-individual variation in baseline immune cell subsets, as characterises humans[1-3]. Finally, some phenodeviants, including many sparsely-studied genes, affected functional responses but not steady-state immune parameters (Fig 7a, upper-left quadrant; Supplementary Fig 5b), possibly because they affect baseline immune parameter(s) not assayed by 3i and/or are expressed by non-immune cells which regulate challenge responses *via* non-immunological mechanisms such as barrier protection.

Given that 57% of the 3i "hits" (80/140) had never hitherto been implicated in immunobiology, and that the others included many little-studied genes, it was striking that hits were collectively enriched in genes for which humans show poor tolerance to "loss-of-function" (LoF). For all human genes assessed by the Genome Aggregation Database (gnomAD) (n=16307), tolerance to LoF is illustrated by "LOEUF": loss-of-function observed/expected upper bound fraction, for which 0 indicates no tolerance of loss-of-function and 2 indicates high tolerance to loss of function (Fig 7b; left panel, red line)[45,46]. We then compared this distribution with that for human orthologues of 3i hits, but first excluded genes with prior GWAS or OMIM classifications that might bias toward low LOEUF values. This notwithstanding, the residual 3i hits (n=77) (Fig 7b; left panel, purple line) showed a significantly different distribution, with conspicuous enrichment for genes with lower LOEUF. This outcome was even more striking when contrasted with human orthologues of 3i

genes without immune phenotypes (n=334) which collectively showed no enrichment for LoF intolerance (Fig 7b; left panel, blue line).

It might be argued that immune hits were biased toward low LOEUF values by genes scored as heterozygotes because the strains were sub-viable. Indeed, LOEUF values were conspicuously low when only heterozygotes were scored for human orthologues of all 3i hits, or for 3i hits minus the OMIM/GWAS genes (as above) (Fig 7b, middle panel, green and purple lines, respectively). Nonetheless, those low-LOEUF-value distributions were significantly displaced from that of human orthologues of 3i heterozygotes that were not immune hits (Fig 7b; middle panel, blue line), strongly arguing that the low LOEUF scores for hits assessed as heterozygotes were not attributable solely to sub-viability but probably also to their immune phenodeviance.

Interestingly, enrichment for low LOEUF was also apparent for human orthologues of genes purely with steady-state flow cytometry phenotypes (p=0.014, Wilcoxon) (Fig 7b; right hand panel, orange *versus* blue lines). Seemingly consistent with this, the 140 immunological phenodeviants were strikingly enriched in genes that also had non-immunological phenotypes (58/140 [>41%]) relative to the genes that were not hits (91/390 [23%]), with almost identical enrichment seen for genes affecting only baseline immune variation (39/86 [>45%]) *versus* those that did not (110/444 [25%]) (Fig 7c).

Genetic regulation of correlation networks

The 3i data-sets were next used to ask whether genes affecting one or more steady-state immune parameter(s) might segregate according to whether they also disrupted correlations connecting immune parameters: i.e. whether they perturbed immunological structure. Fig 8a (left panel) schematises hypothetical distribution clouds of data-points for three phenodeviants (yellow, pink, green) displaying extreme values for cell population B. Of note, whereas gene yellow and gene green maintained proportionality with population A, gene pink broke that correlation.

Real examples of this are shown in Fig 8b: *Gmds* and *Arpc1b* mutants displayed very few NK cells but maintained proportionality with mature NK cells, whereas most *Arhgef1*$^{-/-}$ and

Pclaf1$^{-/-}$ mice sat outside the confidence limits of the relationship, displaying disproportionately high NK maturation. Likewise, *Duxoa2*$^{-/-}$ and *Dph6*$^{-/-}$ mice, whose effector CD4^{+} T cell numbers were atypically low and high, respectively, each preserved an inverse relationship of effector CD4^{+} Th cells and naïve CD8^{+} T cells, whereas this correlation was broken by *Gmds* and *Cog6* deficiencies. Hence, correlations that confer structure on the immune system are differentially resilient to genetic perturbation.

Overall, we observed that genes with the potential to affect $\geq$10 correlates collectively preserved ~75% of intra-organ and inter-organ correlations (Fig 8c; left-hand column, 'Total'). Thus, immunological structure was relatively resilient to genetic perturbation of discrete immune parameters. Nonetheless, mutations of some genes that affected larger numbers of immune parameters disrupted substantially more correlations, as was evident for *Cog6* and *Bach2* (Fig 8c). However, structural perturbation did not simply reflect the greater number of immunophenotypes affected by a gene, since *Dph6*$^{-/-}$ mice displayed a similar number of steady-state immunophenotypes (e.g. altered cell subsets) to *Cog6*$^{-/-}$ mice, but preserved most intra-organ and inter-organ correlations (Fig 8d; compare the density of red lines (broken correlations) *versus* blue lines (preserved correlations) in the spleens of the two strains). This argues that specific genes underpin the existence of certain correlations and hence shape immunological structure. Added to this, *Arpc1b* broke many inter-organ correlations while preserving most intra-organ correlations (Fig 8c), indicating that different genes regulate immune subset relationships in different ways.

Given that many immune parameters also correlated with specific physiologic measures, it was appropriate to ask whether genes with non-immunological phenotypes were more likely to disrupt immunological structure. Indeed, baseline immunological structure seemed much less resilient when discrete physiological traits were perturbed, with such genes collectively breaking significantly more correlations (30%) than did genes only affecting immune parameters (16%) (Fig 8e). Additionally, genes which affected challenge responses as well as the baseline immunophenotype broke significantly more correlations (35%) than genes affecting only the baseline immunophenotype (19%) (Fig 8f). By using cluster-robust standard errors, the results shown in Fig. 8e and 8f were robust *vis-a-vis* different genes contributing to different numbers of correlations, and correlations being underpinned by

additional factors not tested for. Moreover, controlling for the influence of non-immune traits and challenge responses in the same regression analysis confirmed that non-immune and challenge phenotypes made separate contributions. Clearly, the association of defects in immunocompetence with compromises in baseline immunological structure makes a compelling case for assessing and better understanding immune subset correlations as a refined means for monitoring immune variation.

Discussion

3i has provided a community resource in the form of a broadly transferrable, high-throughput platform by which immunophenotypes can be measured in different settings; e.g. comparison of genotypic variants, or pre- and post-treatments. By combining genetic screening and immunophenotyping at scale, 3i has affirmed a substantial contribution of genetics to immunophenotypic variation, and has considerably expanded the number and diversity of genes known to have monogenic impacts on steady-state immune parameters and/or challenge responses. Those genes, most of which lacked prior implication in immunobiology, likely have disease-relevance given their wholly unanticipated enrichment in genes for which humans show poor tolerance to loss-of-function. Moreover, for well-studied genes such as *Bach2*, 3i identified hitherto unrealised endophenotypes that may contribute to disease mechanisms.

Of comparable value to 3i's identification of immunoregulatory genes was the functional implication of pathways on which those genes lie. Complex, multigenic autoimmune pathologies such as systemic lupus erythematosus (SLE) and multiple sclerosis (MS) reflect combined dysfunctions in commonly unelucidated pathways. Germane to 3i, the recent demonstration that causative dysfunction in SLE and MS could be tracked *via* discrete endophenotyes[15] emphasises the value of associating specific genes and pathways to specific endophenotypes. Likewise, relative proportions of murine splenic cell types have proved to be powerful indicators of autoimmune dysregulation[47]. Added to this, the web-based curation of 3i data-sets, comparing hundreds of single-gene ablations on the C57BL/6N background, one the most-widely used animal models, might help predict the outcomes of drug-mediated pathway inhibition[18].

The scale, throughput, and robustness of 3i were also sufficient to provide insight into the nature and scope of immune variation in C57BL/6N mice. For example, whereas sexual dimorphism of immune parameters is well established[48,49], 3i established that its impacts are highly selective. The analysis of immune variation at scale also revealed dense correlation networks of immune parameters with each other and with general physiologic traits. *De facto,* such correlations impose structures constraining immune variation. Although structure was more evident in males, it likely exists in females but in practical terms may be masked by higher variability in general physiology. This notwithstanding, correlations offer insights into physiologic and environmental factors, e.g. diet, that may regulate specific immunophenotypes, and may additionally provide practical surrogate measures of immune status.

While immune correlations and resulting structures will differ in detail across organs, strains and species, they provide a revised framework for viewing immune variation. For example, the co-ordination of immune cell subsets reflected by immunologic structure may confer on the immune system a critical agility to respond to diverse challenges. Thus, structure metrics (e.g. subset ratios *versus* consensus values) might usefully be included in immune-monitoring strategies. Supporting this, *Bach2*, *Cog6* and *Arpc1b*, which were readily scored as disrupting correlations, are strongly associated with human disease[40-42,50-52]. Moreover, therapeutic responsiveness to checkpoint blockade was recently associated with a ratio of $CD8^+$ T cell subtypes, rather than with individual subsets[53]. In parallel, the unanticipated density of correlation networks revealed by 3i makes the case for investigating their biological basis.

Author contributions (in order of appearance as authors):

Conceptualisation: J.K.W., F.P., G.D., W.J., C.M.L., R.J.C., K.J.M., G.M.G., R.K.G., D.J.A., A.C.H. Methodology: L.A.-D., A.G.L., A.L., D.S.U., S.C., A.O.S., N.Sa., M.D.-C., K.R.B., B.M., J.I. P.B., K.I.H., E.C., S.F., T.L.C., B.W., A.R., S.D., J.M., A.Y., M.L., G.X.S.-Z., A.C., R.B., G.D., W.J., C.M.L., R.J.C., K.J.M., G.M.G., R.K.G., D.J.A., A.C.H. Software: A.L., M.G., N.R., N.A.K., D.M., A.R., S.D., J.M., A.Y., M.L., J.A., R.B. Website: L.A.-D., A.L., K.O.B., J.W., J.M., A.T.M., T.M. Validation: L.A.-D., A.G.L., A.L., D.S.U., S.C., A.O.S., N.Sa., M.D., K.R.B., B.M., J.I., P.B., E.C. Formal analysis: L.A.-D., A.G.L., A.L., D.S.U., S.C., A.O.S., N.Sa., M.D.-C., K.R.B., B.M., J.I., P.B., E.C., A.C.H.

Investigation: L.A.-D., A.G.L., D.S.U., S.C., A.O.S., N.Sa., M.D.-C., K.R.B., B.M., J.I., P.B., K.I.H., E.C., S.F., T.L.C., H.W., L.K., K.H., C.B., G.N., E.C., B.W., G.X.S.-Z., A.C., C.B.R., A.P-K., M.E., N.St., M.P. Data curation: L.A.-D, A.L. Writing – original draft: A.C.H. Writing – Review and editing: L.A.-D., A.G.L., A.L., D.S.U., A.O.S., N.Sa, N.A.K., J.A., G.D., R.J.C., G.K.G., R.K.G., D.J.A., A.C.H. Vizualisation: L.A.-D., A.G.L., A.L., A.C.H. Supervision: R.B., G.D., W.J., C.M.L., R.J.C., K.J.M., G.M.G., R.K.G., D.J.A., A.C.H. Project Administration: L.A.-D., J.K.W., S.C., A.O.S., R.R-S., A.C.H. Funding Acquisition: R.B., F.P., G.D., W.J., C.M.L., R.J.C., K.J.M., G.M.G., R.K.G., D.J.A., A.C.H.

Acknowledgements

We thank many colleagues for advice, particularly Drs S. Heck of the Biomedical Research Centre of Guy's and St Thomas' Hospital and King's College London; D. Davies of the Francis Crick Institute; F. Geissmann, J. Strid and O. Sobolev in the early stages of programme planning; and N. Karamanis and K. Hawkins for UX testing of the website. The project was funded by Wellcome Trust grants 100156/Z/12/Z. M.D-C received funding from the European Union's Horizon 2020 research and innovation programme under the Marie Sklodowska-Curie grant agreement No 656347. K.O.B., J.W. and T.M., were supported by the NIH Common Fund [UM1 HG006370]. The development of automated flow analysis in R.B.'s group was supported by Genome BC (SOF152), NSERC, International Society for Advancement of Cytometry Genome Canada, Genome BC (252FLO), the National Institute of general medical sciences (R01GM118417) and CIHR. G.D. was supported by an NIHR grant to the Cambridge Biomedical Centre. W.J. was supported by NIH grant AI026170. C.M.L. is supported by a Wellcome Senior Fellowship in Basic Biomedical Science (107059/Z/15/Z). R.J.C. is a principal investigator of the MRC Human Immunology Unit. K.J.M. is funded by a Wellcome Trust Investigator Award (102972/Z/13/Z). R.K.G. holds a Wellcome Trust Investigator Award Z10661/Z/18/Z and is part of the Wellcome Trust Centre for Cell Matrix Research funded by award Z03128/Z/16/Z. In addition, the project was supported by grants and facilities provided to A.C.H. by the Francis Crick Institute, which receives its core funding from Cancer Research UK (FC001093), the UK Medical Research Council (FC001093), and the Wellcome Trust (FC001093).

References

1. Nakaya, H. I. *et al.* Systems biology of vaccination for seasonal influenza in humans. *Nat. Immunol.* **12,** 786–795 (2011).
2. Sobolev, O. *et al.* Adjuvanted influenza-H1N1 vaccination reveals lymphoid signatures of age-dependent early responses and of clinical adverse events. *Nat. Immunol.* **17,** 204–213 (2016).
3. Tsang, J. S. *et al.* Global Analyses of Human Immune Variation Reveal Baseline Predictors of Postvaccination Responses. *Cell* **157,** 499–513 (2014).
4. Wei, S. C. *et al.* Distinct Cellular Mechanisms Underlie Anti-CTLA-4 and Anti-PD-1 Checkpoint Blockade. *Cell* 1–32 (2017).
5. Brodin, P. *et al.* Variation in the human immune system is largely driven by non-heritable influences. *Cell* **160,** 37–47 (2015).
6. Carr, E. J. *et al.* The cellular composition of the human immune system is shaped by age and cohabitation. *Nat. Immunol.* **17,** 461–468 (2016).
7. Patin, E. *et al.* Natural variation in the parameters of innate immune cells is preferentially driven by genetic factors. *Nat. Immunol.* **19,** 302–314 (2018).
8. Alpert, A. *et al.* A clinically meaningful metric of immune age derived from high-dimensional longitudinal monitoring. *Nat. Med.* 1–34 (2019).
9. Ellinghaus, D. *et al.* Analysis of five chronic inflammatory diseases identifies 27 new associations and highlights disease-specific patterns at shared loci. *Nat. Genet.* **48,** 510–518 (2016).
10. Liu, J. Z. *et al.* Association analyses identify 38 susceptibility loci for inflammatory bowel disease and highlight shared genetic risk across populations. *Nat. Genet.* **47,** 979–986 (2015).
11. Tsoi, L. C. *et al.* Identification of 15 new psoriasis susceptibility loci highlights the role of innate immunity. *Nat. Genet.* **44,** 1341–1348 (2012).
12. Orrù, V. *et al.* Genetic variants regulating immune cell levels in health and disease. *Cell* **155,** 242–256 (2013).
13. Nelms, K. A. & Goodnow, C. C. Genome-wide ENU mutagenesis to reveal immune regulators. *Immunity* **15,** 409–418 (2001).
14. Wang, T. *et al.* Real-time resolution of point mutations that cause phenovariance in mice. *Proc Natl Acad Sci USA* **112,** E440–E449 (2015).
15. Steri, M. *et al.* Overexpression of the Cytokine BAFF and Autoimmunity Risk. *N Engl J Med* **376,** 1615–1626 (2017).
16. Zhang, S.-Y. *et al.* TLR3 deficiency in patients with herpes simplex encephalitis. *Science* **317,** 1522–1527 (2007).
17. Turnbull, C. *et al.* The 100 000 Genomes Project: bringing whole genome sequencing to the NHS. *BMJ* **361,** k1687 (2018).
18. Zambrowicz, B. P. & Sands, A. T. Knockouts model the 100 best-selling drugs—will they model the next 100? *Nat Rev Drug Discov* **2,** 38–51 (2003).
19. Skarnes, W. C. *et al.* A conditional knockout resource for the genome-wide study of mouse gene function. *Nature* **474,** 337–342 (2011).
20. Saleheen, D. *et al.* Human knockouts and phenotypic analysis in a cohort with a high rate of consanguinity. *Nature* **544,** 235–239 (2017).
21. White, J. K. *et al.* Genome-wide generation and systematic phenotyping of knockout mice reveals new roles for many genes. *Cell* **154,** 452–464 (2013).
22. Rahim, A. *et al.* High throughput automated analysis of big flow cytometry data. *Methods* **134-135,** 164–176 (2018).
23. Cooper, G. S. & Stroehla, B. C. The epidemiology of autoimmune diseases.

Autoimmunity Reviews **2,** 119–125 (2003).
24. Ananthakrishnan, A. N. Epidemiology and risk factors for IBD. *Nature Publishing Group* **12,** 205–217 (2015).
25. Zhou, X. *et al.* Circuit Design Features of a Stable Two-Cell System. *Cell* **172,** 744–747.e17 (2018).
26. Byers, S. L., Wiles, M. V., Dunn, S. L. & Taft, R. A. Mouse estrous cycle identification tool and images. *PLoS ONE* **7,** e35538 (2012).
27. Huang, S. C.-C. *et al.* Metabolic Reprogramming Mediated by the mTORC2-IRF4 Signaling Axis Is Essential for Macrophage Alternative Activation. *Immunity* **45,** 817–830 (2016).
28. Kolev, M. *et al.* Complement Regulates Nutrient Influx and Metabolic Reprogramming during Th1 Cell Responses. *Immunity* **42,** 1033–1047 (2015).
29. Salvagno, G. L., Sanchis-Gomar, F., Picanza, A. & Lippi, G. Red blood cell distribution width: A simple parameter with multiple clinical applications. *Crit Rev Clin Lab Sci* **52,** 86–105 (2015).
30. Olumuyiwa-Akeredolu, O.-O. O. & Pretorius, E. Platelet and red blood cell interactions and their role in rheumatoid arthritis. *Rheumatol. Int.* **35,** 1955–1964 (2015).
31. Pilling, L. C., Atkins, J. L., Kuchel, G. A., Ferrucci, L. & Melzer, D. Red cell distribution width and common disease onsets in 240,477 healthy volunteers followed for up to 9 years. *PLoS ONE* **13,** e0203504–12 (2018).
32. Xuan, C. *et al.* RBB, a novel transcription repressor, represses the transcription of HDM2 oncogene. **32,** 3711–3721 (2012).
33. Barbee, S. D. *et al.* Skint-1 is a highly specific, unique selecting component for epidermal T cells. *Proc. Natl. Acad. Sci. U.S.A.* **108,** 3330–3335 (2011).
34. Narita, T., Nitta, T., Nitta, S., Okamura, T. & Takayanagi, H. Mice lacking all of the Skint family genes. *International Immunology* **30,** 301–309 (2018).
35. Liu, S. *et al.* Diphthamide modification on eukaryotic elongation factor 2 is needed to assure fidelity of mRNA translation and mouse development. *Proc. Natl. Acad. Sci. U.S.A.* **109,** 13817–13822 (2012).
36. Chen, C.-M. & Behringer, R. R. Ovca1 regulates cell proliferation, embryonic development, and tumorigenesis. *Genes Dev.* **18,** 320–332 (2004).
37. Liu, S. *et al.* Dph3, a small protein required for diphthamide biosynthesis, is essential in mouse development. *Mol. Cell. Biol.* **26,** 3835–3841 (2006).
38. Jackson, R. *et al.* The translation of non-canonical open reading frames controls mucosal immunity. *Nature* 1–20 (2018).
39. Grasberger, H. & Refetoff, S. Identification of the maturation factor for dual oxidase. Evolution of an eukaryotic operon equivalent. *J. Biol. Chem.* **281,** 18269–18272 (2006).
40. Christodoulou, K. *et al.* Next generation exome sequencing of paediatric inflammatory bowel disease patients identifies rare and novel variants in candidate genes. *Gut* **62,** 977–984 (2013).
41. Cooper, J. D. *et al.* Meta-analysis of genome-wide association study data identifies additional type 1 diabetes risk loci. *Nat. Genet.* **40,** 1399–1401 (2008).
42. Liu, W. *et al.* Identification of BACH2 as a susceptibility gene for Graves' disease in the Chinese Han population based on a three-stage genome-wide association study. *Hum. Genet.* **133,** 661–671 (2014).
43. Roychoudhuri, R. *et al.* BACH2 represses effector programs to stabilize T(reg)-mediated immune homeostasis. *Nature* **498,** 506–510 (2013).

44. Afzali, B. *et al.* BACH2 immunodeficiency illustrates an association between super-enhancers and haploinsufficiency. *Nat. Immunol.* **18,** 813–823 (2017).
45. Lek, M. *et al.* Analysis of protein-coding genetic variation in 60,706 humans. *Nature* **536,** 285–291 (2016).
46. Karczewski, K. J. *et al.* Variation across 141,456 human exomes and genomes reveals the spectrum of loss-of-function intolerance across human protein-coding genes: Supplementary Information. 1–39 (2019).
47. Goltsev, Y. *et al.* Deep Profiling of Mouse Splenic Architecture with CODEX Multiplexed Imaging. *Cell* **174,** 968–981.e15 (2018).
48. Piasecka, B. *et al.* Distinctive roles of age, sex, and genetics in shaping transcriptional variation of human immune responses to microbial challenges. *Proc Natl Acad Sci USA* **115,** E488–E497 (2018).
49. Zalocusky, K. A. *et al.* The 10,000 Immunomes Project: Building a Resource for Human Immunology. *Cell Rep* **25,** 513–522.e3 (2018).
50. Márquez, A. *et al.* A combined large-scale meta-analysis identifies COG6 as a novel shared risk locus for rheumatoid arthritis and systemic lupus erythematosus. *Ann Rheum Dis* **76,** 286–294 (2017).
51. Liu, Y. *et al.* A Genome-Wide Association Study of Psoriasis and Psoriatic Arthritis Identifies New Disease Loci. *PLoS Genet* **4,** e1000041–14 (2008).
52. Kuijpers, T. W. *et al.* Combined immunodeficiency with severe inflammation and allergy caused by ARPC1B deficiency. *J. Allergy Clin. Immunol.* **140,** 273–277.e10 (2017).
53. Sade-Feldman, M. *et al.* Defining T Cell States Associated with Response to Checkpoint Immunotherapy in Melanoma. *Cell* **175,** 998–1013.e20 (2018).

Figure Legends

Figure 1: Variation in immune cell subset composition with sex as a contributory driver

a. Overview of the tests performed by WTSI as part of IMPC (inner circle) and by 3i and WTSI as part of 3i (outer circle).
b. Sexual dimorphism in the immune system: Population sizes as % of CD45 cells (upper panel); sexual dimorphism of mean values of population sizes as log2 fold change (middle panel, female/male); and % coefficient of variation (lower panel) of immune populations in SPL, BM and PB from 16-week old male and female wt C57BL/6N mice (n>500). Blue arrows denote cell subsets mentioned in text. Blue and orange circles in bottom panel denote CV values for female and male mice, respectively. Non adjusted p-values from two-sided Wilcoxon test.
c. Left: Neutrophils from peripheral blood of 16-week old wt C57BL/6N mice (for females n=918 and for males n=913, bars represent means) Right: Hardy fractions A and C from the bone marrow of 16-week old WT C57BL/6N mice (for females n=308, for males n=315, bar represents mean)
d. PCA of cell type frequencies from four tissues (SPL, MLN, BM, PB), 60 subsets, and 451 mice; colour denotes sex.

Figure 2: Correlations exist between immune parameters

a. Heat map represents Pearson correlations of 46 splenic immune cell subsets with each other in wt males (n>230) as determined by flow cytometry. Dark red fields denote strong positive, dark blue fields strong negative correlations between frequencies of spleen immune cell subsets.
b. Correlation differences between males and females. Colour denotes ΔR, the difference between the correlation coefficient R for SPL subsets in male and female wt mice. Black circumferences mark parameter pairs that are significantly sexually dimorphic (see Materials and Methods). Correlation coefficients for male and female mice were derived from data depicted in Fig 2a and Fig S2, respectively.

Figure 3: Correlations between immune and non-immune parameters form a sex-specific network of interactions

Correlations with a Pearson R-value >0.33 and p<0.001 between PBL, SPL, MLN, BM with haematological, clinical blood chemistry, and additional parameters (see **Supplementary Fig 3**) for males (a) and females (b). Circle colours denote organ assayed; red lines denote positive correlations; blue lines, negative correlations (n>180 per sex).

Figure 4: 140 out of 530 genes perturb the immunophenotype

Red, significantly different from wt; blue, not significantly different from wt; white, not performed; grey, insufficient data to make a call. Each cell is coloured red when at least one of parameters within an assay is significant. Methods for determining significance of parameters are parameter-specific (see Materials and Methods and www.immunophenotyping.org).

Figure 5: Examples of genes with specific impacts on the immune system

a. Overview of two genes that display specific immunophenotypes. Colours as in Fig 4. Statistical methods and sample size differ between parameters – see Materials and Methods and www.immunophenotype.org for specific gene/parameter combination of n.

b. Vγ5 DETC in ear epidermis of wt and *Nacc2*$^{-/-}$ mice. The image represents a z-projection of cell outlines produced by image processing in Definiens Developer XD, which were used for quantitative object-based image analysis: blue, Langerhans cells (LC); red, Vγ5^{+} DETC contacting LC; green, Vγ5^{+} DETC not contacting LC. Bottom: cumulative data for *Nacc2*$^{-/-}$ mice (n=4) versus sex-matched wt controls (for females n=330, for males n=340, bar represents mean).

c. Phenotypic abnormalities in Dph6$^{-/-}$ mice. Fold change in immune cell subset proportions between *Dph6*$^{-/-}$ and wt mice across multiple tissues (*Dph6*$^{-/-}$, n=6 for SPL, MLN, BM and n=14 for PBL; wt, n>500 for all parameters).

Figure 6: Examples of genes that impact upon the immune system and physiology

a. Overview of two genes that exhibit broad immunophenotypes. Colours as in Fig 4. Statistical methods and sample size differ between parameters – see Materials and Methods and www.immunophenotype.org for specific gene/parameter combination of n.

b. Phenotypic abnormalities PBL in *Duoxa2*$^{-/-}$ mice . Relative PBL cell subset frequencies for *Duoxa2*$^{-/-}$ (n=11) *versus* wt mice (n>450 per sex for all parameters). Dark and light blue denote wt males and females; red and orange denote *Duoxa2*$^{-/-}$ males and females.

c. Effector cell subsets in *Bach2*$^{-/-}$ mice. Fold-change in SPL cell subset composition in mutant mice (n=6) *versus* wt controls (n=76). Yellow represents significant cellular phenotypes not previously reported, as detected by reference range; dark blue represents significant cellular phenotypes previously reported; light blue represents non-significant differences. KLRG1^{+}CD4^{-} NK cells: 10-fold increase, p=1.1x10^{-9}; reference range combined with Fisher's exact test).

d. Cytotoxic T lymphocytes in *Bach2*$^{-/-}$ mice (n=4) compared to wt controls (212 female and 208 male): grey points represent individual wt mice; red circles represent individual *Bach2*$^{-/-}$ mice.

e. *DSS colitis in Bach2*$^{-/-}$ mice (n=4) compared to wt controls (n=481 female and n=315male): grey points represent individual wt mice; white circles represent wt mean values; blue circles represent individual *Bach2*$^{-/-}$ mice.

Figure 7: Genes affecting baseline immunophenotypes and challenge responses

a. Effected parameters and Pubmed citations per gene. Each bubble represents one gene; size represents the number of immune flow phenotypes detected for that gene; colour represents the extent to which each gene has been reported on, determined by number of Pubmed citations, as of October 2018. Numbers denote the numbers of genes in quadrants of the figure.

b. Tolerance to LOF mutations in human orthologs of 3i genes. Left-hand panel: LOF tolerance scores derived from GnomAD for human orthologs of: 3i genes without hits (blue, n=334); 3i genes with hits OMIM/GWAS genes excluded (purple, n=77), and for all GnomAD genes (red, n=16037). A score of 0 denotes complete intolerance; a score of 2 complete tolerance to loss of function. Wilcoxon test: purple versus red p=0.010; purple versus blue p=0.009. Deciles of all genes marked with vertical grey broken lines. Middle panel: Genes tested in heterozygotes. 3i genes without hits (blue, n=109), 3i genes with hits (green, n=31), 3i genes with hits OMIM/GWAS genes excluded (purple, n=19). Wilcoxon test: purple versus blue p=0.0029; green versus blue p=0.003. Right-

hand panel: Human orthologs of all 3i genes without hits (blue, n=334) *versus* genes with hits in steady state flow cytometry phenotypes but without challenge hits (orange, n=34); orange versus blue p=0.014, Wilcoxon test.

c. Relationship between immune phenotypes and non-immune phenotypes. Each bubble represents one gene; size represents the number of immune flow phenotypes detected for that gene; colour indicates non-immune phenotype. Genes with any immune hit and a non-immune phenotype (orange bubbles among bubbles in top and right bottom quadrants) versus not hit genes (orange bubbles among bubbles in left bottom quadrant); p=0.000072, Fisher exact test. Genes with baseline phenotype change and a non-immune phenotype (orange bubbles among bubbles in right bottom quadrant) versus not hit genes (orange bubbles among bubbles in left quadrants); p= p=0.00021, Fisher exact test.

Figure 8: Phenodeviants preserve or break immunological structures.

a. Schematic illustrating the concept of structural perturbation. The yellow and green genes are theoretical hits in both correlated parameters (Pearson's correlation), and exist as an exaggeration of the normal relationship that exists at steady state (grey dots represent wt mice). The pink gene is also a hit in both parameters, but breaks the correlation by falling outside the blue corridor that represents a 95% prediction confidence interval around the correlation line.

b. Examples of genes that preserve or disrupt immunological structure. Plotted are data frequencies of SPL subsets (indicated on x- and y-axes) as determined by flow cytometry. Data from mutant lines with phenotypes are highlighted in different colours; large dots represent the x/y centroid (mean) values, small dots represent data points for each mouse. Grey data points represent wt mice and mutant mice that are comparable to wt mice for both parameters shown. n=4 for Arhgef1$^{-/-}$, n=5 for Arpc1b$^{-/-}$, n=5 for Gmds$^{-/-}$, n=4 for Pclaf$^{-/-}$.

c. Genes differ in their capacity to break or preserve relationships. Stated in red font are the number of correlations that each cited gene disrupts and in blue font the residual number of correlations that each cited gene preserves, the total being all correlations contributed to by the steady-state parameters that the cited gene affects. These are represented as percentages in the left-hand graph (correlations across organs) and

right-hand graph (correlations within the same organ). Only genes affecting parameters which contribute to >10 correlations are depicted. Statistical significance was determined by two-sided Fisher's exact test in comparison to the data set average (dotted line). Number of correlations above bars, *p<0.05, **p<0.01, ***p<0.001.

d. Examples of genes that either preserve or disrupt many correlations. Plotted are parameters (colour-coded according to cell lineage) in BM, SPL, MLN, and PBL, and the correlations that link them in wt mice (left panel, grey lines) or in *Dph6*$^{-/-}$ mice (middle) or *Cog6*$^{-/-}$ mice (right), in which cases blue and red lines denote correlations that are preserved or broken, respectively.

e. Comparison of correlation breaking in genes that score in non-immune tests and immune tests versus genes that have hits only in immune parameters (Probit regression, $p=2.74*10^{-11}$; $p=7.45*10^{-7}$ when controlling for unequal numbers of correlations per gene; p=0.007 when allowing for any dependencies of correlations within a gene by using cluster-robust standard errors). Numbers of correlations above bars.

f. Comparison of correlation breaking in genes that score in challenge assays and steady-state immune tests versus genes that have hits only in steady-state immune parameters (Probit regression, $p=3.95*10^{-18}$; $p=9.10*10^{-16}$ when controlling for unequal numbers of correlations per gene; p=0.021 when allowing for any dependencies of correlations within a gene by using cluster-robust standard errors). Numbers of correlations above bars. Separate contributions of non-immune and challenge phenotypes: $p= 1.56*10^{-6}$ for non-immune controlling for challenge; $p=2.93*10^{-13}$ for challenge controlling for non-immune.

Materials and Methods

Contact for Reagent and Resource Sharing

All reagents used are listed in Supplementary Table 5. For additional information about reagents and resources, contact Adrian Hayday at adrian.hayday@kcl.ac.uk.

Experimental design

All assays relied on the fastidious application to cells and tissues of intensively piloted, robust, optimised Standard Operating Procedures (SOPs) employing high-resolution, quantitative protocols, whose high reproducibility was monitored over time (e.g. Supplementary Fig 1f).

Mice were randomly allocated to the experimental groups (wt *versus* ko) by Mendelian inheritance. The experimental unit in the study was the individual mouse. For the majority of tests, operators were blinded with regard to the genetic identities of mice. Further detailed experimental design information is captured by a standardized ontology as described[19], and is available from the IMPC portal (www.mousephenotype.org). The steady-state screens integrated within the HTS followed a multi-batch design, in which a baseline set of control data was constantly collected by phenotyping wt mice of both sexes along with mutant mice at least once per week. As soon as mutant mice from the breeding colonies reached appropriate ages, they were issued to the pipeline until sufficient number of males and females of each genotype were assessed. In this way, animals from each mutant strain were tested on two to five days, interspersed throughout experiment duration, rather than within one batch. For advantages and robustness of such design in an HTS see [21,54-56]. The challenge screens implemented a parallel group study design.

Compliant with HTS practice, the numbers of mice examined in each assay were dictated by costs, logistics, and power, with bespoke statistical tests (see below) applied to identify genes (so-called "hits") perturbing defined components of the immune system. Two to seven homozygote mice of each sex per mutant line were assessed per test. If no homozygotes were obtained from $\geq$28 offspring of heterozygote intercrosses, the line was deemed homozygous lethal. Similarly, if <13% of the pups resulting from intercrossing were homozygous, the line

was judged as being homozygous subviable. In either case, heterozygotes were phenotyped. The numbers and sex of animals tested per genotype and assay are summarized in Supplementary Table 3.

Ethical compliance

Mouse use in this study was justified based on their facilitating a large variety of phenotypic tests to be carried out on a sufficient number of individuals in a controlled environment. The care and use of mice in the study was conducted in accordance with UK Home Office regulations, UK Animals (Scientific Procedures) Act of 2013 under two UK Home Office licenses which approved this work (80/2076 and 80/2485) which were reviewed regularly by the WTSI Animal Welfare and Ethical Review Board.

All efforts were made to minimize suffering by considerate housing and husbandry, the details of which are available at the IMPC portal: http://www.mousephenotype.org/about-impc/arrive-guidelines. Animal welfare was assessed routinely for all mice involved. Adult mice were killed by terminal anaesthesia followed by exsanguination, and death was confirmed by either cervical dislocation or cessation of circulation.

Animals

Mice were maintained in a specific pathogen-free unit under a 12-hour light, 12-hour dark cycle with water and food *ad libitum* (Mouse Breeders Diet (LabDiets 5021-3, IPS, Richmond, USA), unless stated otherwise. Mice where housed in Tecniplast Sealsafe 1284L (overall dimensions of caging (L × W × H): 365 × 207 × 140 mm; floor area = 530 cm^2) at a density of 3-5 animals per cage, and provided with a sterilized aspen bedding substrate and cardboard tubes and nestlets for environmental enrichment.

Mutant mouse production

Mice carrying knockout first conditional-ready alleles were generated on a C57BL/6N background using the EUCOMM/KOMP Embryonic Stem (ES) cell resource, with ES quality control and molecular characterization of mutant mouse strains performed as described previously [57]. Upon completion of phenotyping, genotyping was repeated and data were only accepted from mice for which the second genotype was concordant with the original. The

knock-in first strategy first generates mice that still possess the full sequence of the targeted gene, interrupted in a crucial exon by the inserted cassette. These tm1a alleles result in functional knockout lines in most cases, but can carry residual expression of the targeted gene. These tm1a alleles can be converted into unequivocal full knockout tm1b alleles by excising the inserted cassette with the targeted essential exon. Details of alleles used can be found in Skarnes *et al*[19]. All lines are available from www.knockoutmouse.org or mouseinterest@sanger.ac.uk.

Non-immune phenotyping

Non-immune phenotyping (summarized in Supplementary Fig 1a) was conducted as described [21]. Screening for phenotypes in *Citrobacter* infection was replaced by the 3i challenges.

Immunological steady-state phenotyping

Tests conducted in the steady-state (PBL, SPL, MLN, BM, ear epidermis, antinuclear antibodies, cytotoxic T lymphocytes function) were conducted on the same 16-week-old mice that were subject to broad non-immunological phenotyping procedures[21]. Non-fasted mice were terminally anaesthetised using Ketamine (100 mg/kg)/Xylazine (10 mg/kg) injection. Organs were harvested and either analysed directly (PBL) or shipped in HBSS at 4°C for analysis on the same day off-site. Readouts of the respective tests and numbers of mice used are summarized in Supplementary Fig 1 and Supplementary Table 3.

Single cell preparation of immune cells from spleen

After removing the fat, spleens were transferred into Miltenyi C-tubes with 3 ml of enzyme buffer (PBS Ca^{2+}/Mg^{2+}, 2% FCS (v/v), 10 mM HEPES, Collagenase (1 mg/ml), and DNAse (0.1 mg/ml). Samples were then processed using a Miltenyi Gentle MACS dissociator (SPL program 01) and incubated at 37°C for 30 minutes. After the incubation, samples were processed again in the Miltenyi Gentle MACS dissociator (SPL program 02) and the enzyme reaction was stopped adding 300 µl of stop buffer (PBS, 0.1 M EDTA). Samples were filtered through 30 µm filters and centrifuged for 5 minutes at 400 x g at 8°C. The pellet was resuspended in FACS buffer (PBS, Ca^{2-}/Mg^{2-}, 0.5% FCS, EDTA 2mM), incubated for 60 seconds

in RBC lysis buffer and then washed with FACS buffer. Samples were transferred to 96-well V bottom plates and incubated in 50 µl of RBC lysis buffer (eBioscience) for 1 minute prior to antibody staining.

Single cell preparation of immune cells from mesenteric lymph nodes (MLN)

After removing the fat, MLN were transferred into 1.7 ml microfuge tubes with 200 µl of buffer (PBS $Ca^{2+/}Mg^{2+}$, 2% FCS (v/v), 10 mM HEPES) and ruptured using small plastic pestles. 400 µl enzyme buffer (PBS $Ca^{2+/}Mg^{2+}$, 2% FCS (v/v), 10 mM HEPES), Collagenase (1 mg/ml), and DNAse (0.1 mg/ml) were and samples were incubated for 15 minutes at 37°C. The reaction was stopped by adding 60 µl stop buffer (PBS 0.1 M EDTA) and samples filtered through 50 µm filters and centrifuged for 5 minutes at 400 x g at 8°C. The cell pellet was resuspended in FACS buffer (PBS $Ca^{2-/}Mg^{2-}$, 0.5% FCS, EDTA 2 mM) and transferred to 96-well V bottom plates for antibody staining.

Single cell preparation of immune cells from bone marrow (BM)

The tibia was cleared of muscle tissue and cut below the knee and above the ankle. The open bone was placed into a cut pipette tip placed into a microfuge tube, thereby keeping the bone away from the bottom of the tube and allowing the bone marrow to be centrifuged out of the bone at 1000 $\times$ g for 1 minute. The bone was discarded and the pellet resuspended in 50 µl RBC lysis buffer at room temperature for 1 minute. Cells were washed in 200 µl FACS buffer and again centrifuged at 1000 $\times$ g for 1 minute. Cells were resuspended in 400 µl FACS buffer and transferred to 96-well V bottom plates for antibody staining.

Blood preparation

Blood was collected into EDTA coated tubes (peripheral blood leukocytes assay) *via* the retro-orbital sinus. Whole blood for peripheral blood leukocyte assays was stained with two titrated cocktails of antibodies (Supplementary Table 1). Using the white blood cell count obtained from the haematological analysis, absolute cell counts were derived for each population and reported as cells/µl.

Immunophenotyping by flow cytometry

Single cell suspensions were incubated with Fc-block for 10 minutes at room temperature, washed four times, first with FACS buffer and then with PBS, and then incubated with live/dead ZiR dye (BioLegend) for 10 minutes at room temperature. Samples were washed again with FACS buffer and incubated with antibody cocktails (see Supplementary Table 1) at 4°C for 20 minutes. Samples were washed twice with FACS buffer and measured on a BD Fortessa X-20 equipped with 405 nm, 488 nm 561 nm and 644 nm lasers (see Supplementary Table 1). Full details of instrument setup are available at www.immunophenotyping.org. Panels were modified slightly in summer 2014 in order to better correspond to the IMPC panels (T cell panel: 9th June 2014, B cell panel: 15th September 2014). Data before and after this data split were analysed separately. Data were analysed with FACSDiva and Flowjo software. FCS files are available from flowrepository.org.

Flow cytometry quantification (SPL, MLN and BM)

Additionally to the manual gating performed at the time of data acquisition, collected flow cytometry data for SPL, MLN and BM were gated computationally using flowClean, UFO, and flowDensity[22,58]. FlowClean was used to perform acquisition-based quality checking to remove anomalous events. Files with fewer than 20,000 events were then removed from further analysis. UFO was used to identify outlier samples (e.g., batch effects). FlowDensity was used to enumerate cell populations by automating a predefined gating approach using sequential, supervised bivariate gating analysis to set the best cut-off for an individual marker using characteristics of the density distribution. The parameters for each individual cell population were pre-defined once for all files. The automated analysis data was validated against matched manually analysed data. Gating strategies are outlined in Supplementary Fig 1b and in Supplementary Fig 6). Assessment of absolute cell counts were not compatible with the high-throughput workflow employed in the study for SPL, MLN and BM. All cell subset frequencies are presented as a percentages of a relevant parent populations.

Ear epidermis immunophenotyping

Epidermal sheets from mouse ears were treated with hair removal cream (Nair) for 4 minutes at room temperature. After removing the cream by extensive washing in PBS, ears were split

into dorsal and ventral sides and incubated dermal side down for 35 minutes at 37°C in 0.5 M ammonium thiocyanate (Sigma-Aldrich). Epidermal sheets were gently peeled from the dermis in PBS, and fixed in cold acetone for 20 minutes at -20°C. After washing in PBS, epidermal sheets were incubated for 1 hour at room temperature with 5% (wt/vol) FCS in PBS and were stained for 1 hour at 37°C with Vγ5 TCR-FITC (clone 536; BD), MHCII-AF647 (I-A/IE; BioLegend) and CD45-eFluor450 (eBioscience). Epidermal sheets were washed extensively in PBS and mounted on slides with ProLong Gold antifade medium (Life Signalling Technologies). Leica SP2 or SP5 confocal microscopes equipped with 40 x 1.25 NA oil immersion lens and 405 nm, 488 nm and 633 nm lasers were used to record 1024 x 1024 pixel confocal z-stacks with Leica Acquisition Software. The confocal records were processed and quantified with Definiens Developer XD^{R} software using a custom-made automated protocol where images were smoothed with a sliding window Gaussian pixel filter, segmented by an automated Otsu's method and then filtered based on object size and morphology parameters to detect cells in each fluorescence channel. Further, in order to quantify the number and length of dendrites, the detected cells were skeletonised in 3D to determine the points where dendrites start to branch out of the cell body. Mean of 3 vision fields was used for quantification.

Antinuclear Antibody Immunophenotyping

Murine serum samples were obtained and stored at -20**°**C prior to analysis (after dilution 1:100 in PBS) by incubating on commercially-sourced substrate slides (A. Menarini Diagnostics Ltd.) coated with HEp-2 cells for 30 minutes at room temperature in a humidifying tray. Samples were removed and slides were washed twice with PBS for 5 minutes and once with water for 5 seconds. Slides were incubated with FITC-conjugated goat anti-mouse IgG, diluted 1:500 and incubated for 20 minutes at room temperature in a humidifying tray in the dark. The secondary antibody was removed and slides washed twice with PBS for 5 minutes and once with water for 5 seconds, both in the dark. Slides were mounted in medium and stored at 4**°**C prior to imaging for 400 ms at 20 x magnification in the GFP channel on a Nikon wide-field TE2000U Microscope or a Deltavision Elite widefield system based on an Olympus microscope. Images were subject to multi-parametric analysis in Fiji. Samples were scored from 0-4 according to intensity based on control samples and commercially sourced FITC QC

beads. Samples scored ≥2 were marked as ANA positive. All sera flagged by automated image analysis as putative positives *vis-à-vis* a contemporaneous standard were manually cross-checked for *bona fide* nuclear localization before scoring.

Cytotoxic T Lymphocyte Immunophenotyping

Mouse splenocytes were isolated using 70 μM cell strainers (BD Plastipak) and cultured in T cell media (TCM: 500 ml RPMI, 500 μl B-ME, 5 ml NaPyr, 5 ml pen/strep, 5 ml L-glut, 50 ml 10% heat inactivated FCS and 100 μl IL-2) on 6-well plates pre-coated with 0.5 μg/ml anti-CD3ε antibody and 1 μg/ml anti-CD28 antibody (1.7×10^6 cells/well) for 48 hours. Plates were washed and cells where cultured for a further 8 days with daily passage prior CTL assay.

Cytotoxicity assays were performed using a CytoTox96 Non-Radioactive Cytotoxicity Assay kit (Promega UK Ltd). Cells were washed and re-suspended in killing assay media (KAM: 500 ml RPMI-phenol red, 10 ml 10% heat inactivated FCS and 5ml pen/strep), with CTLs at a concentration of 0.1×10^6 and P815 target cells at a concentration of 0.1×10^6. Purified hamster anti-mouse CD3ε antibody was added to P815 target cells.

P815 cells were added to a serial dilution of CTL samples and incubated for 3 hours. Lysis buffer (Promega UK Ltd.) was added to control samples and incubated for 45 minutes. Supernatants were harvested and substrate mix (Promega UK Ltd) was added prior to a 30-minute incubation in the dark. Stop solution (Promega Corporation UK Ltd) was added to halt the reaction and results acquired using a spectrophotometer (VersaMax, molecular devices).

Flow cytometric analysis was performed to assess the percentage of $CD4^+$ and $CD8^+$ cells within the cell culture. The cell suspension was washed in FACS buffer and the cell pellet re-suspended in a staining master mix (FACS buffer solution + 1:200 anti-CD8α APC and 1:200 anti-CD4 PE). Tubes were then incubated in the dark for 7 minutes at room temperature before the antibody was washed off and cells resuspended in FACS buffer. Results were acquired on a FACS Calibur machine and analysed using FlowJo 10 software.

Challenge screens

Challenge screens were conducted on separate cohorts of mice from the same breeding colony used for the steady-state screens.

DSS colitis challenge

Colitis was induced by adding 1.5% (w/v) DSS (Affymetrix, Inc.) to drinking water for 7 days, followed by 3 days with regular drinking water, in animals aged between 5 and 18 weeks (mean age 9 weeks). Mice were weighed every day and culled if weight loss reached 20% of starting weight.

For histological assessment of intestinal inflammation, mice were sacrificed at day 10 by cervical dislocation, and samples from mid and distal colon taken. Tissue sections were fixed in buffered 10% formalin; paraffin-embedded; cut; and stained with haematoxylin and eosin. Colon histopathology was blind-graded semi-quantitatively on a scale from zero to three, for four criteria: (1) degree of epithelial hyperplasia/damage and goblet cell depletion, (2) leukocyte infiltration in lamina propria, (3) area of tissue affected, and (4) presence of markers of severe inflammation, including crypt abscesses, submucosal inflammation, and oedema. Scores for individual criteria were added for an overall inflammation score of between zero and twelve for each sample. Scores from mid and distal colon were then averaged to obtain inflammation scores for each mouse colon.

Salmonella typhimurium challenge

Groups of 8 mutant and 8 C57BL/6N wild type mice were challenged intravenously with 5×10^5 colony forming units (cfu) *Salmonella typhimurium* M525 :: TetC, (Fragment C of tetanus toxin, to act as an antigen for subsequent antibody quantification), and followed for 28 days. On day 14 post-infection (pi), four mutant and four wt mice were sacrificed by cervical dislocation and organs (spleen, liver and caecum) removed. A small piece of spleen and liver was fixed in 4% formalin and then later processed to paraffin blocks as an infected tissue biobank. The rest of the organs were weighed then homogenized, serially diluted and plated to determine viable bacterial load. At day 28 pi, the remaining four mice were culled

by cardiac puncture under terminal anesthesia and organs removed and processed, as above. The blood was allowed to clot, then centrifuged, serum collected and used to detect TetC antigen specific antibodies by enzyme-linked immunosorbent assay (ELISA). Mice were weighed and monitored daily for signs of pathophysiology.

Influenza challenge

Mutant and wt mice (5-21 weeks of age) were lightly anesthetised and intranasally inoculated with 171 or 227 p.f.u. of A/X-31 (H3N2) influenza in 50 μl of sterile PBS. Mouse weight was recorded daily and the percent reduction was calculated from their weight on day 0. Mice were sacrificed by cervical dislocation on day 10 pi, and the area under the curve from day 0 to 9 pi was calculated. Mice exceeding 25% total weight loss were culled in accordance with UK Home Office guidelines.

Trichuris muris challenge

The Edinburgh (E) strain of *Trichuris muris* was used in all experiments. Female mice (6-12 weeks old) were orally infected with 400 embryonated eggs. Mice were culled by cervical dislocation at day 32 pi, blood was collected by cardiac puncture for serum recovery, and caecum/proximal colon was dissected to inspect for worm presence by stereomicroscope. Levels of parasite-specific serum IgG1 and IgG2a Ab were by ELISA: briefly, ELISA plates were coated with *T. muris* excretory/secretory (E/S) antigen at 5 μg/ml. Serum was diluted 1/40, and parasite-specific IgG1, IgG2a and IgE detected with biotinylated anti-mouse IgG1 (Biorad), biotinylated anti-mouse IgG2a (BD PharMingen), and anti-mouse IgE (BioLegend), respectively. To generate *T. muris* E/S antigen, live adult worms were incubated at 37°C for 24 hours in RPMI-1640 medium (Gibco, UK) supplemented with 500 U/ml penicillin, 500 μg/ml streptomycin and 2 mM L-glutamine (all Gibco, UK). Supernatants were removed, centrifuged at 2000 x g for 15 minutes, filtered through a 0.22 μm filter (Millipore, UK), concentrated using a 10 kD molecular weight cut off Centriprep concentrator (Amicon, UK) and dialysed against PBS over a 24-hour period. The supernatant was subsequently filtered again and protein concentration determined before use.

Statistical analysis

Sample sizes for each experimental group are included in the figure legends and Supplementary Table 3. Measures were taken from distinct animals in almost all experiments. Exceptions are body weight, where the weight of the same animal was recorded repeatedly during the course of the experiment and the CTL assay, in which T cells from the same culture were used for different effector : target ratios. Tests for all assays are listed in Supplementary Table 3. Reference-range tests which require no assumptions were used for most assays. Adjustments for multiple comparisons were not made unless stated in test description, as individual comparisons were not independent (e.g. percentages for different cell types determined by flow cytometry are often nested and dependent on each other). Low false positive rates were instead ensured by using conservative reference range cut-offs and monitoring false positive rates by simulation (Supplementary Fig 4). All tests used were two-sided. Co-variates were included in the analysis indirectly, by dividing animals into sex-specific groups or matching ko and wt by assay date/weight/age (MMR analysis described below) and in the analysis presented in figures 8e and 8f where covariates tested are described in the text. A description of statistical parameters is included into the figure legends. Effect sizes are given when fold change between sexes was analysed. All significant calls and borderline candidates were manually reviewed by biological experts.

Experimental batch effects were minimised by the experimental design, the statistical analysis and by expert review. Experimental set-up: Mice were phenotyped on at least two different days and typically three to four different days. Statistical analysis: Stringent reference range hit calling required $\geq$60% of samples to be in the upper 2.5% or lower 2.5% of the wt distribution. The influence of temporal drift in flowcytometric data was minimized by using as controls only the 70 wt mice that were closest in time for any given parameter. Reference ranges have been shown by the WTSI team to be stable for $\geq$60 mice. Expert review: Experts reviewed all hits and borderline candidates and excluded candidates that suffered from batch effects despite the measures taken above.

Coefficient of variation (CV) was estimated as a ratio of the standard deviation of the wt population to its mean (for both sexes together, unless indicated otherwise). Note that since

a data-set is expressed as frequency of parent, it is bound and CV estimates are less accurate close to the boundary.

Sexual dimorphism

Significance of sex as a source of variation in wt animals was tested in a mixed model (sex as explanatory variable, assay date as a random effect) by examining the contribution of sex to the model and whether the variance was homogeneous between sexes[59]. The effect of multiple testing was managed with Bonferroni correction to control the family-wise error rate to 5%. For Principal Component Analysis and Linear discriminant analysis (LDA), only wt samples with a complete set of flow parameters were used. Data was scaled. Accuracy of classification by sex in LDA was checked with leave-one-out cross-validation.

Estimation of false positive rates

A mutant mouse line was mimicked by randomly selecting N wt animals (N depending on the screen) and assessed whether it would be called a hit using the RR approach. To reflect the data structure and address the potentially confounding batch effect of test days, the number of experimental days from which animals were drawn and their sex was set according to the distributions observed across all tested mutant lines. For example, in the lab, bone marrow was collected on five different days in 36% of mouse strains; in 38% on four different dates; in 11% from three different days, etc. When strains were tested on four assay days, in 78% of cases females were tested on two days, etc. The same data structure was imposed on the draws for the false positive rates. Thereupon, the same rubric used for calling hits from real data was applied, except that the expert data review step (see above) was replaced by filtering out samples from the days when the median of wt animals and non-significant mutant strain samples was further than two median absolute deviations (MADs) from the overall median in wt animals. 10,000 draws were performed for each parameter to determine the rate at which false positives would occur.

Correlation analysis

Pearson correlations between parameters in the flow cytometry screens as well as between the flow cytometry screens and non-immune screens were identified in wt mice for pairwise complete observations, accumulated throughout whole duration of the experiment.

Correlations with parent and sister populations were excluded from the dataset. Correlations with $R>0.33$ and $p<0.0001$ were considered significant.

Comparison of correlations between male and female mice

R values of all significant correlations were compared with a t-test after Fisher z-transformation. Difference in dependence between parameters between sexes (slope of regression line) was tested by fitting a linear regression model to correlated parameters and assessing significance of interaction between sex and predictor variable. P-values were adjusted for multiple testing with Bonferroni correction to control the family wise error rate to 5%.

Immunological structure analysis

Starting from parameters that were affected in a mutant strain, a list was compiled of other parameters with which the affected parameter was ordinarily correlated. The wt C57BL/6N data were then used to predict a value for the correlated parameter in the mutant strain by sex-specific linear regression. If ≥60% of mice for a given mutant strain had predicted values outside the 95% confidence interval based on the wt distribution, the mutant line was defined as breaking this specific parameter correlation. Note that a single perturbed parameter could contribute more than one correlation to the dataset. For the purpose of this analysis, it was assumed that all correlations were equally likely to be broken. To assess if breaking of correlations was correlated with other characteristics, such as a non-immune phenotype or a challenge phenotype, a multivariate Probit regression analysis was undertaken. The same analysis was also used to control for unequal numbers of correlations per gene, allowing for dependencies of correlations within a gene by cluster-robust standard errors and for separate contributions of all characteristics tested. The analysis was carried out using R, RStudio and R packages ggplot2, data.table, dplyr and igraph, org.Mm.eg.db and org.Hs.eg.db.

GnomAD, OMIM and GWAS analyses

If homo-and heterozygotes were analysed from the same strain, only homozygotes were included in this analysis. Human orthologues were based on JAX definition (http://www.informatics.jax.org, accessed 05.05.2016) and only 1:1 human-mouse

orthologues were used. GnomAD scores were extracted from release 2 (gs://gnomad-public/release/2.1/ht/constraint/constraint.ht)[46].

OMIM annotations were obtained on 31 May 2017, with immune-related OMIM-listed genes considered as those implicated in phenotypes of immunodeficiency, recurrent infections, autoimmunity.

GWAS associations were obtained from the full NHGRI-EBI GWAS catalog database 78 on September 10, 2017 (file gwas_catalog_v1.0.1-associations_e89_r2017-07-31.tsv). In GWAS annotation, "immune-related" genes were considered as those mapping to susceptibility to autoimmune disease (systemic lupus erythematosus, psoriasis, rheumatoid arthritis, Sjögren syndrome, primary biliary cholangitis, ulcerative colitis, inflammatory bowel disease, Crohn's disease, multiple sclerosis, type 1 diabetes, Graves' disease, late-onset myasthenia gravis); immune response to virus (measured by secreted TNF-alpha); and functional units of gut microbiota.

Gene overrepresentation analysis

Enrichment analysis was performed with PANTHER Overrepresentation Test with the tool version 14.1 (Released 2019-03-12, www.pantherdb.org)[60]. We calculated significance of over- and underrepresentation of GO-slim Biological Process categories among 466/530 genes with available GO annotation, by Fisher's Exact test and with FDR multiple testing correction. Only categories with more than one gene expected in our dataset and less than 1000 genes in the mouse genome were included.

Data and Code Availability

The flow cytometry files that support the findings of this study are available from www.flowrepository.org with the identifiers listed below:

3i PBMC panel 1: FR-FCM-ZYPJ

3i PBMC panel 2: FR-FCM-ZYPK

3i T-cell Spleen IMPC: FR-FCM-ZYX9

3i T-cell MLN IMPC: FR-FCM-ZYXB

3i B-cell Spleen IMPC: FR-FCM-ZYXC

3i B-cell MLN IMPC: FR-FCM-ZYXE

3i M-cell Spleen IMPC: FR-FCM-ZYXF

3i M-cell MLN IMPC: FR-FCM-ZYXG

3i P2 SPL IMPC: FR-FCM-ZYXN

3i BM IMPC: FR-FCM-ZYXQ

Vignettes showing gating of affected cell populations in KO mice and controls are available for all phenotypes deemed significant in this study in flow cytometry assays through www.mousephenotype.org (access through Associated Images on a gene page).

Microscopy image files from ear epidermis assay, ANA assay and DSS histology are available from the corresponding author upon request and are submitted to www.mousephenotype.org (access through Associated Images on a gene page).

All assay results on mouse and strain level that support the findings of this study are available through http://www.immunophenotype.org (website entirely devoted to this project) and www.mousephenotype.org (access via gene name).

Figures with associated raw data are:

1bcd, 2AB,3ab, 5bc, 6bcde, 7abc, 8cef,S1eghi, S2, S3ab, S4abcd. Supporting data is in Source data files and also available from https://github.com/AnnaLorenc/3i_heatmapping.

Code used for initial hit calling and preprocessed per-mouse data for flow cytometry, ear epidermis and DSS assays are available from https://github.com/AnnaLorenc/3i_heatmapping.

The PhenStat R package used for Influenza analysis is available on Bioconductor (www.bioconductor.org). The ImageJ macro and the Python code used to score ANA positivity, the Definiens Developer code to assess the ear epidermis images and the R code used to assess the false positive rate are available on request.

Material Availability

All mouse lines analysed in this work are available from repositories linked to the International Mouse Phenotyping Consortium (www.mousephenotype.org) or from WTSI (email mouseinterest@sanger.ac.uk). Cell lines are available upon request.

Methods References

54. Karp, N. A. *et al.* Applying the ARRIVE Guidelines to an In Vivo Database. *PLoS Biol.* **13,** e1002151 (2015).
55. Karp, N. A., Melvin, D., Sanger Mouse Genetics Project & Mott, R. F. Robust and Sensitive Analysis of Mouse Knockout Phenotypes. *PLoS ONE* **7,** e52410–11 (2012).
56. Karp, N. A. *et al.* Impact of Temporal Variation on Design and Analysis of Mouse Knockout Phenotyping Studies. *PLoS ONE* **9,** e111239–10 (2014).
57. Ryder, E. *et al.* Molecular characterization of mutant mouse strains generated from the EUCOMM/KOMP-CSD ES cell resource. *Mamm. Genome* **24,** 286–294 (2013).
58. Malek, M. *et al.* flowDensity: reproducing manual gating of flow cytometry data by automated density-based cell population identification. *Bioinformatics* **31,** 606–607 (2015).
59. Mason, J. *et al.* Prevalence of sexual dimorphism in mammalian phenotypic traits. *Nat Commun* **8,** 1–12 (2017).
60. Mi, H., Muruganujan, A., Ebert, D., Huang, X. & Thomas, P. D. PANTHER version 14: more genomes, a new PANTHER GO-slim and improvements in enrichment analysis tools. *Nucleic Acids Res.* **47,** D419–D426 (2018).
61. Kurbatova, N., Mason, J. C., Morgan, H., Meehan, T. F. & Karp, N. A. PhenStat: A Tool Kit for Standardized Analysis of High Throughput Phenotypic Data. *PLoS ONE* **10,** e0131274 (2015).
62. Osorio, F. G. *et al.* Splicing-directed therapy in a new mouse model of human accelerated aging. *Sci Transl Med* **3,** 106ra107–106ra107 (2011).

Figure 1

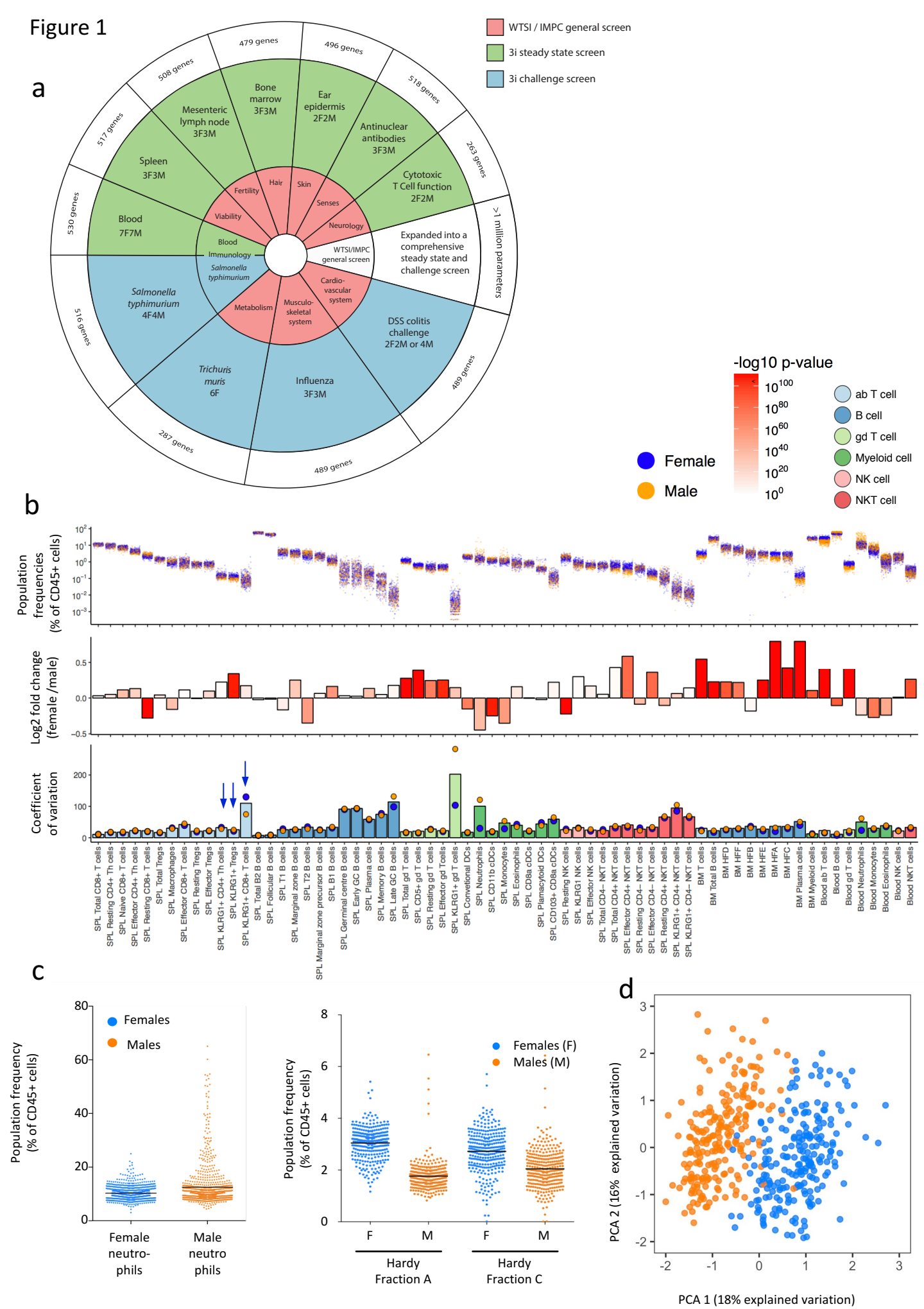
a
WTSI / IMPC general screen
3i steady state screen
3i challenge screen
479 genes
496 genes
508 genes
518 genes
517 genes
263 genes
530 genes
>1 million parameters
516 genes
489 genes
287 genes
489 genes
Bone marrow 3F3M
Ear epidermis 2F2M
Mesenteric lymph node 3F3M
Antinuclear antibodies 3F3M
Spleen 3F3M
Cytotoxic T Cell function 2F2M
Blood 7F7M
Expanded into a comprehensive steady state and challenge screen
Salmonella typhimurium 4F4M
DSS colitis challenge 2F2M or 4M
Trichuris muris 6F
Influenza 3F3M
Fertility
Hair
Skin
Viability
Senses
Neurology
Blood Immunology
Salmonella typhimurium
WTSI/IMPC general screen
Metabolism
Musculo-skeletal system
Cardio-vascular system
-log10 p-value
Female
Male
ab T cell
B cell
gd T cell
Myeloid cell
NK cell
NKT cell
b
Population frequencies (% of CD45+ cells)
Log2 fold change (female /male)
Coefficient of variation
c
Population frequency (% of CD45+ cells)
Females
Males
Female neutro-phils
Male neutro phils
Females (F)
Males (M)
Hardy Fraction A
Hardy Fraction C
d
PCA 2 (16% explained variation)
PCA 1 (18% explained variation)

Figure 2

a Males

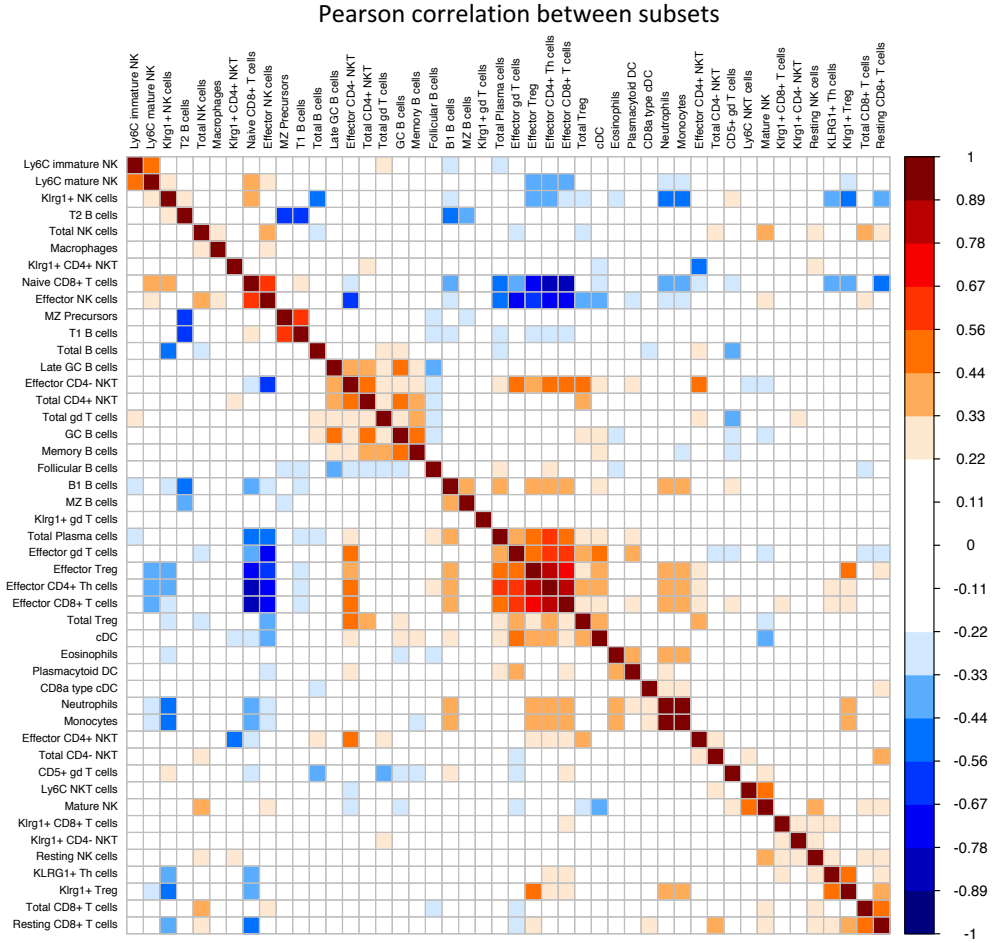

b Males versus females

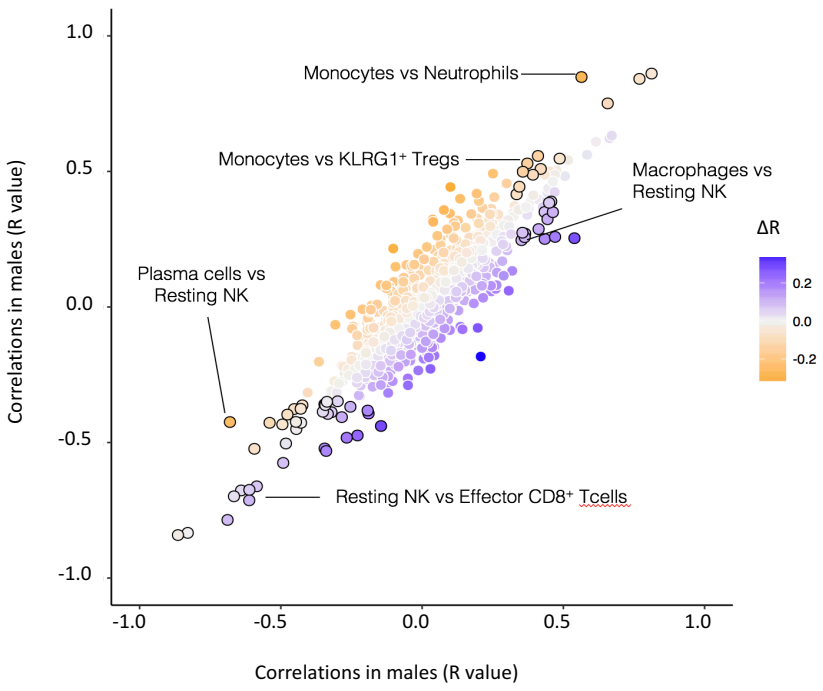

Figure 3

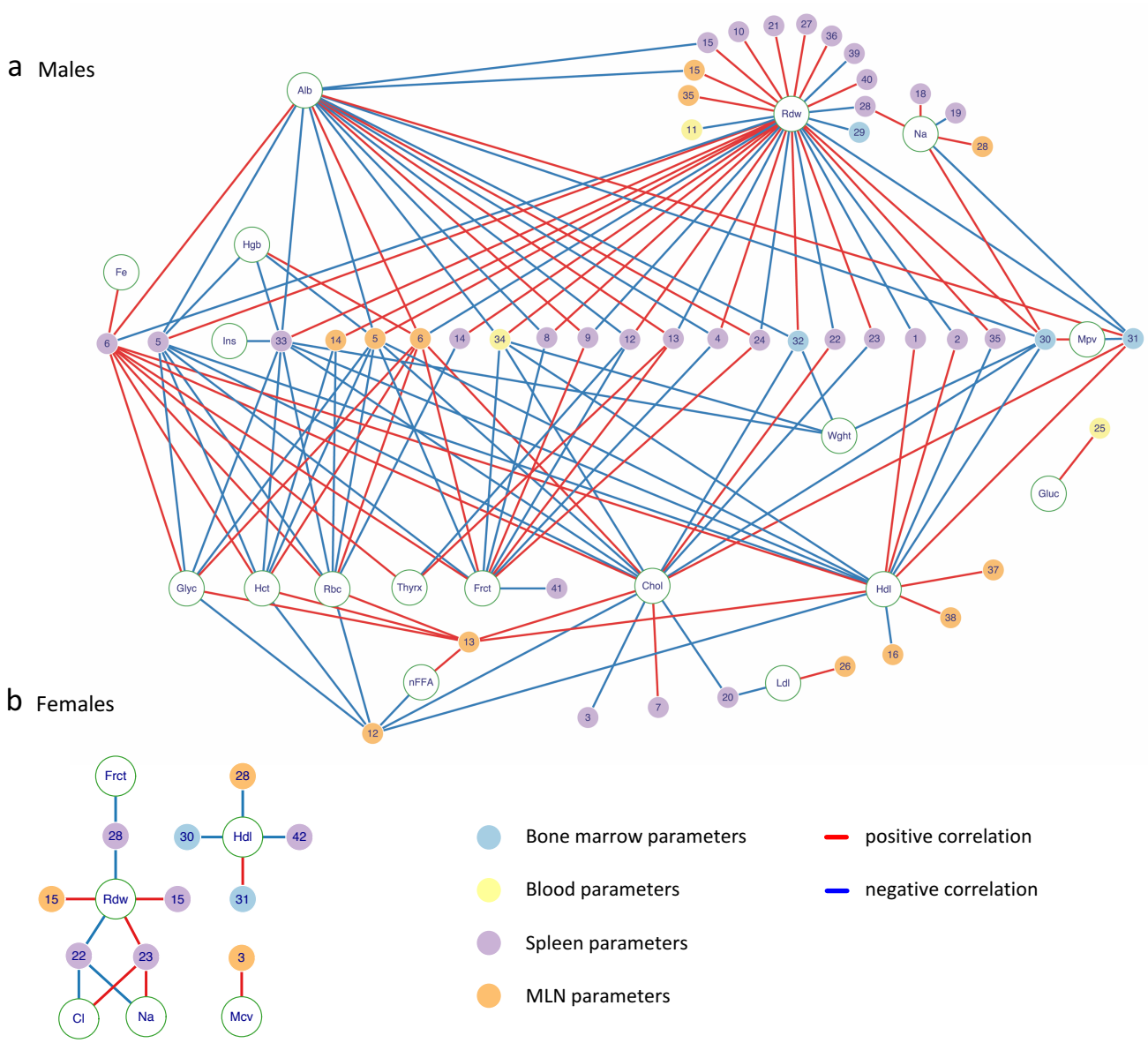

Alb	Albumin
Chol	Cholesterol
Cl	Chloride
Fe	Iron
Frct	Fructose
Gluc	Glucose
Glyc	Glycerin
Hct	Haematocrit
Hdl	HDL cholesterol
Hgb	Haemoglobin
Ins	Insulin
Ldl	LDL cholesterol
Mcv	Mean corpuscular volume
Mpv	Mean platelet volume
Na	Sodium
nFFA	Non-esterified free fatty acids
Rbc	Red blood cell count
Rdw	Red blood cell distribution width
Thyrx	Thyroxin
Wght	Weight

1	Total T cells
2	αβ T cells
3	CD8+ T cells
4	Effector CD8+ T cells
5	Resting CD8+ T cells
6	Naïve CD8+ T cells
7	CD4+ T cells
8	Effector CD4+ T helper cells
9	Resting CD4+ T helper cells
10	KLRG1+ CD4+ T helper cells
11	T_{reg} cells
12	Effector T_{reg} cells
13	Resting T_{reg} cells
14	KLRG1+ T_{reg} cells
15	CD5+ γδ T cells
16	Total NKT cells
17	Ly6C+ NKT cells
18	Effector CD4- NKT cells
19	Resting CD4- NKT cells
20	Total NK cells
21	KLRG1+ NK cells

22	Immature NK cells
23	Mature NK cells
24	Ly6C+ mature NK cells
25	Total B cells
26	Follicular B cells
27	Marginal zone B cells
28	Memory B cells
29	Total B cell precursors
30	Hardy Fraction A
31	Hardy Fraction B
32	Granulocytes (BM)
33	Granulocytes
34	Neutrophils
35	Eosinophils
36	Monocytes
37	Total DC
38	Conventional DC (cDC)
39	CD11b-high cDC
40	CD11b-low cDC
41	CD103+ CD11b-low cDC
42	Late germinal centre B cells

Figure 4

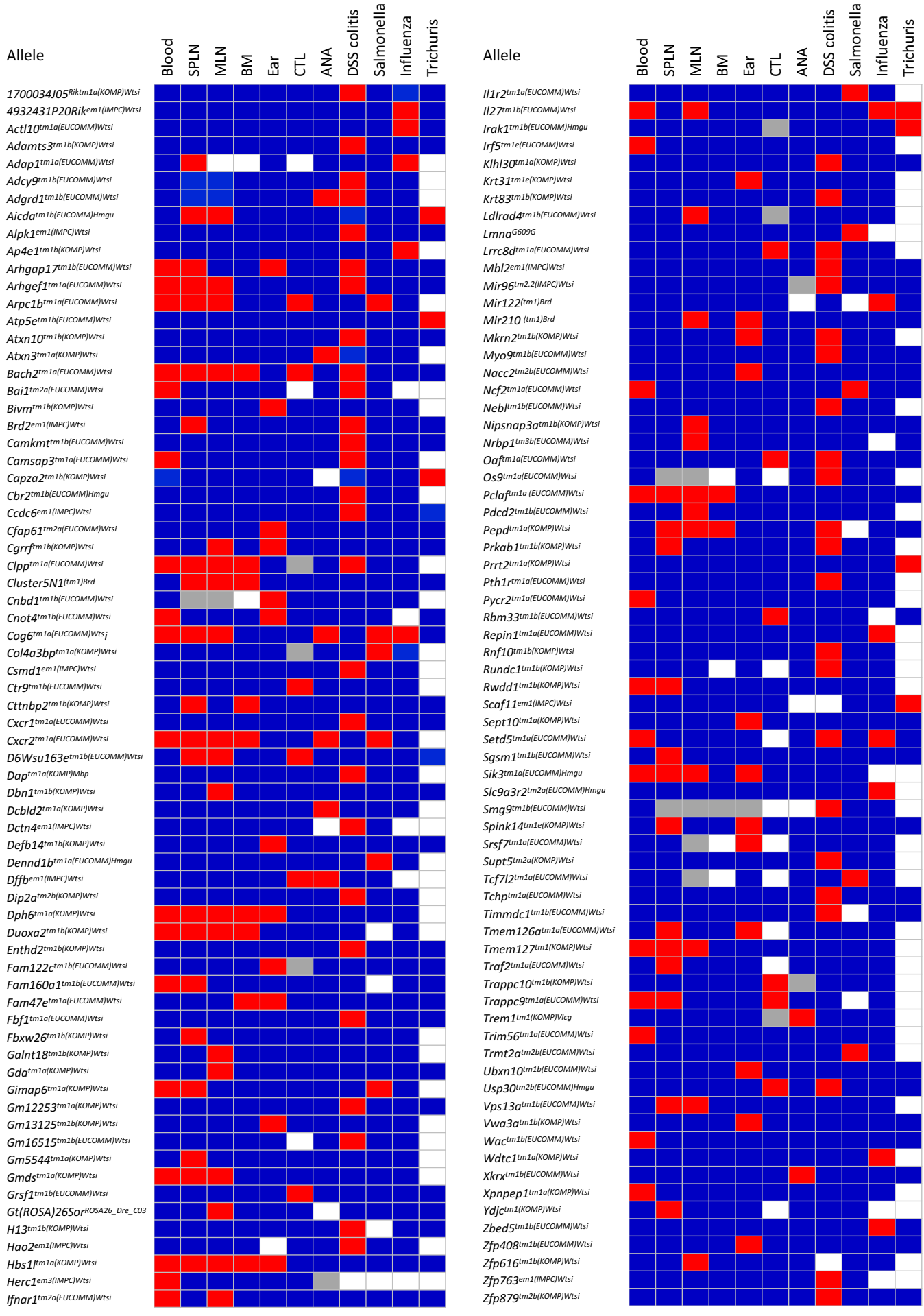
Allele
Blood
SPLN
MLN
BM
Ear
CTL
ANA
DSS colitis
Salmonella
Influenza
Trichuris
1700034J05Riktm1a(KOMP)Wtsi
4932431P20Rikem1(IMPC)Wtsi
Actl10tm1a(EUCOMM)Wtsi
Adamts3tm1b(KOMP)Wtsi
Adap1tm1a(EUCOMM)Wtsi
Adcy9tm1b(EUCOMM)Wtsi
Adgrd1tm1b(EUCOMM)Wtsi
Aicdatm1b(EUCOMM)Hmgu
Alpk1em1(IMPC)Wtsi
Ap4e1tm1b(KOMP)Wtsi
Arhgap17tm1b(EUCOMM)Wtsi
Arhgef1tm1a(EUCOMM)Wtsi
Arpc1btm1a(EUCOMM)Wtsi
Atp5etm1b(EUCOMM)Wtsi
Atxn10tm1b(KOMP)Wtsi
Atxn3tm1a(KOMP)Wtsi
Bach2tm1a(EUCOMM)Wtsi
Bai1tm2a(EUCOMM)Wtsi
Bivmtm1b(KOMP)Wtsi
Brd2em1(IMPC)Wtsi
Camkmttm1b(EUCOMM)Wtsi
Camsap3tm1a(EUCOMM)Wtsi
Capza2tm1b(KOMP)Wtsi
Cbr2tm1b(EUCOMM)Hmgu
Ccdc6em1(IMPC)Wtsi
Cfap61tm2a(EUCOMM)Wtsi
Cgrrftm1b(KOMP)Wtsi
Clpptm1a(EUCOMM)Wtsi
Cluster5N1(tm1)Brd
Cnbd1tm1b(EUCOMM)Wtsi
Cnot4tm1b(EUCOMM)Wtsi
Cog6tm1a(EUCOMM)Wtsi
Col4a3bptm1a(KOMP)Wtsi
Csmd1em1(IMPC)Wtsi
Ctr9tm1b(EUCOMM)Wtsi
Cttnbp2tm1b(KOMP)Wtsi
Cxcr1tm1a(EUCOMM)Wtsi
Cxcr2tm1a(EUCOMM)Wtsi
D6Wsu163etm1b(EUCOMM)Wtsi
Daptm1a(KOMP)Mbp
Dbn1tm1b(KOMP)Wtsi
Dcbld2tm1a(KOMP)Wtsi
Dctn4em1(IMPC)Wtsi
Defb14tm1b(KOMP)Wtsi
Dennd1btm1a(EUCOMM)Hmgu
Dffbem1(IMPC)Wtsi
Dip2atm2b(KOMP)Wtsi
Dph6tm1a(KOMP)Wtsi
Duoxa2tm1b(KOMP)Wtsi
Enthd2tm1b(KOMP)Wtsi
Fam122ctm1b(EUCOMM)Wtsi
Fam160a1tm1b(EUCOMM)Wtsi
Fam47etm1a(EUCOMM)Wtsi
Fbf1tm1a(EUCOMM)Wtsi
Fbxw26tm1b(KOMP)Wtsi
Galnt18tm1b(KOMP)Wtsi
Gdatm1a(KOMP)Wtsi
Gimap6tm1a(KOMP)Wtsi
Gm12253tm1a(KOMP)Wtsi
Gm13125tm1b(KOMP)Wtsi
Gm16515tm1b(EUCOMM)Wtsi
Gm5544tm1a(KOMP)Wtsi
Gmdstm1a(KOMP)Wtsi
Grsf1tm1b(EUCOMM)Wtsi
Gt(ROSA)26SorROSA26_Dre_C03
H13tm1b(KOMP)Wtsi
Hao2em1(IMPC)Wtsi
Hbs1ltm1a(KOMP)Wtsi
Herc1em3(IMPC)Wtsi
Ifnar1tm2a(EUCOMM)Wtsi
Allele
Blood
SPLN
MLN
BM
Ear
CTL
ANA
DSS colitis
Salmonella
Influenza
Trichuris
Il1r2tm1a(EUCOMM)Wtsi
Il27tm1b(EUCOMM)Wtsi
Irak1tm1b(EUCOMM)Hmgu
Irf5tm1e(EUCOMM)Wtsi
Klhl30tm1a(KOMP)Wtsi
Krt31tm1e(KOMP)Wtsi
Krt83tm1b(KOMP)Wtsi
Ldlrad4tm1b(EUCOMM)Wtsi
LmnaG609G
Lrrc8dtm1a(EUCOMM)Wtsi
Mbl2em1(IMPC)Wtsi
Mir96tm2.2(IMPC)Wtsi
Mir122(tm1)Brd
Mir210 (tm1)Brd
Mkrn2tm1b(KOMP)Wtsi
Myo9tm1b(EUCOMM)Wtsi
Nacc2tm2b(EUCOMM)Wtsi
Ncf2tm1a(EUCOMM)Wtsi
Nebltm1b(EUCOMM)Wtsi
Nipsnap3atm1b(KOMP)Wtsi
Nrbp1tm3b(EUCOMM)Wtsi
Oaftm1a(EUCOMM)Wtsi
Os9tm1a(EUCOMM)Wtsi
Pclaftm1a (EUCOMM)Wtsi
Pdcd2tm1b(EUCOMM)Wtsi
Pepdtm1a(KOMP)Wtsi
Prkab1tm1b(KOMP)Wtsi
Prrt2tm1a(KOMP)Wtsi
Pth1rtm1a(EUCOMM)Wtsi
Pycr2tm1a(EUCOMM)Wtsi
Rbm33tm1b(EUCOMM)Wtsi
Repin1tm1a(EUCOMM)Wtsi
Rnf10tm1b(KOMP)Wtsi
Rundc1tm1b(KOMP)Wtsi
Rwdd1tm1b(KOMP)Wtsi
Scaf11em1(IMPC)Wtsi
Sept10tm1a(KOMP)Wtsi
Setd5tm1a(EUCOMM)Wtsi
Sgsm1tm1b(EUCOMM)Wtsi
Sik3tm1a(EUCOMM)Hmgu
Slc9a3r2tm2a(EUCOMM)Hmgu
Smg9tm1b(EUCOMM)Wtsi
Spink14tm1e(KOMP)Wtsi
Srsf7tm1a(EUCOMM)Wtsi
Supt5tm2a(KOMP)Wtsi
Tcf7l2tm1a(EUCOMM)Wtsi
Tchptm1a(EUCOMM)Wtsi
Timmdc1tm1b(EUCOMM)Wtsi
Tmem126atm1a(EUCOMM)Wtsi
Tmem127tm1(KOMP)Wtsi
Traf2tm1a(EUCOMM)Wtsi
Trappc10tm1b(KOMP)Wtsi
Trappc9tm1a(EUCOMM)Wtsi
Trem1tm1(KOMP)Vlcg
Trim56tm1a(EUCOMM)Wtsi
Trmt2atm2b(EUCOMM)Wtsi
Ubxn10tm1b(EUCOMM)Wtsi
Usp30tm2b(EUCOMM)Hmgu
Vps13atm1b(EUCOMM)Wtsi
Vwa3atm1b(KOMP)Wtsi
Wactm1b(EUCOMM)Wtsi
Wdtc1tm1a(KOMP)Wtsi
Xkrxtm1b(EUCOMM)Wtsi
Xpnpep1tm1a(KOMP)Wtsi
Ydjctm1(KOMP)Wtsi
Zbed5tm1b(EUCOMM)Wtsi
Zfp408tm1b(EUCOMM)Wtsi
Zfp616tm1b(KOMP)Wtsi
Zfp763em1(IMPC)Wtsi
Zfp879tm2b(KOMP)Wtsi

Figure 5

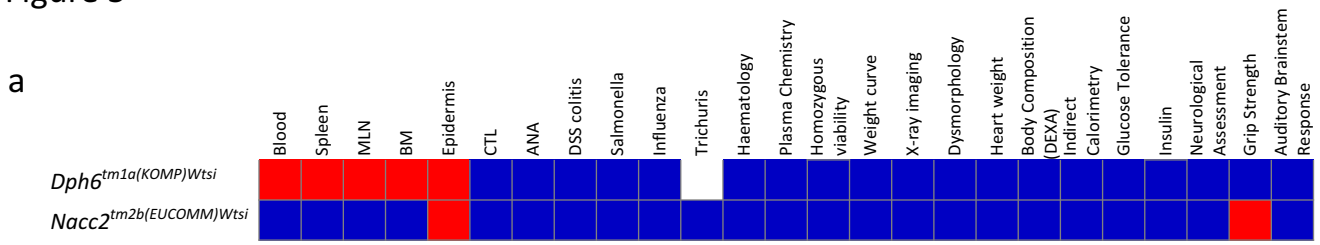
a
Blood
Spleen
MLN
BM
Epidermis
CTL
ANA
DSS colitis
Salmonella
Influenza
Trichuris
Haematology
Plasma Chemistry
Homozygous viability
Weight curve
X-ray imaging
Dysmorphology
Heart weight
Body Composition (DEXA)
Indirect Calorimetry
Glucose Tolerance
Insulin
Neurological Assessment
Grip Strength
Auditory Brainstem Response
Dph6tm1a(KOMP)Wtsi
Nacc2tm2b(EUCOMM)Wtsi

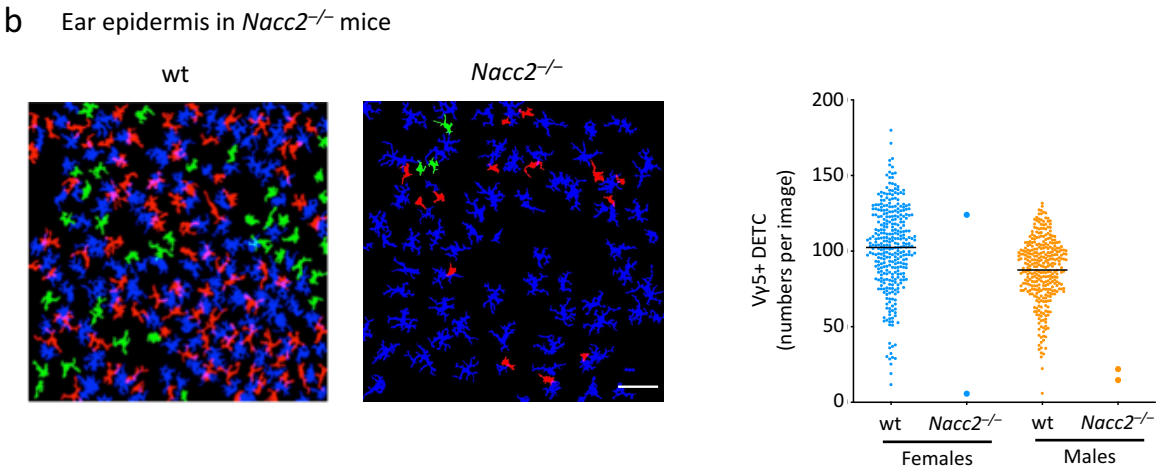
b
Ear epidermis in Nacc2−/− mice
wt
Nacc2−/−
Vγ5+ DETC (numbers per image)
200
150
100
50
0
wt
Nacc2−/−
wt
Nacc2−/−
Females
Males

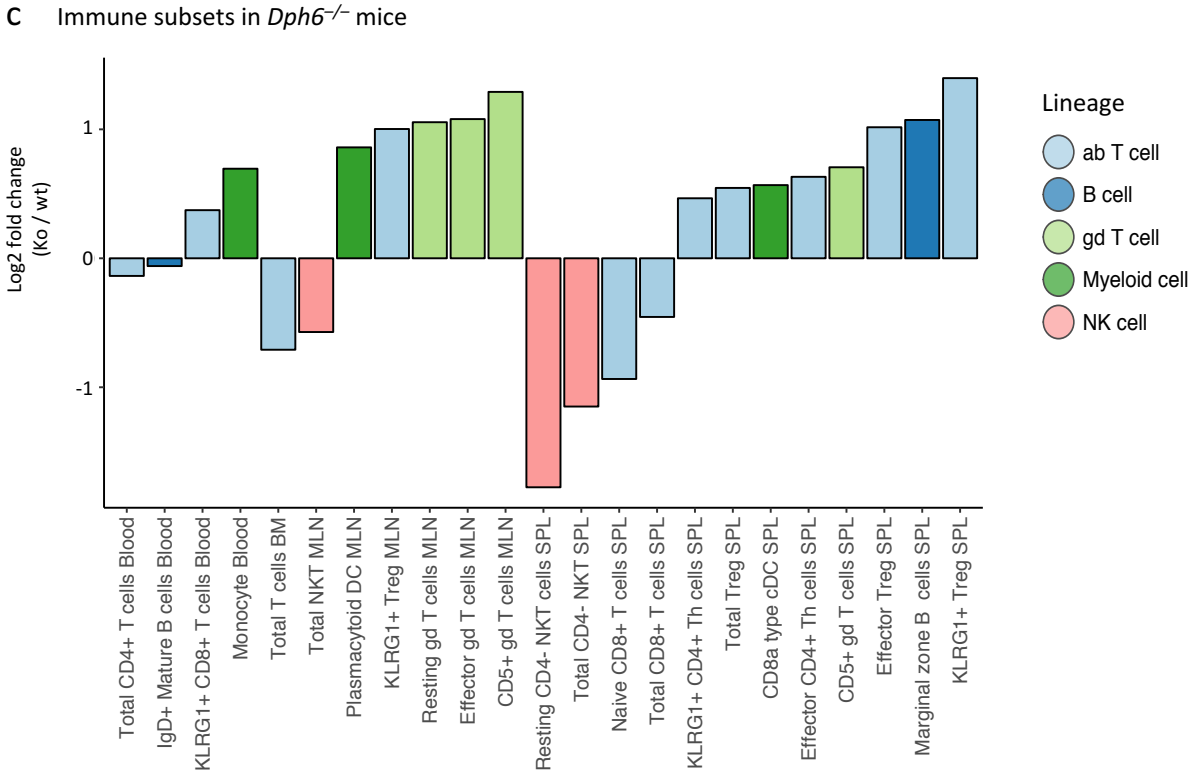
c
Immune subsets in Dph6−/− mice
Log2 fold change (Ko / wt)
1
0
-1
Total CD4+ T cells Blood
IgD+ Mature B cells Blood
KLRG1+ CD8+ T cells Blood
Monocyte Blood
Total T cells BM
Total NKT MLN
Plasmacytoid DC MLN
KLRG1+ Treg MLN
Resting gd T cells MLN
Effector gd T cells MLN
CD5+ gd T cells MLN
Resting CD4- NKT cells SPL
Total CD4- NKT SPL
Naive CD8+ T cells SPL
Total CD8+ T cells SPL
KLRG1+ CD4+ Th cells SPL
Total Treg SPL
CD8a type cDC SPL
Effector CD4+ Th cells SPL
CD5+ gd T cells SPL
Effector Treg SPL
Marginal zone B cells SPL
KLRG1+ Treg SPL
Lineage
ab T cell
B cell
gd T cell
Myeloid cell
NK cell

Figure 6

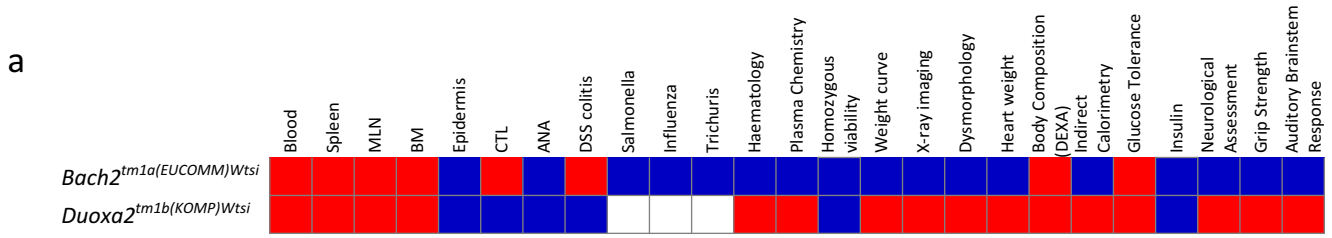
a
Blood
Spleen
MLN
BM
Epidermis
CTL
ANA
DSS colitis
Salmonella
Influenza
Trichuris
Haematology
Plasma Chemistry
Homozygous viability
Weight curve
X-ray imaging
Dysmorphology
Heart weight
Body Composition (DEXA)
Indirect Calorimetry
Glucose Tolerance
Insulin
Neurological Assessment
Grip Strength
Auditory Brainstem Response
Bach2tm1a(EUCOMM)Wtsi
Duoxa2tm1b(KOMP)Wtsi

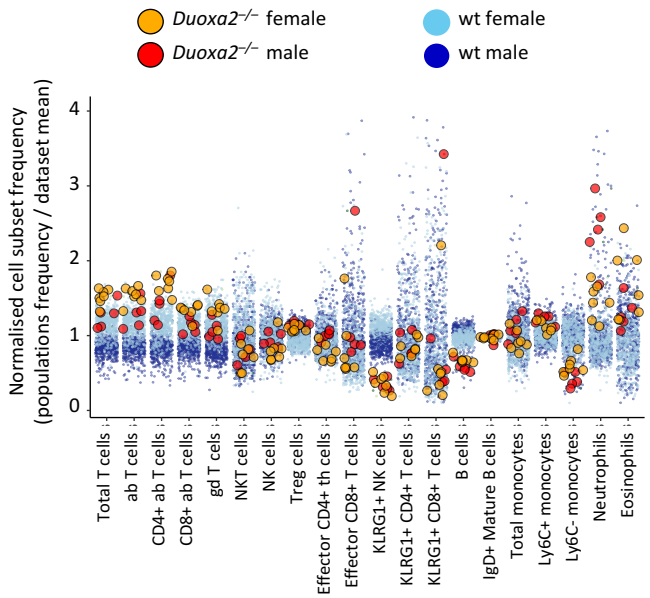
b
Blood immune cell subsets in Duoxa2−/− mice
Duoxa2−/− female
Duoxa2−/− male
wt female
wt male
Normalised cell subset frequency (populations frequency / dataset mean)
Total T cells
ab T cells
CD4+ ab T cells
CD8+ ab T cells
gd T cels
NKT cells
NK cells
Treg cells
Effector CD4+ th cells
Effector CD8+ T cells
KLRG1+ NK cells
KLRG1+ CD4+ T cells
KLRG1+ CD8+ T cells
B cells
IgD+ Mature B cells
Total monocytes
Ly6C+ monocytes
Ly6C- monocytes
Neutrophils
Eosinophils

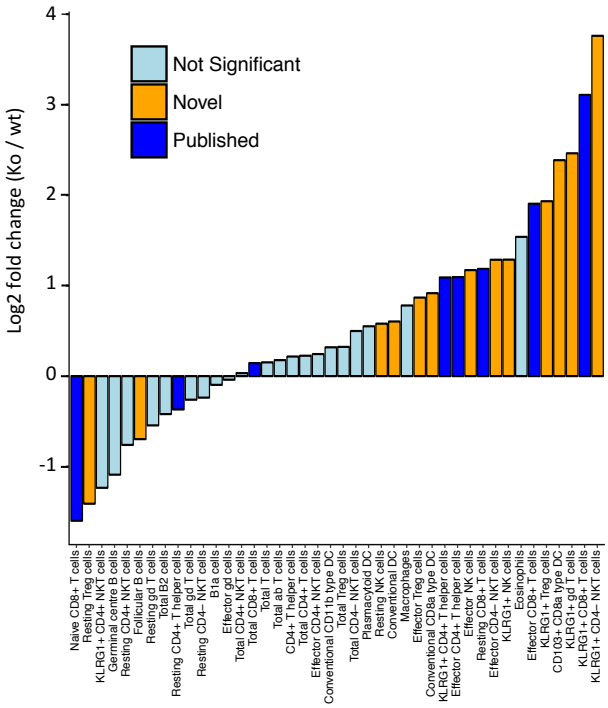
c
Spleen immune cell subsets in Bach2−/− mice
Not Significant
Novel
Published
Log2 fold change (Ko / wt)
Naive CD8+ T cells
Resting Treg cells
KLRG1+ CD4+ NK cells
Germinal Center B cells
Resting CD4+ NKT cells
Follicular B cells
Resting gd T cells
Total B2 cells
Resting CD4+ T helper cells
Total gd T cells
Resting CD4− NKT cells
B1a cells
Effector gd cells
Total CD4+ NKT cells
Total CD8+ T cells
Total T cells
Total ab T cells
CD4+ T helper cells
Total CD4+ T cells
Effector CD4+ NKT cells
Conventional CD11b type DC
Total Treg cells
Total CD4− NKT cells
Plasmacytoid DC
Resting NK cells
Conventional DC
Macrophages
Effector Treg cells
Conventional CD8a type DC
KLRG1+ CD4+ T helper cells
Effector CD4+ T helper cells
Effector NK cells
Resting CD8+ T cells
Effector CD4− NKT cells
KLRG1+ NK cells
Eosinophils
Effector CD8+ T cells
KLRG1+ Treg cells
CD103+ CD8a type DC
KLRG1+ gd T cells
KLRG1+ CD8+ T cells
KLRG1+ CD4− NKT cells

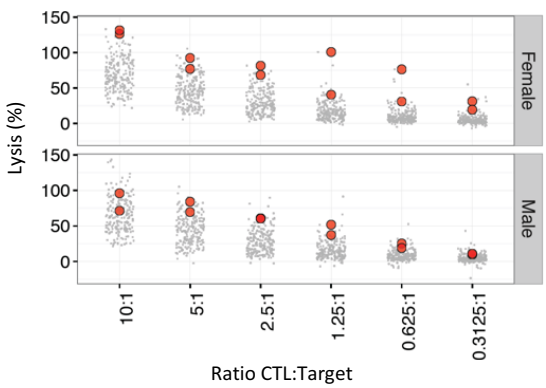
d
Cytotoxic T cell lysis in Bach2-/- mice
Lysis (%)
Female
Male
10:1
5:1
2.5:1
1.25:1
0.625:1
0.3125:1
Ratio CTL:Target

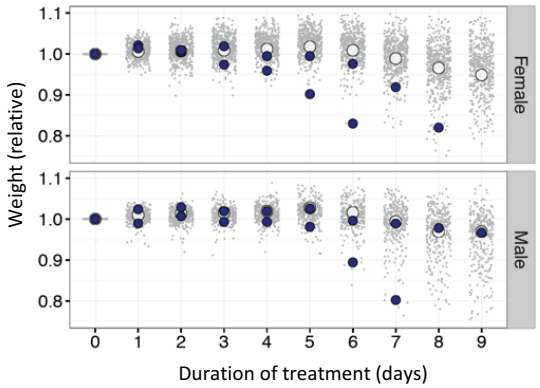
e
DSS-induced colitis in Bach2-/- mice
Weight (relative)
Female
Male
Duration of treatment (days)

Figure 7

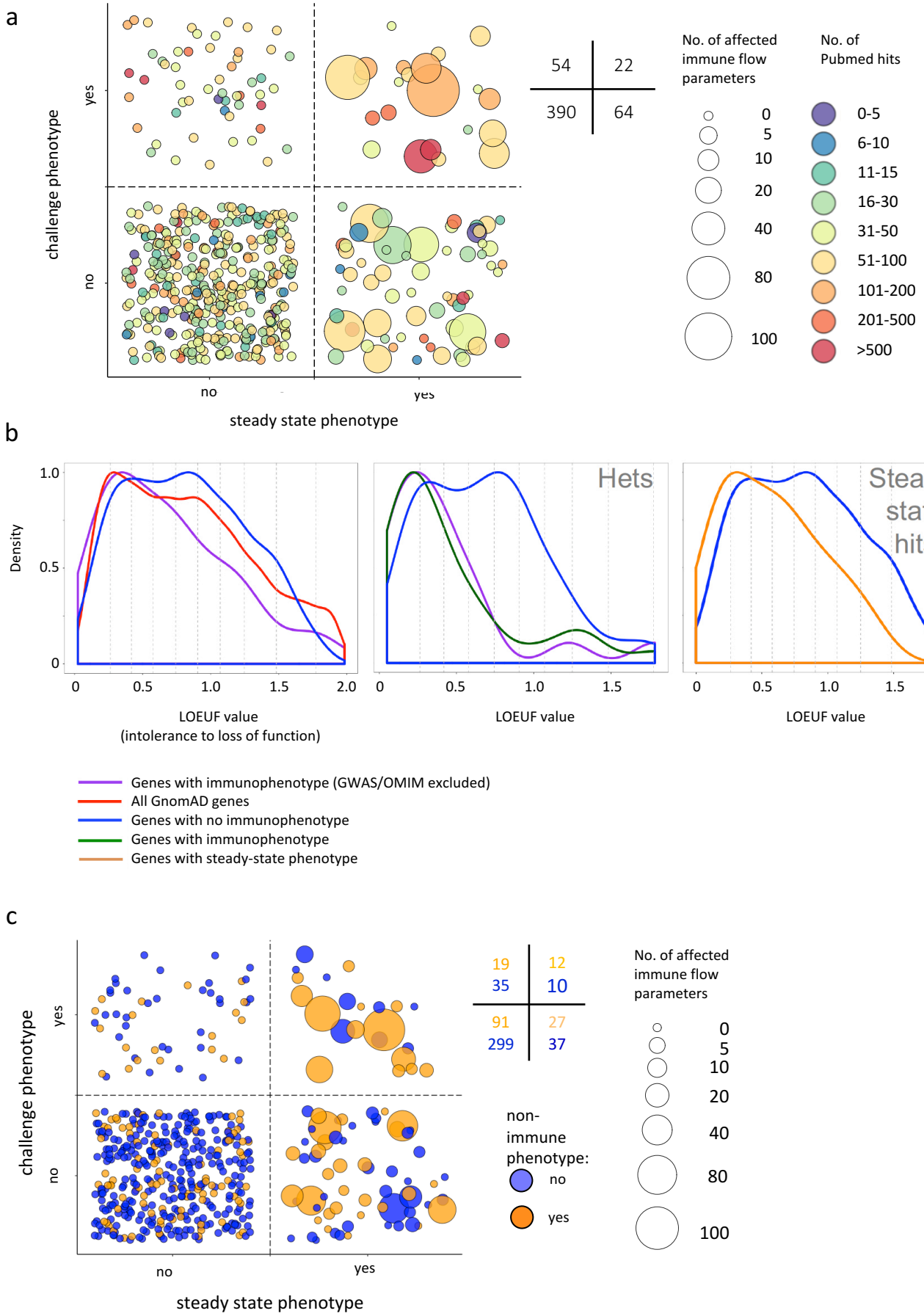
a
challenge phenotype
yes
no
no
yes
steady state phenotype
54
22
390
64
No. of affected immune flow parameters
0
5
10
20
40
80
100
No. of Pubmed hits
0-5
6-10
11-15
16-30
31-50
51-100
101-200
201-500
>500
b
Density
1.0
0.5
0
0
0.5
1.0
1.5
2.0
LOEUF value
(intolerance to loss of function)
Hets
Steady-state hits
Genes with immunophenotype (GWAS/OMIM excluded)
All GnomAD genes
Genes with no immunophenotype
Genes with immunophenotype
Genes with steady-state phenotype
c
challenge phenotype
yes
no
no
yes
steady state phenotype
19
12
35
10
91
27
299
37
non-immune phenotype:
no
yes
No. of affected immune flow parameters
0
5
10
20
40
80
100

Figure 8

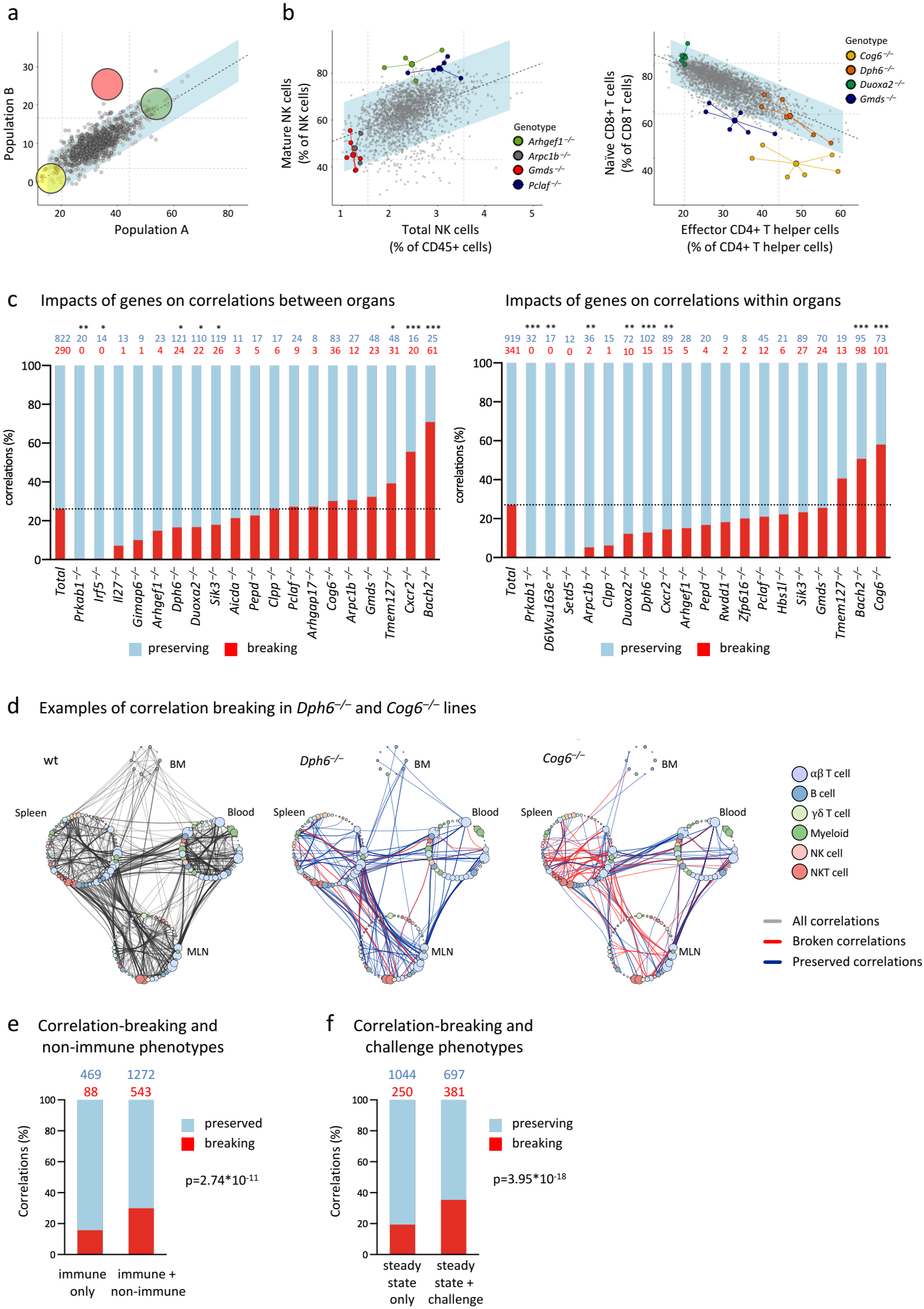
a
Population B
Population A
b
Mature NK cells (% of NK cells)
Total NK cells (% of CD45+ cells)
Genotype
Arhgef1 −/−
Arpc1b −/−
Gmds −/−
Pclaf −/−
Naïve CD8+ T cells (% of CD8 T cells)
Effector CD4+ T helper cells (% of CD4+ T helper cells)
Genotype
Cog6 −/−
Dph6 −/−
Duoxa2 −/−
Gmds −/−
c
Impacts of genes on correlations between organs
correlations (%)
822 20 14 13 9 23 121 110 119 11 17 17 24 8 83 27 48 48 16 25
290 0 0 1 1 4 24 22 26 3 5 6 9 3 36 12 23 31 20 61
Total
Prkab1 −/−
Irf5 −/−
Il27 −/−
Gimap6 −/−
Arhgef1 −/−
Dph6 −/−
Duoxa2 −/−
Sik3 −/−
Aicda −/−
Pepd −/−
Clpp −/−
Pclaf −/−
Arhgap17 −/−
Cog6 −/−
Arpc1b −/−
Gmds −/−
Tmem127 −/−
Cxcr2 −/−
Bach2 −/−
preserving
breaking
Impacts of genes on correlations within organs
correlations (%)
919 32 17 12 36 15 72 102 89 28 20 9 8 45 21 89 70 19 95 73
341 0 0 0 2 1 10 15 15 5 4 2 2 12 6 27 24 13 98 101
Total
Prkab1 −/−
D6Wsu163e −/−
Setd5 −/−
Arpc1b −/−
Clpp −/−
Duoxa2 −/−
Dph6 −/−
Cxcr2 −/−
Arhgef1 −/−
Pepd −/−
Rwdd1 −/−
Zfp616 −/−
Pclaf −/−
Hbs1l −/−
Sik3 −/−
Gmds −/−
Tmem127 −/−
Bach2 −/−
Cog6 −/−
preserving
breaking
d
Examples of correlation breaking in Dph6−/− and Cog6−/− lines
wt
Dph6−/−
Cog6−/−
BM
Spleen
Blood
MLN
αβ T cell
B cell
γδ T cell
Myeloid
NK cell
NKT cell
All correlations
Broken correlations
Preserved correlations
e
Correlation-breaking and non-immune phenotypes
469 1272
88 543
Correlations (%)
preserved
breaking
p=2.74*10-11
immune only
immune + non-immune
f
Correlation-breaking and challenge phenotypes
1044 697
250 381
Correlations (%)
preserving
breaking
p=3.95*10-18
steady state only
steady state + challenge

Supplementary Figure 1

a

Tests performed at WTSI	
Viability / Fertility	Viability Fertility Recessive lethality
Anatomy	X-ray imaging Dysmorphology Hair dysmorphology Hair Follicle Cycling Heart weight
Metabolism	Body Composition (DEXA) Indirect Calorimetry Glucose Tolerance Insulin
Immune System	Blood cytometric analysis Salmonella challenge Citrobacter challenge
Other	Modified Shirpa Grip Strength Erythrocyte Micronuclei Auditory Brainstem Response Plasma Chemistry Haematology

b

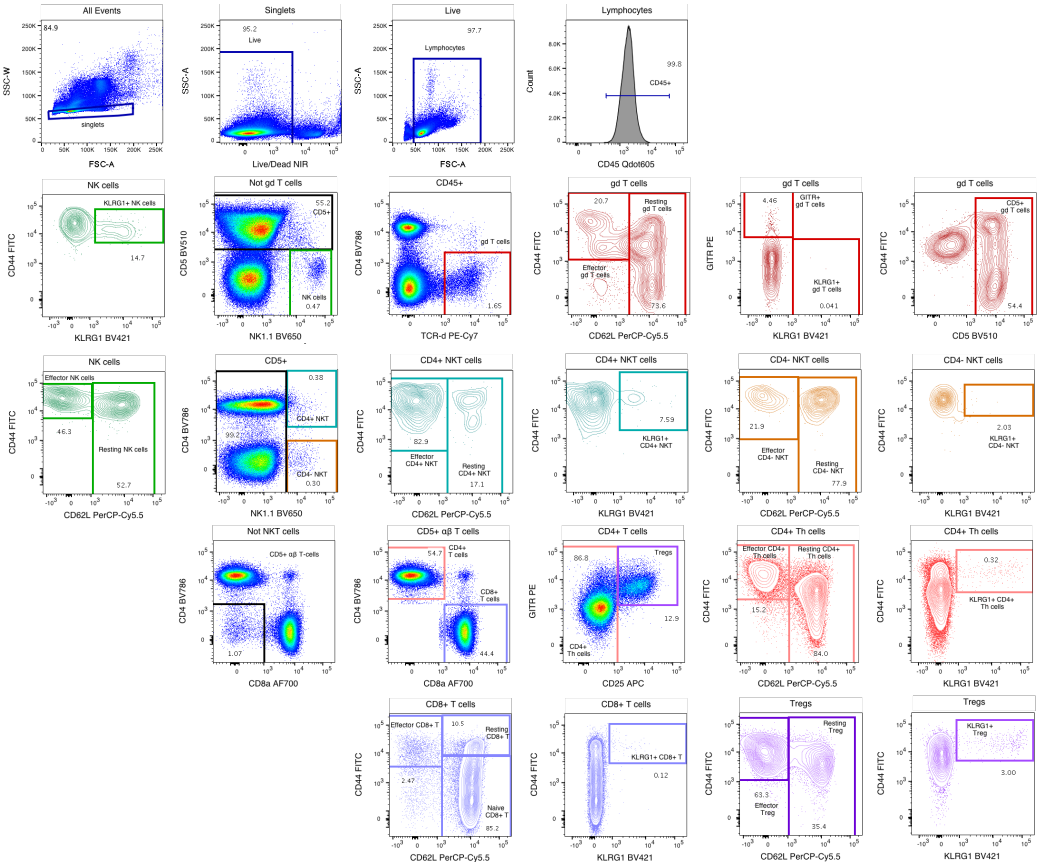

c

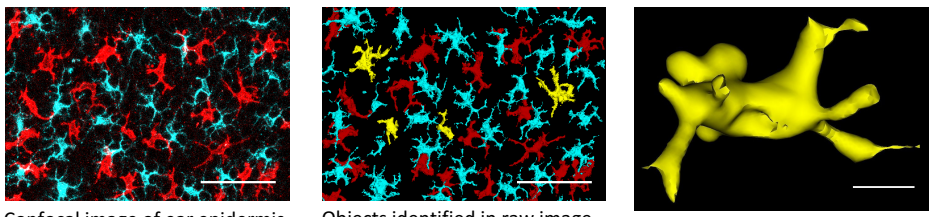

d

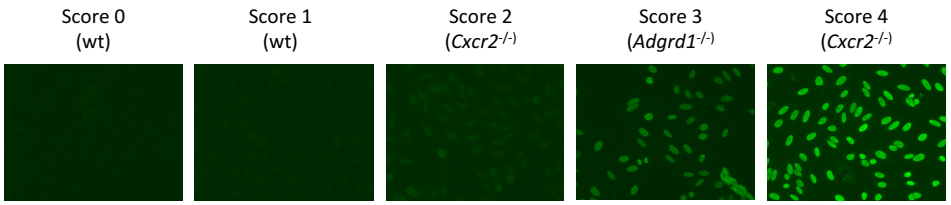

e

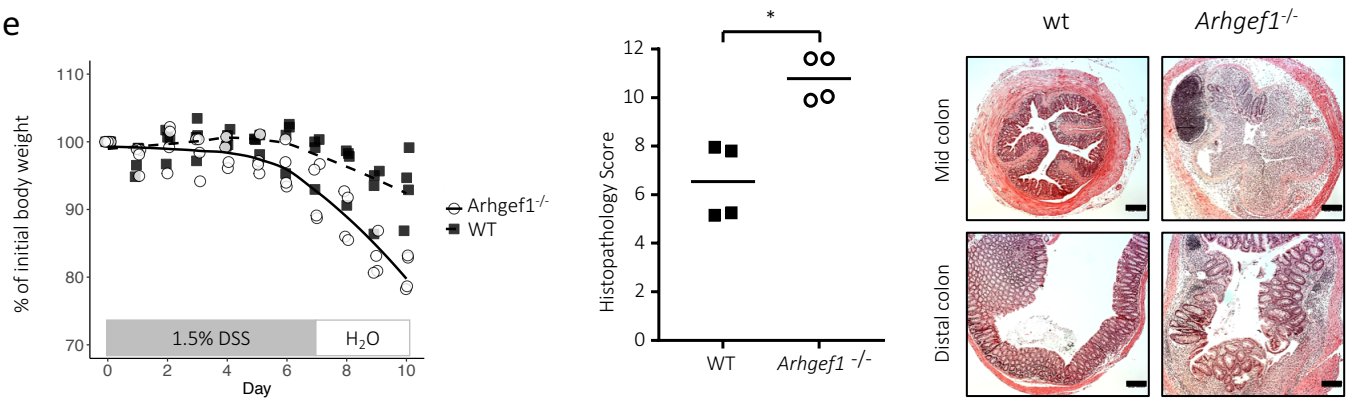

f

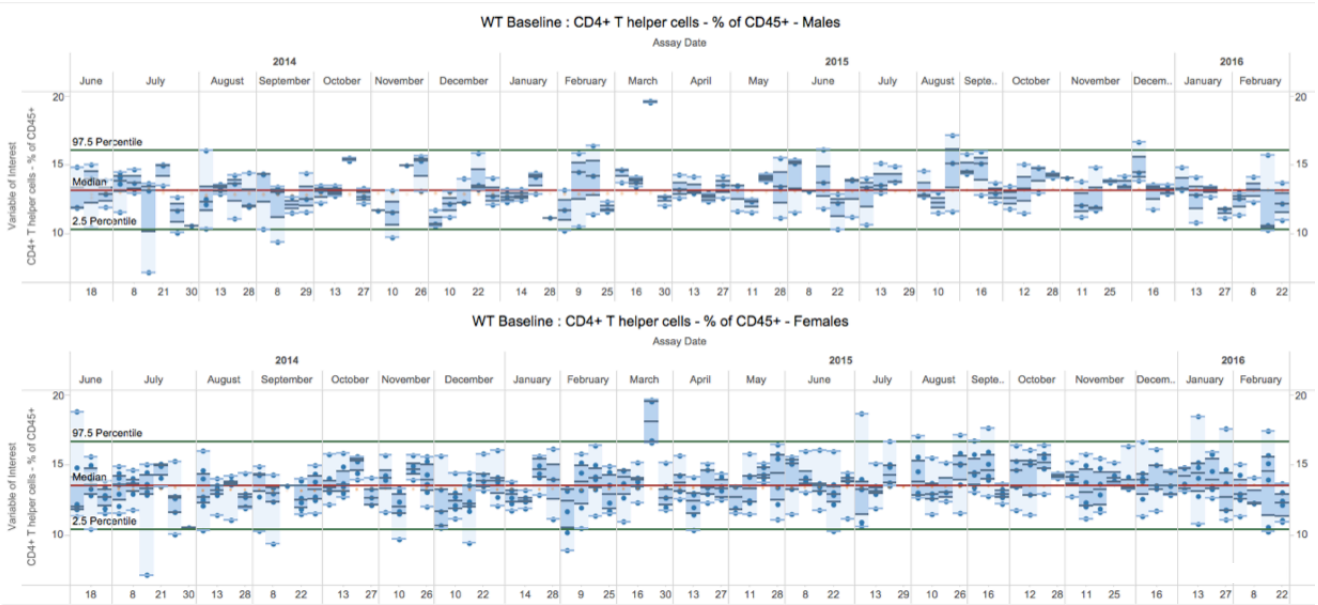
WT Baseline : CD4+ T helper cells - % of CD45+ - Males
Assay Date
2014
2015
2016
June
July
August
September
October
November
December
January
February
March
April
May
June
July
August
Septe..
October
November
Decem..
January
February
97.5 Percentile
Median
2.5 Percentile
Variable of Interest
CD4+ T helper cells - % of CD45+
WT Baseline : CD4+ T helper cells - % of CD45+ - Females
Assay Date
97.5 Percentile
Median
2.5 Percentile
Variable of Interest
CD4+ T helper cells - % of CD45+

g

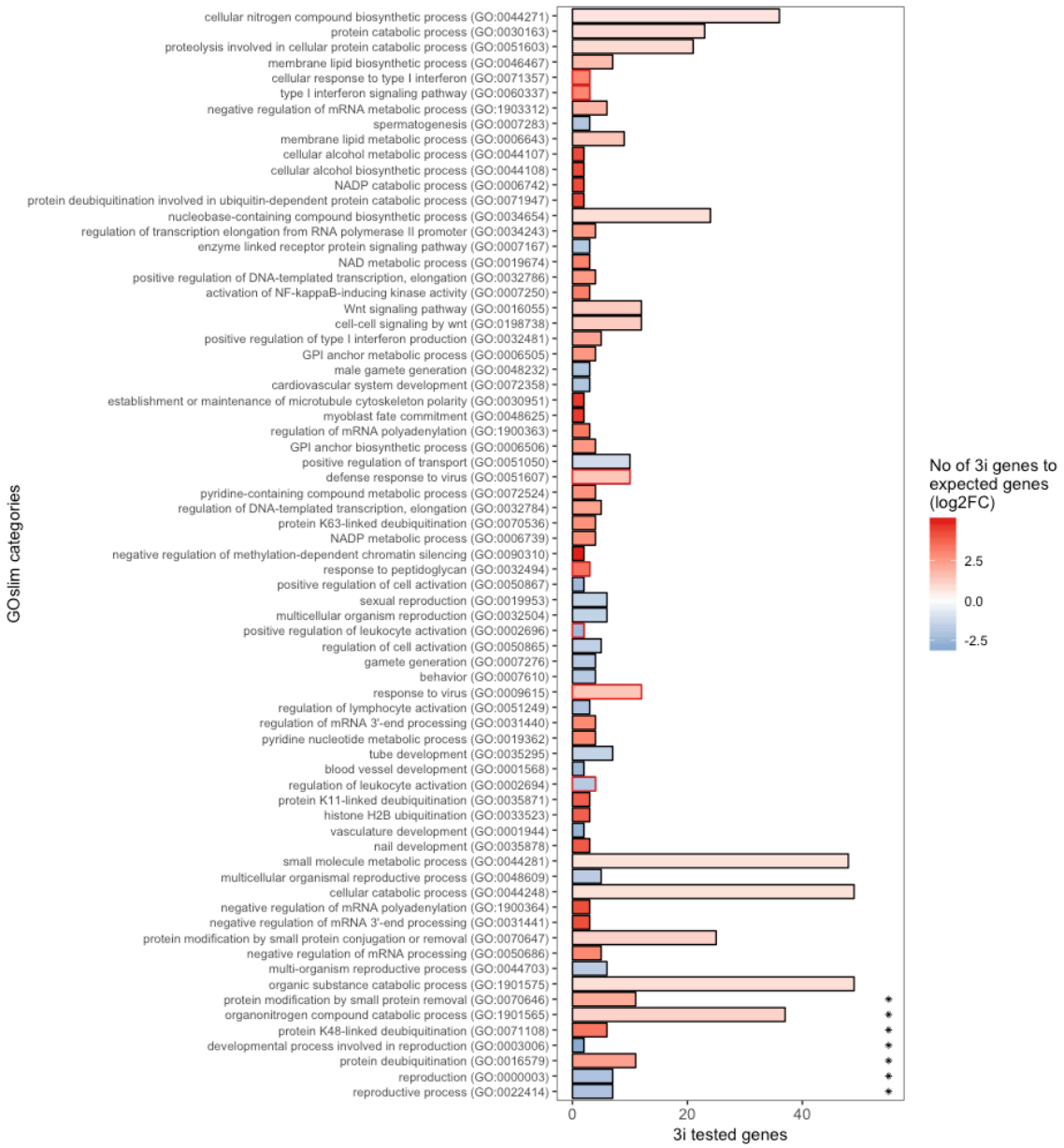
cellular nitrogen compound biosynthetic process (GO:0044271)
protein catabolic process (GO:0030163)
proteolysis involved in cellular protein catabolic process (GO:0051603)
membrane lipid biosynthetic process (GO:0046467)
cellular response to type I interferon (GO:0071357)
type I interferon signaling pathway (GO:0060337)
negative regulation of mRNA metabolic process (GO:1903312)
spermatogenesis (GO:0007283)
membrane lipid metabolic process (GO:0006643)
cellular alcohol metabolic process (GO:0044107)
cellular alcohol biosynthetic process (GO:0044108)
NADP catabolic process (GO:0006742)
protein deubiquitination involved in ubiquitin-dependent protein catabolic process (GO:0071947)
nucleobase-containing compound biosynthetic process (GO:0034654)
regulation of transcription elongation from RNA polymerase II promoter (GO:0034243)
enzyme linked receptor protein signaling pathway (GO:0007167)
NAD metabolic process (GO:0019674)
positive regulation of DNA-templated transcription, elongation (GO:0032786)
activation of NF-kappaB-inducing kinase activity (GO:0007250)
Wnt signaling pathway (GO:0016055)
cell-cell signaling by wnt (GO:0198738)
positive regulation of type I interferon production (GO:0032481)
GPI anchor metabolic process (GO:0006505)
male gamete generation (GO:0048232)
cardiovascular system development (GO:0072358)
establishment or maintenance of microtubule cytoskeleton polarity (GO:0030951)
myoblast fate commitment (GO:0048625)
regulation of mRNA polyadenylation (GO:1900363)
GPI anchor biosynthetic process (GO:0006506)
positive regulation of transport (GO:0051050)
defense response to virus (GO:0051607)
pyridine-containing compound metabolic process (GO:0072524)
regulation of DNA-templated transcription, elongation (GO:0032784)
protein K63-linked deubiquitination (GO:0070536)
NADP metabolic process (GO:0006739)
negative regulation of methylation-dependent chromatin silencing (GO:0090310)
response to peptidoglycan (GO:0032494)
positive regulation of cell activation (GO:0050867)
sexual reproduction (GO:0019953)
multicellular organism reproduction (GO:0032504)
positive regulation of leukocyte activation (GO:0002696)
regulation of cell activation (GO:0050865)
gamete generation (GO:0007276)
behavior (GO:0007610)
response to virus (GO:0009615)
regulation of lymphocyte activation (GO:0051249)
regulation of mRNA 3'-end processing (GO:0031440)
pyridine nucleotide metabolic process (GO:0019362)
tube development (GO:0035295)
blood vessel development (GO:0001568)
regulation of leukocyte activation (GO:0002694)
protein K11-linked deubiquitination (GO:0035871)
histone H2B ubiquitination (GO:0033523)
vasculature development (GO:0001944)
nail development (GO:0035878)
small molecule metabolic process (GO:0044281)
multicellular organismal reproductive process (GO:0048609)
cellular catabolic process (GO:0044248)
negative regulation of mRNA polyadenylation (GO:1900364)
negative regulation of mRNA 3'-end processing (GO:0031441)
protein modification by small protein conjugation or removal (GO:0070647)
negative regulation of mRNA processing (GO:0050686)
multi-organism reproductive process (GO:0044703)
organic substance catabolic process (GO:1901575)
protein modification by small protein removal (GO:0070646)
organonitrogen compound catabolic process (GO:1901565)
protein K48-linked deubiquitination (GO:0071108)
developmental process involved in reproduction (GO:0003006)
protein deubiquitination (GO:0016579)
reproduction (GO:0000003)
reproductive process (GO:0022414)
GOslim categories
0
20
40
3i tested genes
No of 3i genes to expected genes (log2FC)
2.5
0.0
-2.5

h

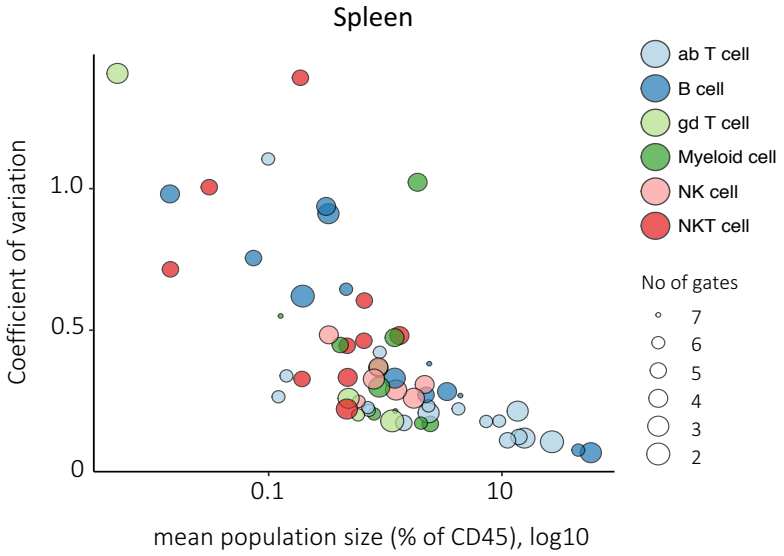
Spleen
Coefficient of variation
1.0
0.5
0
0.1
10
mean population size (% of CD45), log10
ab T cell
B cell
gd T cell
Myeloid cell
NK cell
NKT cell
No of gates
7
6
5
4
3
2

i

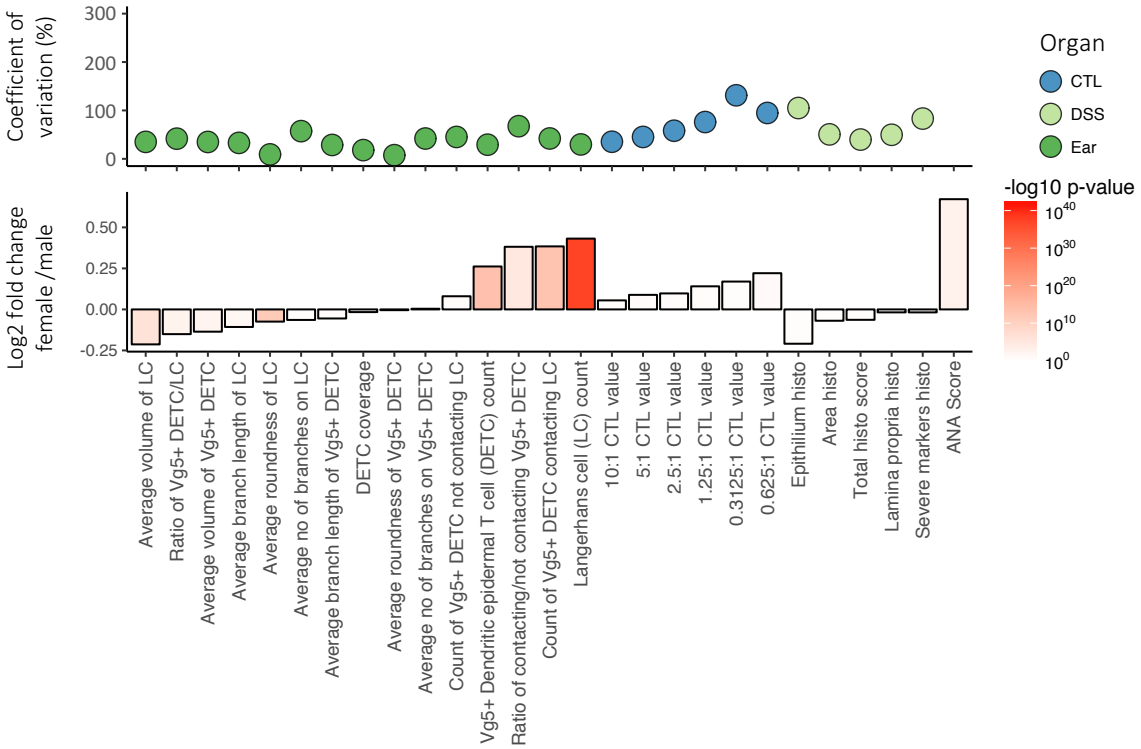
Coefficient of variation (%)
300
200
100
0
Log2 fold change female /male
0.50
0.25
0.00
-0.25
Organ
CTL
DSS
Ear
-log10 p-value
10^{40}
10^{30}
10^{20}
10^{10}
10^{0}
Average volume of LC
Ratio of Vg5+ DETC/LC
Average volume of Vg5+ DETC
Average branch length of LC
Average roundness of LC
Average no of branches on LC
Average branch length of Vg5+ DETC
DETC coverage
Average roundness of Vg5+ DETC
Average no of branches on Vg5+ DETC
Count of Vg5+ DETC not contacting LC
Vg5+ Dendritic epidermal T cell (DETC) count
Ratio of contacting/not contacting Vg5+ DETC
Count of Vg5+ DETC contacting LC
Langerhans cell (LC) count
10:1 CTL value
5:1 CTL value
2.5:1 CTL value
1.25:1 CTL value
0.3125:1 CTL value
0.625:1 CTL value
Epithilium histo
Area histo
Total histo score
Lamina propria histo
Severe markers histo
ANA Score

Supplementary Figure 2

Females

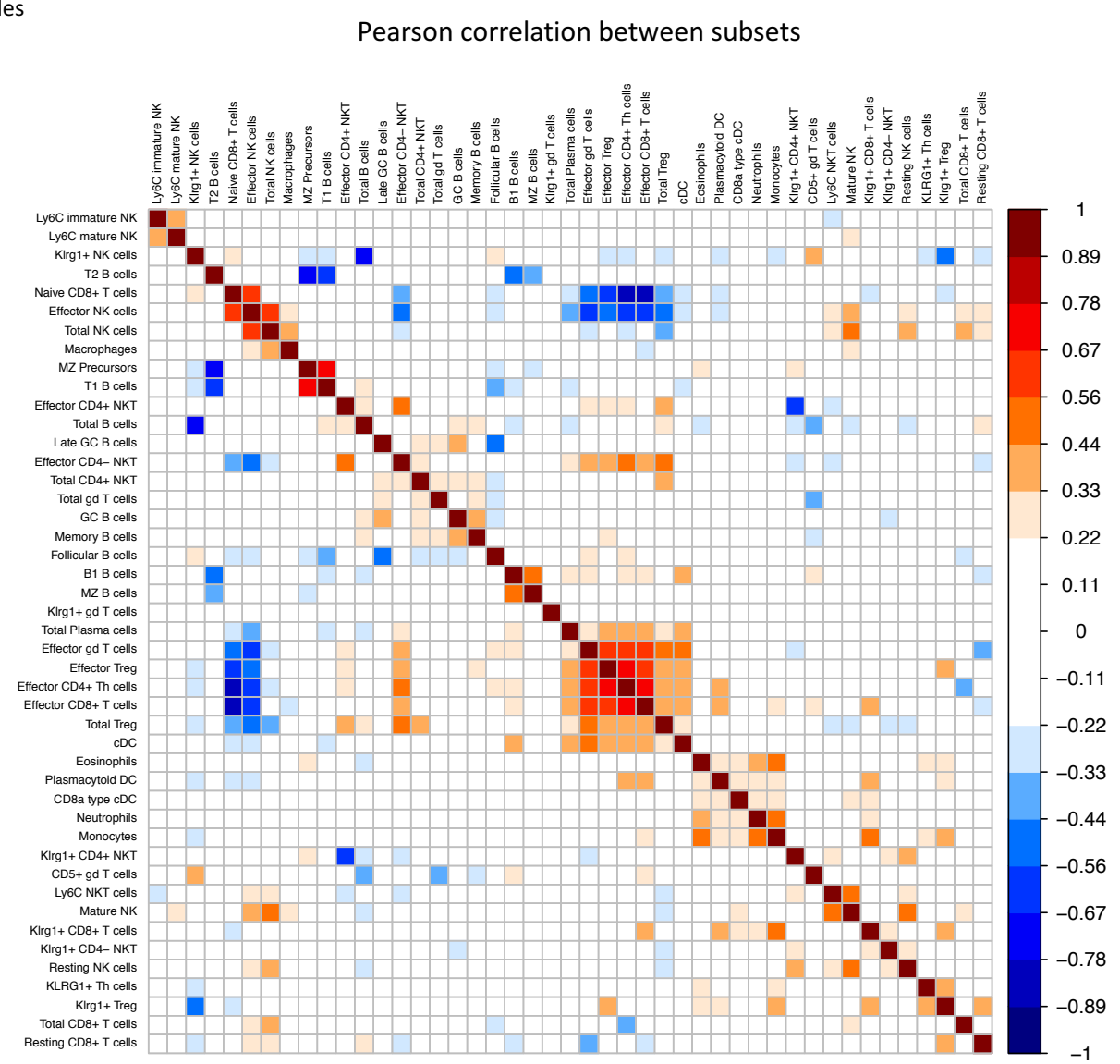

Supplementary Figure 3

a Males

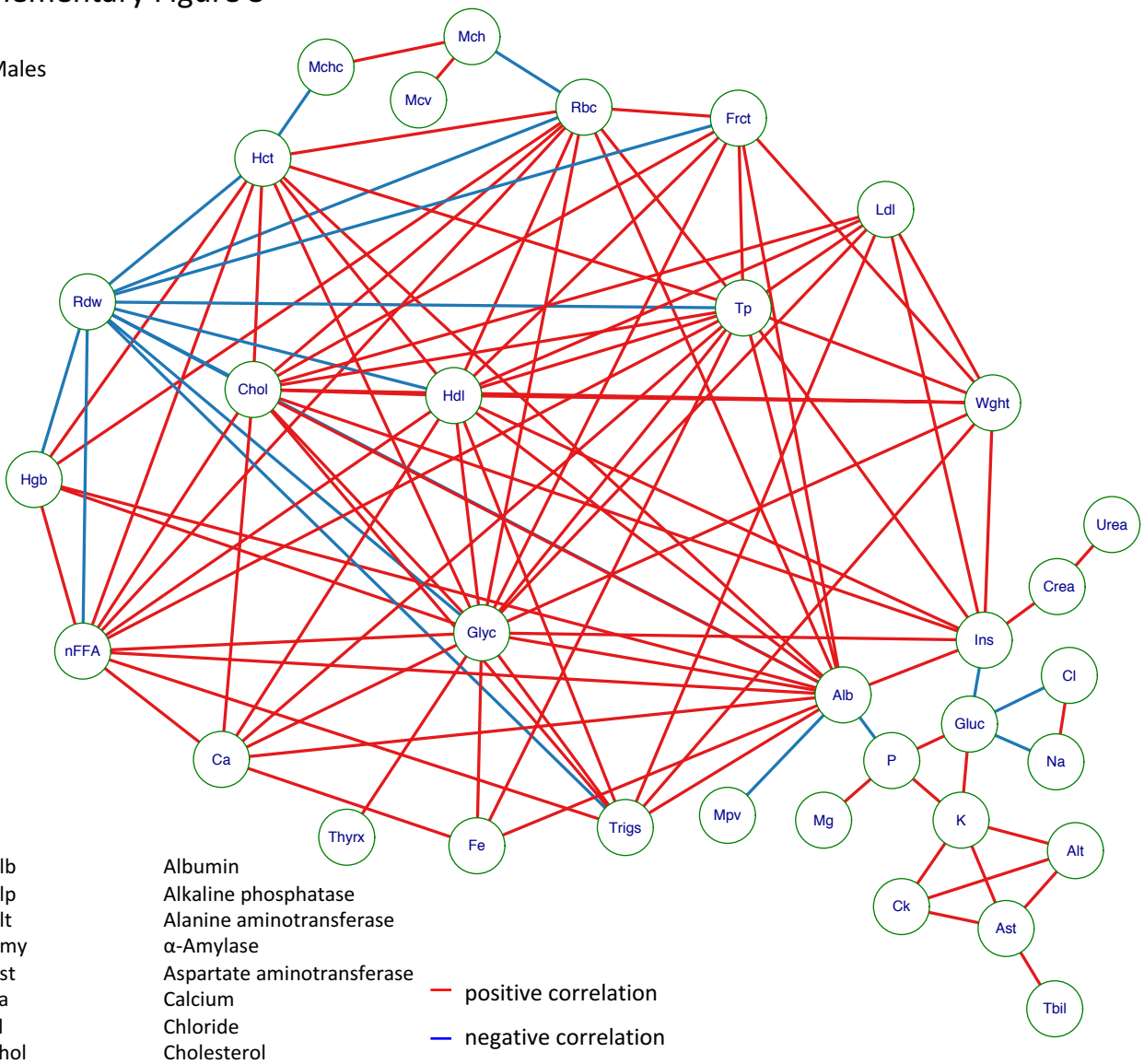

Alb	Albumin
Alp	Alkaline phosphatase
Alt	Alanine aminotransferase
Amy	α-Amylase
Ast	Aspartate aminotransferase
Ca	Calcium
Cl	Chloride
Chol	Cholesterol
Ck	Creatinine kinase
Crea	Creatinine
Fe	Iron
Fruct	Fructosamine
Gluc	Glucose
Glyc	Glycerol
Hct	Hematocrit
Hdl	HDL cholesterol
Hgb	Hemoglobulin
Ins	Insulin
K	Potassium
Ldl	LDL cholesterol
Mch	Mean corpuscular hemoglobin
Mchc	Mean cell hemoglobin concentration
Mcv	Mean corpuscular volume
Mg	Magnesium
Mpv	Mean platelet volume
Na	Sodium
nFFA	Free fatty acids
P	Phosphorus
Rbc	Red blood cell count
Rdw	Red blood cell distribution width
Tbil	Total bilirubin
Thyrx	Thyroxine
Tp	Total protein
Trigs	Triglycerides
Urea	Urea

b Females

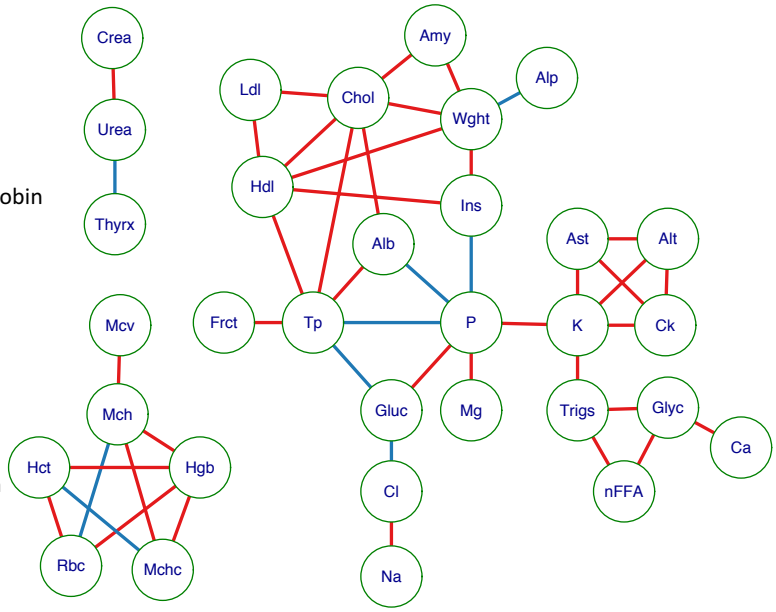

Supplementary Figure 4

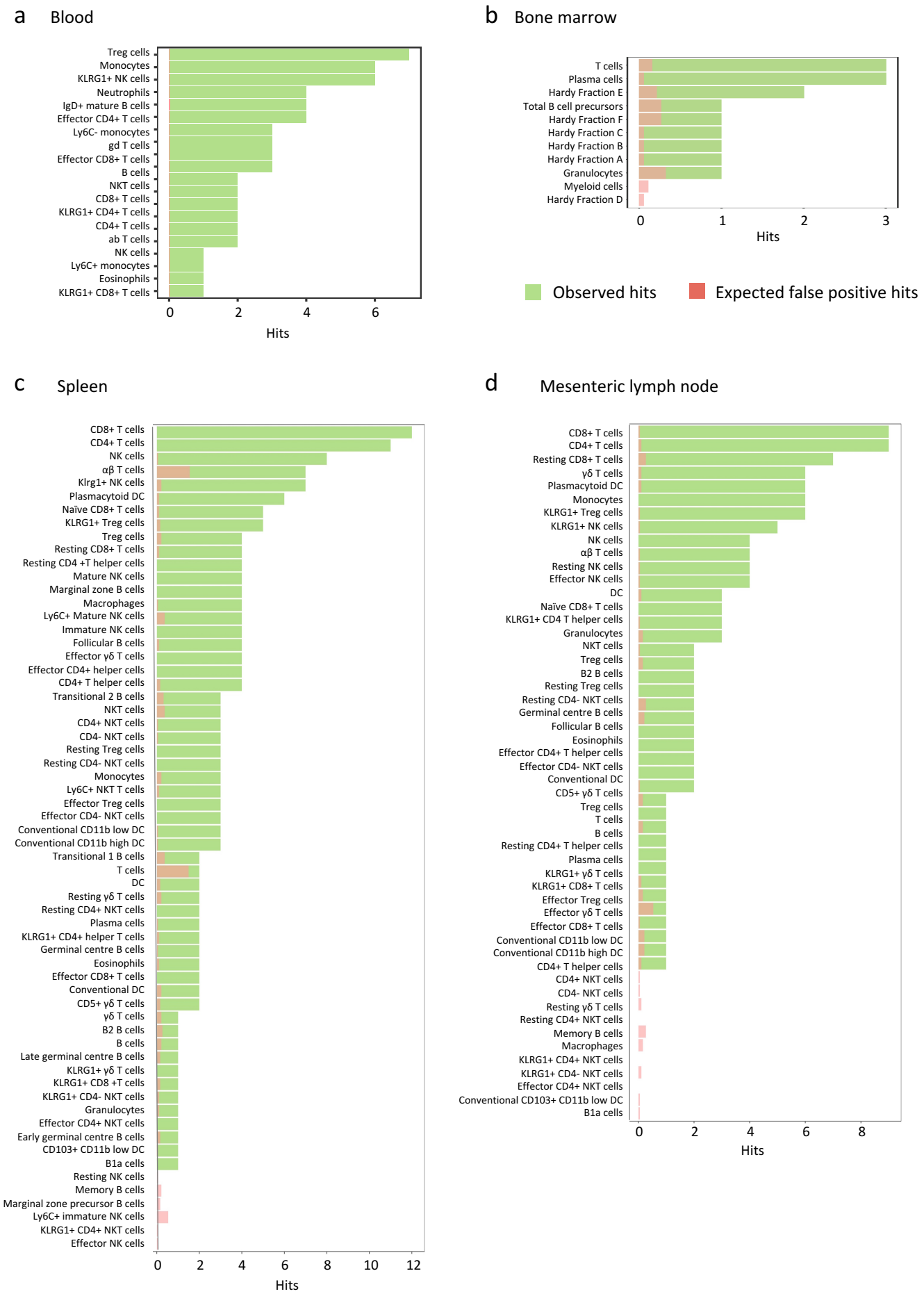

Supplementary Figure 5

a

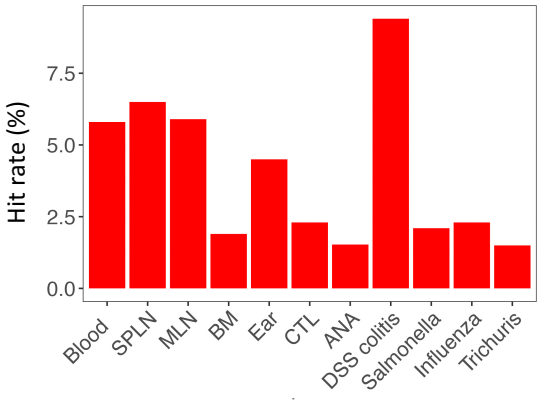

b

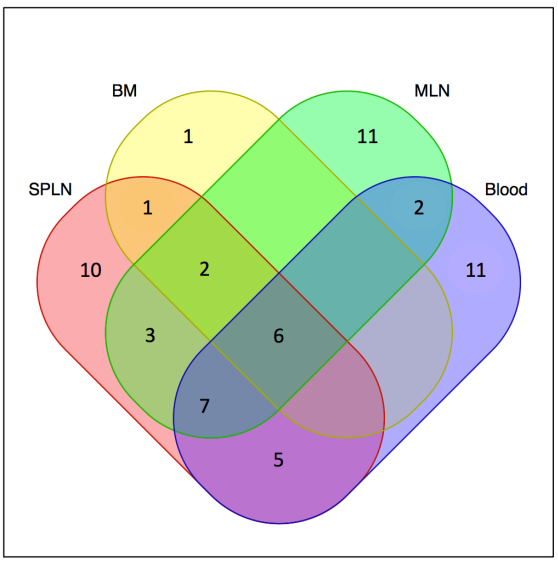

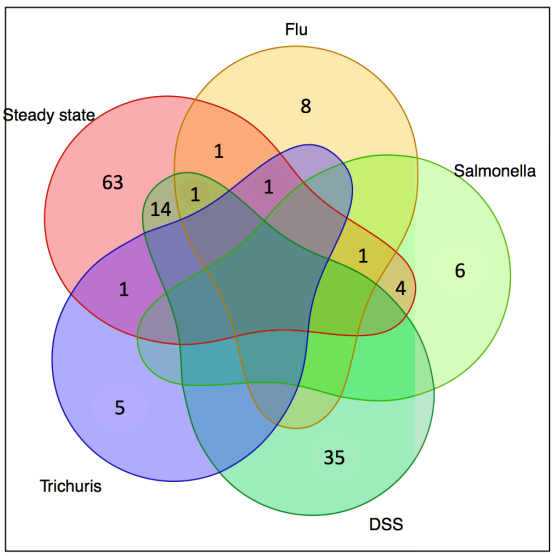

Supplementary Figure 6

a

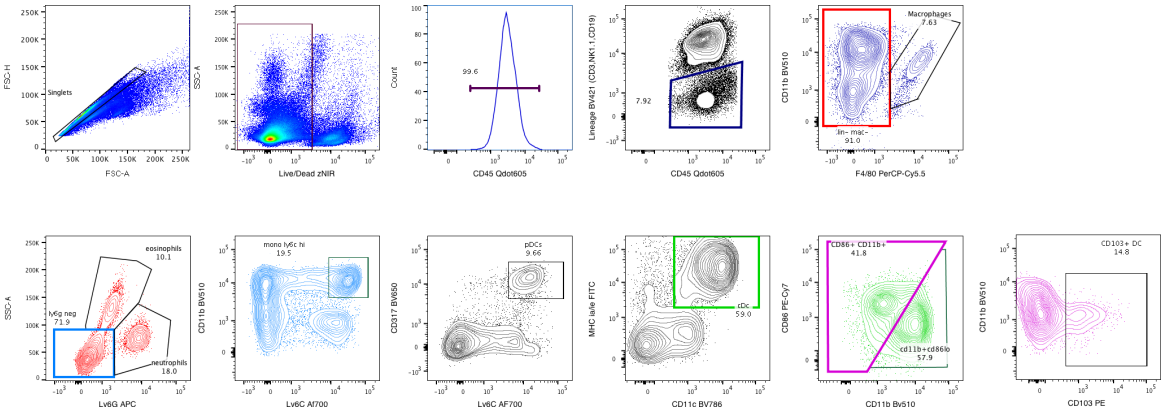

b

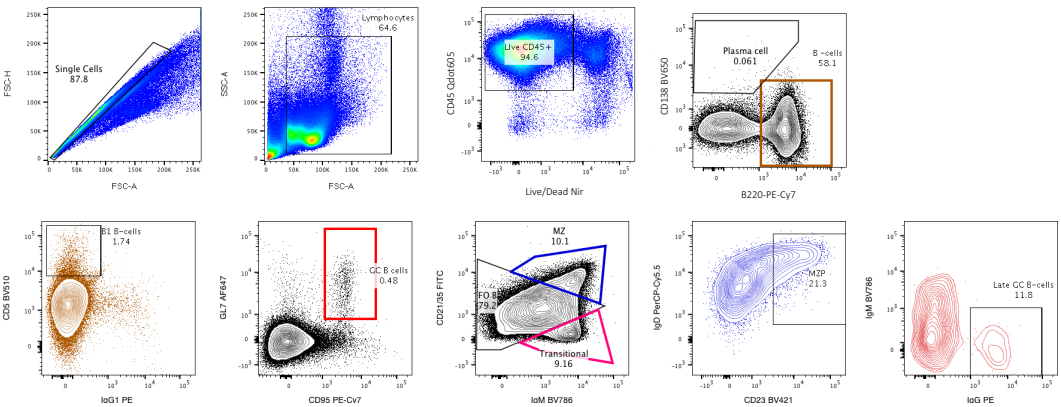

c

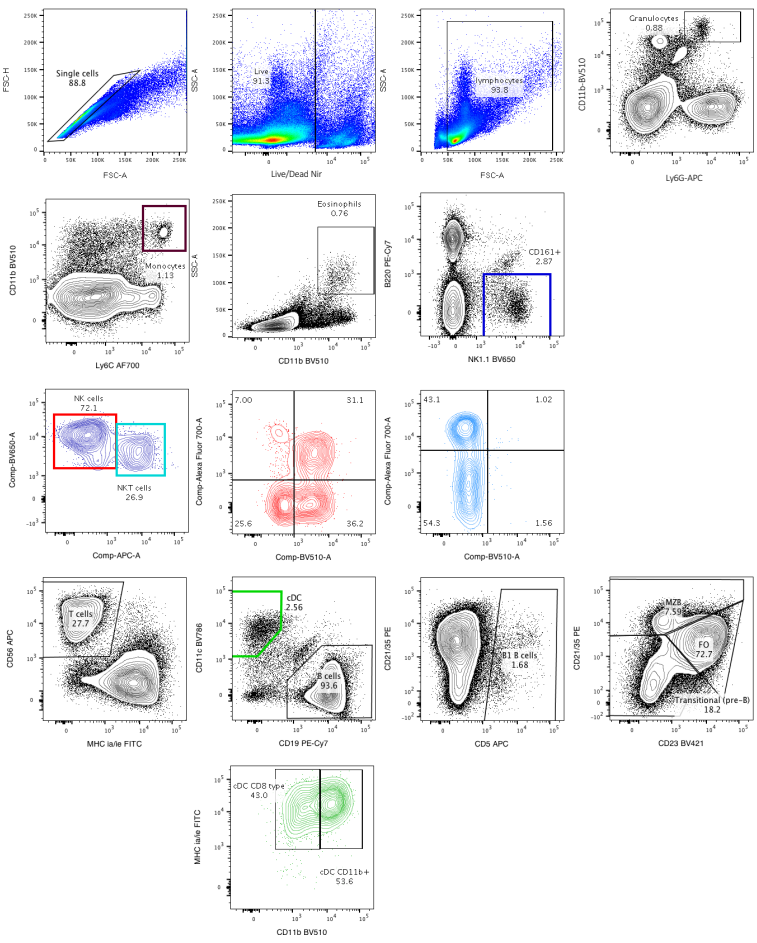

d

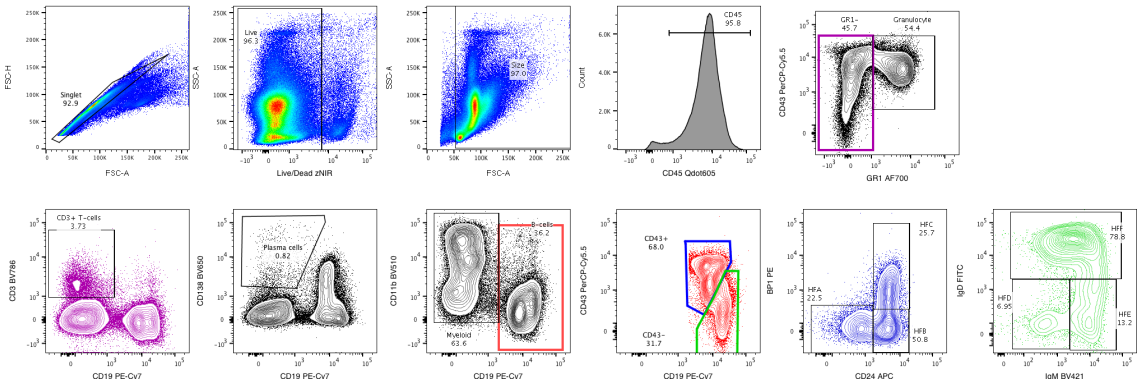
Singlet
92.9
Live
96.3
Live
97.0
CD45
95.8
GR1-
45.7
Granulocyte
54.4
CD3+ T-cells
3.73
Plasma cells
0.82
B-cells
36.2
Myeloid
63.6
CD43+
68.0
CD43-
31.7
HFC
25.7
HFA
22.5
HFB
50.8
HFF
78.8
HFD
6.95
HFE
13.2

e

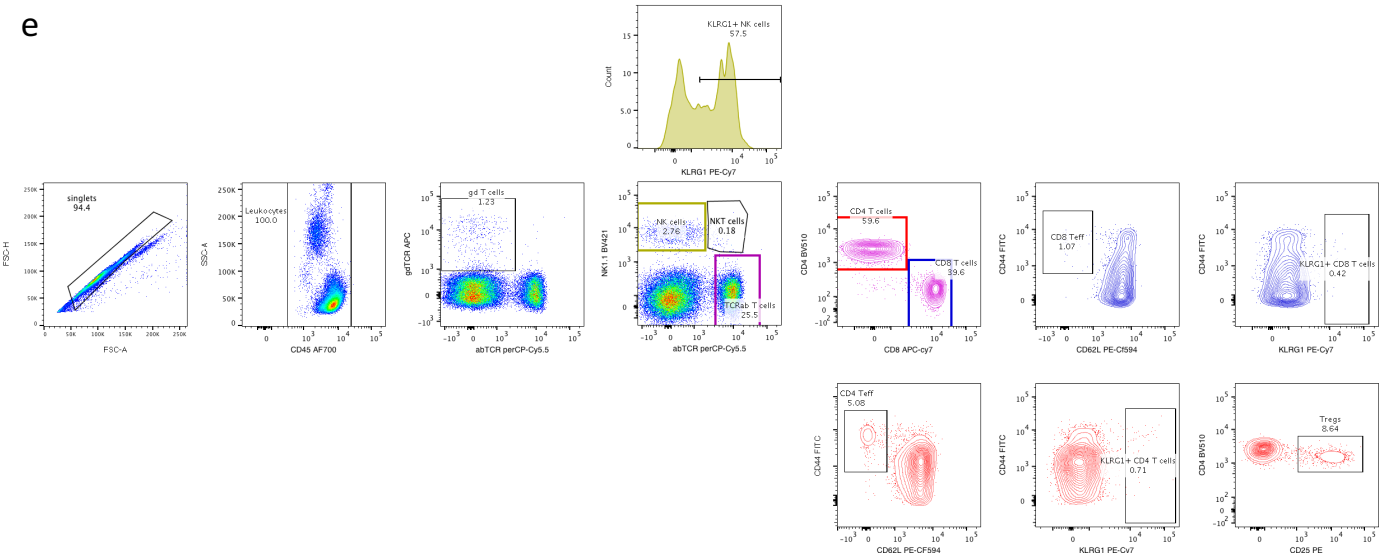
KLRG1+ NK cells
57.5
singlets
94.4
Leukocytes
100.0
gd T cells
1.23
NK cells
2.76
NKT cells
0.18
TCRab T cells
25.5
CD4 T cells
59.6
CD8 T cells
39.6
CD8 Teff
1.07
KLRG1+ CD8 T cells
0.42
CD4 Teff
5.08
KLRG1+ CD4 T cells
0.71
Tregs
8.64

f

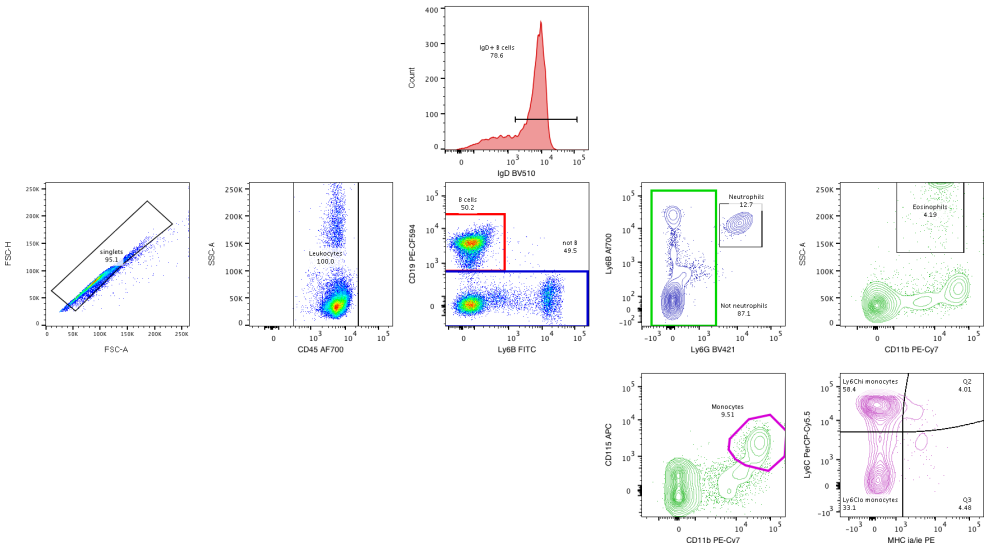
IgD+ B cells
78.6
singlets
95.1
Leukocytes
100.0
B cells
50.2
not B
49.5
Neutrophils
12.7
Not neutrophils
87.1
Eosinophils
4.19
Monocytes
9.51
Ly6Chi monocytes
58.4
Q2
4.01
Ly6Clo monocytes
33.1
Q3
4.48

Supplementary Figure 1: Assay overview.

a. Overview of the IMPC tests performed at Wellcome Trust Sanger Institute (WTSI) prior to the substantial expansion by 3i.

b. Flow cytometry screen. Representative MLN data illustrate gating strategy for T cells, NKT cells and NK cells. Subsets of key populations are shown in gates of the same colour. Percentages denote percentages of parent population. Panels can be found in Supplementary Table 1, populations are quantitated in Supplementary Table 2.

c. Epidermis screen. Left panel: Maximal intensity projection of a z-stack 2-channel overlay. Pseudocolouring scheme was applied to represent Dendritic Epidermal Vγ5$^+$ γδ T Cells (DETC) in red and MHC-II+ Langerhans cells (LC) in cyan, scale bar 50 µm. Middle panel: 3D quantitative object-based image analysis (Definiens Developer XD) of DETC that contact LC (red) versus not contacting LC (yellow), and LC (cyan); scale bar: 50 µm. Right panel: 3D representation of a DETC rendering in Definiens Developer from which parameters such as dendricity and roundness were quantitated; scale bar: 10 µm. Measurements were performed on three vision fields from the same slide per animal.

d. ANA screen. Antinuclear antibody staining in Hep2 cells using serum from wt mice and different ko lines. Sera were scored on a scale of 0 to 4. The images illustrate that sera from wt or specific mutant strains do not all score equally. Scores of $\leq$1 were regarded as negative; scores of $\geq$2 as positive. Test performed once per animal.

e. DSS histology screen. Left: Body weight curves of wt and *Arhgef1*$^{-/-}$ mice in the same experiment (n=4[2M2F] for wt; n=4[2M2f] for *Arhgef1*$^{-/-}$). Middle: histopathology scores of wt and *Arhgef1*$^{-/-}$ mice. Symbols denote the average histopathology score for mid- and distal-colon in each mouse, and horizontal bars represent the median across mice for this group. Right: representative photomicrographs of H&E-stained colonic sections of wt and *Arhgef1*$^{-/-}$ mice; scale bar 0.2 mm. One mid-colon and one distal colon section scored per animal.

f. Longitudinal monitoring of manually analysed flow cytometry data for quality controls (QC), illustrated by CD4$^+$ T helper cells. Daily inner quantiles are shaded dark blue, outer quantiles light blue, middle line is daily median. All individual data points

are shown. Temporal QC are further considered in Materials and Methods.

g. Top GO-slim categories (all categories with raw p-value < 0.01 shown, two-sided Fisher's exact test) among 466 of genes with GO annotation in 3i gene set. X axis: number of genes from given category in the 3i set. Coloured by ratio of observed to expected number of genes. Red frame: immune-system related categories. Categories significantly different from whole mouse genome at FDR 5% marked with asterisk.

h. Variation in immune cell subsets (colours denote cell lineages) detected by flow cytometry (denoted by size of circles). Data from 16-week old wt C57BL/6N SPL (n>500 for all parameters).

i. Variation and sexual dimorphism in analyses of ear epidermal microscopy; CD8 cytotoxicity; DSS colitis; and ANA. Lower panel: sexual dimorphism of mean values as log2 fold change (middle panel, female/male); colour indicates p value (two tailed unpaired t test) Upper panel: coefficient of variation; colour indicates assay. Number of wt samples for each of the assays are listed in Supplementary Table 3.

Supplementary Figure 2: Immunological correlations across parameters

Heat map represents Pearson correlations of 46 splenic immune cell subsets with each other in wt females (n>230 for all parameters) as determined by flow cytometry. Dark red fields denote strong positive, dark blue fields strong negative correlations.

Supplementary Figure 3: Non-immunological correlations across parameters

Correlations of nonimmune parameters (haematological, clinical blood chemistry, and additional data) in males (a) and females (b). Depicted are correlations with an R-value >0.33 and p<0.001; red lines denote positive correlations; blue lines, negative correlations (n>780 per sex for all parameters).

Supplementary Figure 4: False positive rates are far below hit rates.

Expected number of false positives estimated by simulation (re-sampling of wt controls, performed 10000 times and adjusted to the actual number of performed tests per parameter) compared to the number of significant phenotypes detected in: (a) PBL

(n>450 per sex for all parameters), (b) BM (n>350 per sex for all parameters), (c) SPL (n>250 per sex for all parameters), and (d) MLN (n>250 per sex for all parameters). Observed hits depicted in green; expected false positives in red. Significance established by windowed 70 wt mice reference range, details in Materials and Methods.

Supplementary Figure 5: 140 out of 530 genes perturb the immunophenotype

a. Hit rate per assay.
b. Venn diagrams showing the overlap of significantly different phenotypes between assays.

Supplementary Figure 6: Flow cytometry gating strategies**.** Subsets of key populations are shown in gates of the same colour. Percentages denote percentages of parent population. Panels can be found in Supplementary Table 1, populations are quantitated in Supplementary Table 2. T cells from spleen can be found in Supplementary Fig 1b. Representative data for:

a. Myeloid cells (data from spleen)
b. B cells (data from spleen)
c. Additional NK subsets (data from spleen)
d. Bone marrow
e. T/NK cells (data from blood)
f. B cells/monocytes (data from blood)

Supplementary Tables 1-5

Supplementary Table 1

Markers and fluorochromes used to identify immune cell populations by flow cytometry

Laser	LP Filter	BP filter	Fluoro-chrome	SPL/MLN T/NK cells	SPL/MLN B cells	SPL/MLN Myeloid cells	SPL Myeloid / B cells	Bone marrow
405	-	450/50	BV421	Klrg1	CD23	CD5/19/161	CD23	IgM
405	505	525/50	BV510	CD5	CD5	CD11b	CD11b	CD11b
405	595	610/20	Qdot-605	CD45	CD45	CD45		CD45
405	630	670/30	BV650	CD161	CD138	CD317	CD161	CD138
405	750	780/60	BV786	CD4	IgM	CD11c	CD11c	CD3
488	505	530/30	FITC	CD44	CD21/35	MHC II	MHC II	IgD
488	685	710/50	PerCP-Cy5.5	CD62L	IgD	F4/80		CD43
561	570	585/15	PE	GITR	IgG1	CD103	CD21/35	BP-1
561	750	780/60	PE-Cy7	TCRδ	CD95	CD86	CD19	B220
640	-	670/14	APC	CD25		Ly6G	CD5	CD24
			AF647		GL7			
640	690	730/45	AF700	CD8α	B220	Ly6C	Ly6C	Gr1
640	750	780/60	NIR	Live/Dead	Live/Dead	Live/Dead	Live/Dead	Live/Dead

Laser	LP Filter	BP filter	Fluoro-chrome	PBL T/NK cells	PBL Myeloid/ B cells
405	-	450/50	BV421	CD161	
			V450		Ly6G
405	505	525/50	BV510	CD4	IgD
488	505	530/30	FITC	CD44	Ly6B
488	550	575/26	PE	CD25	MHC II
488	600	610/20	PE-CF594	CD62L	CD19
488	685	695/40	PerCP-Cy5.5	TCRβ	Ly6C
488	755	780/60	PE-Cy7	Klrg1	CD11b
633	-	660/20	APC	TCRδ	CD115
633	710	730/45	AF700	CD45	CD45
633	755	780/60	APC-H7	CD8α	

Supplementary Table 2: Parameters of flow cytometry and ear epidermis assays

Parameter	Cell markers
Spleen and mesenteric lymph node	
Total γδ T cells	TCRδ+
CD5+ γδ T cells	TCRδ+ CD5+
Effector γδ T cells	TCRδ+ CD62L- CD44+
Resting γδ T cells	TCRδ+ CD62L+
KLRG1+ γδ T cells	TCRδ+ KLRG1+
Total αβ T cells	TCRδ- CD5+ CD4+ or CD8+
Total CD4+ T cells	TCRδ- CD5+ CD4+
CD4+ T helper cells	TCRδ- CD5+ CD4+ CD25- GITR-
Effector CD4+ T helper cells	TCRδ- CD5+ CD4+ CD25- GITR- CD62L- CD44+
Resting CD4+ T helper cells	TCRδ- CD5+ CD4+ CD25- GITR- CD62L+
KLRG1+ CD4+ T helper cells	TCRδ- CD5+ CD4+ CD25- GITR- KLRG1+
Total T_{reg} cells	TCRδ- CD5+ CD4+ CD25+ GITR+
Effector T_{reg} cells	TCRδ- CD5+ CD4+ CD25+ GITR+ CD62L- CD44+
Resting T_{reg} cells	TCRδ- CD5+ CD4+ CD25+ GITR+ CD62L+
KLRG1+ T_{reg} cells	TCRδ- CD5+ CD4+ CD25+ GITR+ KLRG1+
Total CD8+ T cells	TCRδ- CD5+ CD8+
Effector CD8+ T cells	TCRδ- CD5+ CD8+ CD62L- CD44+
Resting CD8+ T cells	TCRδ- CD5+ CD8+ CD62L+ CD44+
Naive CD8+ T cells	TCRδ- CD5+ CD8+ CD62L+ CD44-
KLRG1+ CD8+ T cells	TCRδ- CD5+ CD8+ KLRG1+
Total NKT cells	TCRδ- CD5+ CD161+
Total CD4- NKT cells	TCRδ- CD5+ CD161+ CD4-
Effector CD4- NKT cells	TCRδ- CD5+ CD161+ CD4- CD62L-
Resting CD4- NKT cells	TCRδ- CD5+ CD161+ CD4- CD62L+
KLRG1+ CD4- NKT cells	TCRδ- CD5+ CD161+ CD4- KLRG1+
Total CD4+ NKT cells	TCRδ- CD5+ CD161+ CD4+
Effector CD4+ NKT cells	TCRδ- CD5+ CD161+ CD4+ CD62L-
Resting CD4+ NKT cells	TCRδ- CD5+ CD161+ CD4+ CD62L+
KLRG1+ CD4+ NKT cells	TCRδ- CD5+ CD161+ CD4+ KLRG1+
Total NK cells	TCRδ- CD5- CD161+
Effector NK cells	TCRδ- CD5- CD161+ CD62L-
Resting NK cells	TCRδ- CD5- CD161+ CD62L+
KLRG1+ NK cells	TCRδ- CD5- CD161+ KLRG1+
Plasma cells	CD138+
B1a cells	CD138- B220+ CD5+
B2 cells	CD138- B220+ CD5-
Follicular B cells	CD138- B220+ CD5- GL7- CD95- CD21/35^{int} IgM^{int}
Memory B cells	CD138- B220+ CD5- GL7- CD95- IgG+
Macrophages	F4/80+ CD11b^{int}
Granulocytes	F4/80- Ly6G^{high} CD11b+
Eosinophils	F4/80- Ly6G^{int} CD11b+ SSC^{high}

Monocytes	F4/80- Ly6G- Ly6C^{high} CD11b+
Plasmacytoid DC	F4/80- Ly6G- Ly6C$^{low/int}$ CD317+
Conventional DC	F4/80- Ly6G- Ly6C$^{low/int}$ CD317- CD11c+ MHCII+
Conventional CD11b^{high} DC	F4/80- Ly6G- Ly6C$^{low/int}$ CD317- CD11c+ MHCII+ CD11b^{high} CD86^{low}
Conventional CD11b^{low} DC	F4/80- Ly6G- Ly6C$^{low/int}$ CD317- CD11c+ MHCII+ CD11b^{low} CD86^{high}
CD103+ conventional CD11b^{low} DC	F4/80- Ly6G- Ly6C$^{low/int}$ CD317- CD11c+ MHCII+ CD11b^{low} CD86^{high} CD103+
Spleen only	
Immature NK cells	Ly6G- CD161+ CD5- CD11b- Ly6C-
Ly6C+ immature NK cells	Ly6G- CD161+ CD5- CD11b- Ly6C+
Mature NK cells	Ly6G- CD161+ CD5- CD11b+ Ly6C-
Ly6C+ mature NK cells	Ly6G- CD161+ CD5- CD11b+ Ly6C+
Germinal centre B cells	CD138- B220+ CD5- GL7+ CD95+
Early germinal centre B cells	CD138- B220+ CD5- GL7+ CD95+ IgM+ IgG-
Late germinal centre B cells	CD138- B220+ CD5- GL7+ CD95+ IgM- IgG+
Marginal zone precursor B cells	CD138- B220+ CD5- GL7- CD95- CD21/35+ CD23-
Marginal zone B cells	CD138- B220+ CD5- GL7- CD95- CD21/35+ CD23+
Transitional 1 B cells	CD138- B220+ CD5- GL7- CD95- CD21/35- CD23-
Transitional 2 B cells	CD138- B220+ CD5- GL7- CD95- CD21/35- CD23+
Blood	
Total T cells	TCRβ+ or TCRδ+
Total αβ T cells	TCRβ+
Total CD4+ T cells	TCRβ+ CD4+
Effector CD4+ T cells	TCRβ+ CD4+ CD62L- CD44+
KLRG1+ CD4+ T cells	TCRβ+ CD4+ KLRG1+
Total T_{reg} cells	TCRβ+ CD4+ CD25+
Total CD8+ T cells	TCRβ+ CD8+
Effector CD8+ T cells	TCRβ+ CD8+ CD62L- CD44+
KLRG1+ CD8+ T cells	TCRβ+ CD8+ KLRG1+
Total γδ T cells	TCRδ+
Total NKT cells	TCRβ+ CD161+
Total NK cells	TCRβ- CD161+
KLRG1+ NK cells	TCRβ- CD161+ KLRG1+
Total B cells	CD19+
IgD+ mature B cells	CD19+ IgD+
Monocytes	CD19- Ly6G- CD11b+
Ly6C+ monocytes	CD19- Ly6G- CD11b+ Ly6C+
Ly6C- monocytes	CD19- Ly6G- CD11b+ Ly6C-

Neutrophils	CD19- Ly6G+ Ly6B+
Eosinophils	CD19- Ly6B- Ly6G- SSC^{high} CD11b+
Bone marrow	
Granulocytes	GR+ CD43+
T cells	GR- CD3+
Plasma cells	GR- CD3- CD138+
Myeloid cells	GR- CD3- CD138- CD11b+
Total B cell precursors	GR- CD3- CD138- B220+
Pre-pro B cells (Hardy fraction A)	GR- CD3- CD138- B220+ CD43+ BP1- CD24-
Pro-B cells (Hardy fraction B)	GR- CD3- CD138- B220+ CD43+ BP1- CD24+
Pro-B cells (Hardy fraction C)	GR- CD3- CD138- B220+ CD43+ BP1+ CD24+
Pre-B cells (Hardy fraction D)	GR- CD3- CD138- B220+ CD43- IgD- IgM-
Immature B cells (Hardy fraction E)	GR- CD3- CD138- B220+ CD43- IgD- IgM+
Mature B cells (Hardy fraction F)	GR- CD3- CD138- B220+ CD43- IgD+ IgM+
Ear epidermis	
DETC coverage	
Count of DETC Vγ5+	
Count of atypical CD45+ cells	
Count of DETC Vγ5+ contacting LC	
Count of DETC Vγ5+ not contacting LC	
Count of LC	
Average volume of DETC Vγ5+	
Average volume of atypical CD45+ cells	
Average volume of DETC Vγ5+ contacting LC	
Average volume of DETC Vγ5+ not contacting LC	
Average volume of LC	
Average roundness of DETC Vγ5+	
Average roundness of atypical CD45+ cells	
Average roundness of DETC Vγ5+ contacting LC	
Average roundness of DETC Vγ5+ not contacting LC	
Average roundness of LC	
Average number of branches on DETC Vγ5+	
Average number of branches on DETC Vγ5+ contacting LC	
Average number of branches on DETC Vγ5+ not contacting LC	
Average number of branches on LC	
Average branch length of on DETC Vγ5+	
Average branch length of on DETC Vγ5+ contacting LC	
Average branch length of on DETC Vγ5+ not contacting LC	

Supplementary Table 3: Summary of statistical procedures per assay and readout

Assay	Readouts	Statistical test	Choice of controls	Successfully phenotyped strains/mice
Ear epidermis (2F, 2M)	Number of cells and morphological parameters recorded by 3D confocal analysis and analysed by an automated script using Definiens developer software	Mutant samples were considered phenodeviant when falling into the lower or upper 2.5 percentiles of the wild type distribution of their respective sex. A mutant line was considered phenodeviant when ≥60% of samples across sexes (3/4 or 3/3) fell outside their respective reference range.	all wt data, sex-matched	496 genes 499 strains 2066 ko mice 728 wt mice
Cytotoxic T cell lysis (2F, 2M)	Percentage of target cell lysis recorded relative to a positive control (detergent)	As for ear epidermis. A sample was considered outside the reference range if three consecutive points in the target:effector ratio fell outside the reference range for this ratio.	all wt data, sex-matched	263 genes 265 strains 1130 ko mice 566 wt mice
Blood (7F, 7M)	Frequencies/cell numbers of cell populations recorded by flow cytometry. Frequencies are reported as a percentage of parental population, absolute numbers are calculated using white blood cell counts from haematology data.	As for ear epidermis, but owing to the larger sample size, phenodeviants were also identified within each sex separately.*	all wt data, sex-matched	530 genes 533 strains 7010 ko mice 2652 wt mice
Spleen/ MLN/BM (3F, 3M)	Frequencies of cell populations recorded by flow cytometry.	As for ear epidermis. A mutant line was considered phenodeviant when ≥60% of samples	70 sex matched wt samples that were	Spleen: 517 genes 520 strains 3169 ko mi.

	Frequencies are reported as a percentage of parental population or as percentage of $CD45^+$, live, single cells.	across sexes (6/6, 5/6, 4/6, 3/5, 3/4 or 3/3) fell outside their respective reference range.	closest in time to the mutant sample assessed.	947 wt mice MLN: 508 genes 511 strains 2986 ko mi. 858 wt mice Bone marrow: 479 genes 482 strains 2622 ko mi. 795 wt mice
DSS histology and weight data (2F, 2M or 4F)	A) Histological scoring of gut sections B) Percentage of reduction in body weight compared to the start of the experiment.	As for ear epidermis	sex-matched wt data, 70 individuals closest in starting weight (A) or age (B)	489 genes 492 strains 2001 ko mice 868 wt mice
Salmonella bacterial burden and serum antibodies (4F, 4M)	A) Colony forming units (CFU) of bacteria cultured on LB agar isolated from spleen and liver homogenates B) Titers of antigen-specific antibodies in serum measured by ELISA	Hits were identified by a Mann-Whitney-U test with a p-value cut-off of 0.05 in comparison to concurrent wt controls, combining data from male and female mice. Significant lines were retested with a second cohort. A final call was made on the combined data from both experiments.	concurrent wt controls	516 genes 518 strains 4133 ko mice 1723 wt mice
Influenza weight data: (3F, 3M)	Percentage of reduction in body weight compared to the start of the experiment.	Hits were identified by fitting a robust mixed model (corresponding to two-way Anova) with a p-value cut-off of 0.0001, in comparison to concurrent wt controls, taking into account sex and genotype, using the R package Phenstat[61]. Residuals were assumed	concurrent wt controls	489 genes 490 strains 3033 ko mice 1054 wt mice

		to be normally distributed.		
ANA (3F, 3M)	Scores for ANA positivity assessed by microscopy and analysed using a Python script. Scores from 0 to 1.5 were considered negative; scores of 2- 4 positive.	Hits were identified by Fisher's exact test with a p-value cut-off of 0.01, comparing the frequency of positive samples in mutant and wt	wt animals from the contempor-aneous 3 months' period	518 genes 520 strains 3286 ko mice 1123 wt mice
Trichuris (6F)	Presence or absence of worms in the cecum on day 33 as categorical measure.	Hits were identified by Fisher's exact test with a p-value cut-off of 0.01, comparing the frequency of positive samples in mutant and wt.	all wt animals	287 genes 289 strains 1704 ko mice 431 wt mice
DSS and influenza survival data	Number of mice having to be culled because of excessive weight loss before the end of the experiment	Hits were identified by Fisher's exact test with a p-value cut-off of 0.01, comparing the frequency of mice with above threshold weight loss in a mutant strain with wt population, combining data from both sexes.	all wt animals	as for DSS and influenza above

*Please note that Blood hits are analysed with a mixed model on the IMPC website as the IMPC statistical pipeline was not offering the option of a reference range approach at the time of writing. The number of hits for blood is therefore higher on the IMPC website.

Supplementary Table 4: Alleles of knockout lines included in the study

1700001C02Rik$^{tm1a(EUCOMM)Wtsi}$	*Dpy30*$^{tm1a(KOMP)Wtsi}$	*Pclaf*$^{tm1a\ (EUCOMM)Wtsi}$
1700007K13Rik$^{tm2b(EUCOMM)Wtsi}$	*Duoxa2*$^{tm1b(KOMP)Wtsi}$	*Pdcd2*$^{tm1b(EUCOMM)Wtsi}$
1700011A15Rik$^{tm1a(KOMP)Wtsi}$	*Dusp5*$^{tm1a(KOMP)Wtsi}$	*Pdia4*$^{tm1b\ (EUCOMM)Wtsi}$
1700024P04Rik$^{tm1b(EUCOMM)Wtsi}$	*Dynlrb2*$^{tm1a(KOMP)Wtsi}$	*Pdk3*$^{tm2a(KOMP)Wtsi}$
1700029H14Rik$^{tm2b(KOMP)Wtsi}$	*Eci3*$^{tm1b(EUCOMM)Wtsi}$	*Pdzk1*$^{tm2b(EUCOMM)Wtsi}$
1700034J05Rik$^{tm1a(KOMP)Wtsi}$	*Eif3h*$^{tm1a(EUCOMM)Hmgu}$	*Pepd*$^{tm1a(KOMP)Wtsi}$
1700067K01Rik$^{tm2a(KOMP)Wtsi}$	*Elac2*$^{tm1b(EUCOMM)Wtsi}$	*Pgap2*$^{tm1b(EUCOMM)Wtsi}$
1700112E06Rik$^{tm1e(EUCOMM)Wtsi}$	*Ell2*$^{tm1b(EUCOMM)Wtsi}$	*Pigf*$^{tm1a(KOMP)Wtsi}$
1700123O20Rik$^{tm1a(EUCOMM)Wtsi}$	*Enc1*$^{tm1a(EUCOMM)Wtsi}$	*Pigl*$^{tm1b(KOMP)Wtsi}$
2010300C02Rik$^{tm1b(KOMP)Wtsi}$	*Enthd2*$^{tm1b(KOMP)Wtsi}$	*Pitrm1*$^{tm1a(KOMP)Wtsi}$
2610034B18Rik$^{tm1b(EUCOMM)Wtsi}$	*Erlin2*$^{tm1a(EUCOMM)Wtsi}$	*Pitx1*$^{em1(IMPC)Wtsi}$
3300002A11Rik$^{tm1a(KOMP)Wtsi}$	*Evi5*$^{tm1a(KOMP)Wtsi}$	*Pla2g6*$^{tm1a(EUCOMM)Wtsi}$
3830406C13Rik$^{tm1b(KOMP)Wtsi}$	*Exoc3l2*$^{tm1b(KOMP)Wtsi}$	*Pld3*$^{tm1e(EUCOMM)Wtsi}$
4930404H24Rik$^{tm1a(KOMP)Wtsi}$	*Exosc9*$^{tm1b(EUCOMM)Wtsi}$	*Plet1*$^{em1(IMPC)Wtsi}$
4930590J08Rik$^{tm1a(EUCOMM)Wtsi}$	*Fads3*$^{tm1b(EUCOMM)Wtsi}$	*Plscr2*$^{tm1b(KOMP)Wtsi}$
4931429L15Rik$^{tm1a(EUCOMM)Wtsi}$	*Fam122c*$^{tm1b(EUCOMM)Wtsi}$	*Plxnb3*$^{tm1a(KOMP)Wtsi}$
4932431P20Rik$^{em1(IMPC)Wtsi}$	*Fam160a1*$^{tm1b(EUCOMM)Wtsi}$	*Polb*$^{tm1a(KOMP)Wtsi}$
4933402N03Rik$^{tm2a(KOMP)Wtsi}$	*Fam163a*$^{tm2b(KOMP)Wtsi}$	*Pold3*$^{tm1b(EUCOMM)Wtsi}$
4933434E20Rik$^{tm1a(EUCOMM)Wtsi}$	*Fam212b*$^{tm1a(KOMP)Wtsi}$	*Polr3f*$^{tm1a(EUCOMM)Wtsi}$
5730559C18Rik$^{tm2a(EUCOMM)Wtsi}$	*Fam47e*$^{tm1a(EUCOMM)Wtsi}$	*Polr3g*$^{tm1a(EUCOMM)Wtsi}$
9330182L06Rik$^{tm1a(KOMP)Wtsi}$	*Fam69a*$^{tm1a(EUCOMM)Wtsi}$	*Ppil3*$^{tm1b(EUCOMM)Wtsi}$
A430005L14Rik$^{tm1a(KOMP)Wtsi}$	*Fam71b*$^{tm1a(KOMP)Wtsi}$	*Prame*$^{tm1a(KOMP)Wtsi}$
A430078G23Rik$^{tm1a(KOMP)Wtsi}$	*Fam92a*$^{tm1b(KOMP)Wtsi}$	*Prkab1*$^{tm1b(KOMP)Wtsi}$
A730017C20Rik$^{tm1b(KOMP)Wtsi}$	*Fbf1*$^{tm1a(EUCOMM)Wtsi}$	*Prrc2b*$^{tm1a(EUCOMM)Wtsi}$
Abhd14a$^{tm2a(EUCOMM)Wtsi}$	*Fbxo33*$^{tm1b(EUCOMM)Wtsi}$	*Prrg2*$^{tm1b(EUCOMM)Wtsi}$
Abhd17a$^{tm1a(KOMP)Wtsi}$	*Fbxw26*$^{tm1b(KOMP)Wtsi}$	*Prrt2*$^{tm1a(KOMP)Wtsi}$
Acbd5$^{tm1b(EUCOMM)Wtsi}$	*Fdft1*$^{tm1a(KOMP)Wtsi}$	*Prss52*$^{tm2a(KOMP)Wtsi}$
Acer1$^{tm1a(EUCOMM)Wtsi}$	*Fkbp3*$^{tm2a(EUCOMM)Wtsi}$	*Psph*$^{tm1a(EUCOMM)Hmgu}$
Actl10$^{tm1a(EUCOMM)Wtsi}$	*Fnip2*$^{tm1a(KOMP)Wtsi}$	*Pth1r*$^{tm1a(EUCOMM)Hmgu}$
Adal$^{tm1a(EUCOMM)Wtsi}$	*Fryl*$^{tm1b(KOMP)Wtsi}$	*Pth*$^{tm1a(EUCOMM)Wtsi}$
Adamts19$^{tm4a(EUCOMM)Wtsi}$	*Fxyd3*$^{tm1a(KOMP)Wtsi}$	*Ptprd*$^{tm2a(KOMP)Wtsi}$

Adamts3$^{tm1b(KOMP)Wtsi}$	*Fzd6*$^{tm2a(EUCOMM)Wtsi}$	*Pwp1*$^{tm1a(EUCOMM)Wtsi}$
Adap1$^{tm1a(EUCOMM)Wtsi}$	*Galnt18*$^{tm1b(KOMP)Wtsi}$	*Pycr2*$^{tm1a(EUCOMM)Wtsi}$
Adcy2$^{tm1a(KOMP)Wtsi}$	*Galntl5*$^{tm1b(KOMP)Wtsi}$	*Rab17*$^{tm1a(KOMP)Wtsi}$
Adcy9$^{tm1b(EUCOMM)Wtsi}$	*Gbp5*$^{em1(IMPC)Wtsi}$	*Rab21*$^{tm1b(KOMP)Wtsi}$
Adgrd1$^{tm1b(EUCOMM)Wtsi}$	*Gda*$^{tm1a(KOMP)Wtsi}$	*Raph1*$^{tm1b(EUCOMM)Wtsi}$
Adpgk$^{tm2a(EUCOMM)Wtsi}$	*Gdpd2*$^{tm1a(KOMP)Wtsi}$	*Rbak*$^{tm1b(KOMP)Wtsi}$
Agap1$^{tm1a(EUCOMM)Wtsi}$	*Gimap6*$^{tm1a(KOMP)Wtsi}$	*Rbm14*$^{tm1a(KOMP)Wtsi}$
Aicda$^{tm1b(EUCOMM)Hmgu}$	*Glo1*$^{tm1a(KOMP)Wtsi}$	*Rbm33*$^{tm1b(EUCOMM)Wtsi}$
Aldh1b1$^{tm2a(EUCOMM)Wtsi}$	*Glyatl3*$^{em1(IMPC)Wtsi}$	*Rbm47*$^{tm1a(EUCOMM)Wtsi}$
Aldh3b1$^{tm1b(EUCOMM)Wtsi}$	*Gm12253*$^{tm1a(KOMP)Wtsi}$	*Rbmx*$^{tm2b(KOMP)Wtsi}$
Alox12e$^{tm1b(EUCOMM)Wtsi}$	*Gm13119*$^{tm2b(KOMP)Wtsi}$	*Reg3d*$^{tm1b(EUCOMM)Wtsi}$
Alpk1$^{em1(IMPC)Wtsi}$	*Gm13125*$^{tm1b(KOMP)Wtsi}$	*Repin1*$^{tm1a(EUCOMM)Wtsi}$
Amz2$^{tm1e(KOMP)Wtsi}$	*Gm16432*$^{tm1b(KOMP)Wtsi}$	*Rida*$^{tm1a(KOMP)Wtsi}$
Ankrd13d$^{tm1a(KOMP)Wtsi}$	*Gm16515*$^{tm1b(EUCOMM)Wtsi}$	*Rimbp2*$^{em1(IMPC)Wtsi}$
Ankrd6$^{tm1b(KOMP)Wtsi}$	*Gm5544*$^{tm1a(KOMP)Wtsi}$	*Rnasek*$^{tm1b(EUCOMM)Wtsi}$
Ankrd9$^{tm1(KOMP)Wtsi}$	*Gmds*$^{tm1a(KOMP)Wtsi}$	*Rnf10*$^{tm1b(KOMP)Wtsi}$
Anks6$^{tm1b(KOMP)Wtsi}$	*Gmnc*$^{tm1b(KOMP)Wtsi}$	*Rnf125*$^{tm1a\ (EUCOMM)Wtsi}$
Ano10$^{tm1a(EUCOMM)Wtsi}$	*Gnb3*$^{tm1b(EUCOMM)Wtsi}$	*Rnf138*$^{tm1b(EUCOMM)Hmgu}$
Anxa9$^{tm1b(EUCOMM)Wtsi}$	*Gpbp1l1*$^{tm1a(EUCOMM)Wtsi}$	*Rnf157*$^{tm1b(EUCOMM)Wtsi}$
Ap2a2$^{em1(IMPC)Wtsi}$	*Gpr152*$^{tm1b(EUCOMM)Wtsi}$	*Rpia*$^{tm1a(KOMP)Wtsi}$
Ap4e1$^{tm1b(KOMP)Wtsi}$	*Gpr35*$^{tm1b(EUCOMM)Hmgu}$	*Rspo4*$^{tm1a(KOMP)Wtsi}$
Ap4m1$^{tm1b(EUCOMM)Wtsi}$	*Grb7*$^{tm1b(EUCOMM)Wtsi}$	*Rundc1*$^{tm1b(EUCOMM)Wtsi}$
Apip$^{tm1b(EUCOMM)Wtsi}$	*Grsf1*$^{tm1b(EUCOMM)Wtsi}$	*Rwdd1*$^{tm1b(KOMP)Wtsi}$
Apol9b$^{tm2a(KOMP)Wtsi}$	*Gsdme*$^{tm1b(KOMP)Wtsi}$	*Sap130*$^{tm1a(KOMP)Mbp}$
Apoo$^{tm1b(KOMP)Wtsi}$	*Gsto2*$^{tm2a(KOMP)Wtsi}$	*Scaf11*$^{em1(IMPC)Wtsi}$
Arap2$^{tm2b(EUCOMM)Wtsi}$	*Gt(ROSA)26Sor*$^{ROSA26\_Dre\_C03}$	*Selenow*$^{tm1b(EUCOMM)Wtsi}$
Arhgap17$^{tm1b(EUCOMM)Wtsi}$	*Gtf2a1*$^{tm1a(KOMP)Wtsi}$	*Sept10*$^{tm1a(KOMP)Wtsi}$
Arhgap22$^{tm1a(KOMP)Wtsi}$	*Gtf2h2*$^{tm1a(EUCOMM)Wtsi}$	*Serinc3*$^{tm1a(KOMP)Wtsi}$
Arhgef1$^{tm1a(EUCOMM)Wtsi}$	*H13*$^{tm1b(KOMP)Wtsi}$	*Setd5*$^{tm1a(EUCOMM)Wtsi}$
Arid1b$^{tm1b(EUCOMM)Hmgu}$	*Hao2*$^{em1(IMPC)Wtsi}$	*Sfxn3*$^{tm1b(KOMP)Wtsi}$
Armc7$^{tm1.1(KOMP)Wtsi}$	*Hbs1l*$^{tm1a(KOMP)Wtsi}$	*Sgms1*$^{tm1a(EUCOMM)Wtsi}$
Armh3$^{tm1a(EUCOMM)Wtsi}$	*Hecw2*$^{tm1a(EUCOMM)Wtsi}$	*Sgsm1*$^{tm1b(EUCOMM)Wtsi}$
Arpc1b$^{tm1a(EUCOMM)Wtsi}$	*Herc1*$^{em1\text{-}3(IMPC)Wtsi}$**	*Sh3bgrl3*$^{tm2b(EUCOMM)Wtsi}$

Arrdc5$^{tm1b(EUCOMM)Wtsi}$	*Hibadh*$^{tm1b(EUCOMM)Wtsi}$	*Sh3bp4*$^{tm1a(EUCOMM)Wtsi}$
Art4$^{tm1a(KOMP)Wtsi}$	*Hmgxb3*$^{tm1a(EUCOMM)Wtsi}$	*Sh3pxd2a*$^{tm1b(EUCOMM)Wtsi}$
Atad3a$^{tm1a(KOMP)Wtsi}$	*Homez*$^{tm1e(KOMP)Wtsi}$	*Sik3*$^{tm1a(EUCOMM)Hmgu}$
Atg16l2$^{tm1a(EUCOMM)Wtsi}$	*Hpf1*$^{em1(IMPC)Wtsi}$	*Slamf9*$^{tm1b(EUCOMM)Wtsi}$
Atp11a$^{tm1a(KOMP)Wtsi}$	*Hrnr*$^{em1(IMPC)Wtsi}$	*Slc16a4*$^{tm2e(EUCOMM)Wtsi}$
Atp5e$^{tm1b(EUCOMM)Wtsi}$	*Ifi27*$^{tm1b(EUCOMM)Wtsi}$	*Slc25a20*$^{tm1a(EUCOMM)Wtsi}$
Atp5f1$^{tm1b(EUCOMM)Wtsi}$	*Ifitm6*$^{tm1b(EUCOMM)Wtsi}$	*Slc25a28*$^{tm1b(EUCOMM)Wtsi}$
Atp8b2$^{tm1a(KOMP)Wtsi}$	*Ifnar1*$^{tm2a(EUCOMM)Wtsi}$	*Slc38a2*$^{tm1a(KOMP)Wtsi}$
Atxn10$^{tm1b(KOMP)Wtsi}$	*Ifnlr1*$^{tm1a(EUCOMM)Wtsi}$	*Slc5a7*$^{tm1a(KOMP)Wtsi}$
Atxn3$^{tm1a(KOMP)Wtsi}$	*Ift140*$^{tm1a(KOMP)Wtsi}$	*Slc9a3r2*$^{tm2a(EUCOMM)Hmgu}$
Bach2$^{tm1a(EUCOMM)Wtsi}$	*Il1r2*$^{tm1a(EUCOMM)Wtsi}$	*Slitrk4*$^{tm1b(KOMP)Wtsi}$
Bai1$^{tm2a(EUCOMM)Wtsi}$	*Il23r*$^{tm2a(EUCOMM)Wtsi}$	*Slu7*$^{tm1a(KOMP)Wtsi}$
Bap1$^{tm1a(EUCOMM)Hmgu}$	*Il27*$^{tm1b(EUCOMM)Wtsi}$	*Slx4ip*$^{tm1a(EUCOMM)Wtsi}$
Barhl1$^{tm1(EGFP\_CreERT2)Wtsi}$	*Irak1*$^{tm1b(EUCOMM)Hmgu}$	*Smg9*$^{tm1b(EUCOMM)Wtsi}$
Bivm$^{tm1b(KOMP)Wtsi}$	*Irf5*$^{tm1e(EUCOMM)Wtsi}$	*Smpd4*$^{tm2b(KOMP)Wtsi}$
Bnip2$^{tm1b(EUCOMM)Wtsi}$	*Izumo1r*$^{tm2a(KOMP)Wtsi}$	*Snx31*$^{tm1a(KOMP)Wtsi}$
Bpgm$^{tm1a(KOMP)Wtsi}$	*Josd1*$^{em1(IMPC)Wtsi}$	*Snx8*$^{tm2a(EUCOMM)Hmgu}$
Bpifb1$^{tm1e(KOMP)Wtsi}$	*Kat2b*$^{em1(IMPC)Wtsi}$	*Spata25*$^{tm1(KOMP)Wtsi}$
Bpifb5$^{tm2a(KOMP)Wtsi}$	*Kcnh4*$^{tm1b(KOMP)Wtsi}$	*Spink14*$^{tm1e(KOMP)Wtsi}$
Brd2$^{em1(IMPC)Wtsi}$	*Kera*$^{em1(IMPC)Wtsi}$	*Sqle*$^{tm1a(EUCOMM)Wtsi}$
Camkmt$^{tm1b(EUCOMM)Wtsi}$	*Kif13b*$^{tm1b(EUCOMM)Wtsi}$	*Srsf7*$^{tm1a(EUCOMM)Wtsi}$
Camsap3$^{tm1a(EUCOMM)Wtsi}$	*Kif18b*$^{tm1a(EUCOMM)Wtsi}$	*Ssr2*$^{tm1b(EUCOMM)Wtsi}$
Capn11$^{tm1b(EUCOMM)Wtsi}$	*Kif1bp*$^{tm1a(KOMP)Wtsi}$	*Stard8*$^{tm1b(EUCOMM)Wtsi}$
Capza2$^{tm1b(KOMP)Wtsi}$	*Kif24*$^{tm1b(KOMP)Wtsi}$	*Stau2*$^{tm1a(EUCOMM)Wtsi}$
Card9$^{tm1a(EUCOMM)Hmgu}$	*Kif3b*$^{tm1b(EUCOMM)Wtsi}$	*Stxbp4*$^{tm1a(EUCOMM)Wtsi}$
Casc4$^{tm2b(EUCOMM)Wtsi}$	*Klc2*$^{tm1e(EUCOMM)Wtsi}$	*Sult1c1*$^{tm1b(KOMP)Wtsi}$
Catip$^{tm1b(KOMP)Wtsi}$	*Klf17*$^{tm1b(KOMP)Wtsi}$	*Supt3*$^{tm1a(EUCOMM)Hmgu}$
Cbr2$^{tm1b(EUCOMM)Hmgu}$	*Klhl18*$^{tm1a(KOMP)Wtsi}$	*Supt5*$^{tm2a(KOMP)Wtsi}$
Ccdc127$^{tm1b(EUCOMM)Wtsi}$	*Klhl30*$^{tm1a(KOMP)Wtsi}$	*Tbc1d22a*$^{tm1b(KOMP)Wtsi}$
Ccdc159$^{tm1a(KOMP)Wtsi}$	*Klk5*$^{tm2a(KOMP)Wtsi}$	*Tceal5*$^{tm1b(KOMP)Wtsi}$
Ccdc18$^{tm1a(EUCOMM)Wtsi}$	*Klk6*$^{em1(IMPC)Wtsi}$	*Tcf7l2*$^{tm1a(EUCOMM)Wtsi}$
Ccdc69$^{tm1b(KOMP)Wtsi}$	*Klrb1a*$^{tm1a(KOMP)Wtsi}$	*Tchp*$^{tm1a(EUCOMM)Wtsi}$
Ccdc6$^{em1(IMPC)Wtsi}$	*Krt31*$^{tm1e(KOMP)Wtsi}$	*Tcp11*$^{tm1a(EUCOMM)Wtsi}$

Cdkn2aipnl$^{tm1b(KOMP)Wtsi}$	*Krt7*$^{tm1b(KOMP)Wtsi}$	*Tctex1d2*$^{tm1e(EUCOMM)Wtsi}$
Celf4$^{tm1a(EUCOMM)Wtsi}$	*Krt83*$^{tm1b(KOMP)Wtsi}$	*Tead3*$^{tm1a(EUCOMM)Wtsi}$
Cenpl$^{tm1b(EUCOMM)Wtsi}$	*L3mbtl2*$^{tm2a(EUCOMM)Wtsi}$	*Tent5c*$^{tm1b(KOMP)Wtsi}$
Cep250$^{tm1a(EUCOMM)Wtsi}$	*Lars*$^{tm1b(KOMP)Wtsi}$	*Tet1*$^{tm1a(KOMP)Wtsi}$
Cfap53$^{em1(IMPC)Wtsi}$	*Lce1m*$^{tm1b(EUCOMM)Wtsi}$	*Tex38*$^{tm1a(KOMP)Wtsi}$
Cfap61$^{tm2a(EUCOMM)Wtsi}$	*Lce3c*$^{tm2a(EUCOMM)Wtsi}$	*Tgfb1i1*$^{tm1b(KOMP)Wtsi}$
Cgrrf1$^{tm1b(KOMP)Wtsi}$****	*Ldhb*$^{tm1b(KOMP)Wtsi}$	*Tgm6*$^{tm1a(KOMP)Wtsi}$
Chd9$^{tm1a(EUCOMM)Wtsi}$	*Ldlrad4*$^{tm1b(EUCOMM)Wtsi}$	*Timeless*$^{tm1b(EUCOMM)Hmgu}$
Chil4$^{tm1b(EUCOMM)Hmgu}$	*Leo1*$^{tm1a(EUCOMM)Wtsi}$	*Timmdc1*$^{tm1b(EUCOMM)Wtsi}$
Chmp6$^{tm1b(KOMP)Wtsi}$	*Leprot*$^{tm2b(KOMP)Wtsi}$	*Tmc3*$^{tm2b(KOMP)Wtsi}$
Chst11$^{tm1a(KOMP)Wtsi}$	*Lmna*^{G609G}***	*Tmem110*$^{tm2b(KOMP)Wtsi}$
Chtop$^{tm1a(EUCOMM)Wtsi}$	*Lonrf3*$^{tm1b(KOMP)Wtsi}$	*Tmem126a*$^{tm1a(EUCOMM)Wtsi}$
Cir1$^{tm3a(KOMP)Wtsi}$	*Lpxn*$^{tm1b(EUCOMM)Hmgu}$	*Tmem127*$^{tm1(KOMP)Wtsi}$
Clpp$^{tm1a(EUCOMM)Wtsi}$	*Lrmp*$^{tm1b(EUCOMM)Wtsi}$	*Tmem18*$^{tm1b(EUCOMM)Wtsi}$
(Cluster5N1)$^{(tm1)Brd}$*	*Lrrc23*$^{tm1a(EUCOMM)Wtsi}$	*Tmem241*$^{tm1b(EUCOMM)Wtsi}$
(ClusterXN1)$^{tm1(Brd)}$*	*Lrrc71*$^{tm1a(KOMP)Wtsi}$	*Tmem254b*$^{tm1a(KOMP)Wtsi}$
Cmbl$^{tm1b(KOMP)Wtsi}$	*Lrrc8d*$^{tm1a(EUCOMM)Wtsi}$	*Tmem30a*$^{tm1a(KOMP)Wtsi}$
Cmtm5$^{tm1a(KOMP)Wtsi}$	*Lyplal1*$^{tm1a(KOMP)Wtsi}$	*Tmem37*$^{tm1a(EUCOMM)Wtsi}$
Cnbd1$^{tm1b(EUCOMM)Wtsi}$	*Lyrm9*$^{tm1a(KOMP)Mbp}$	*Tmem42*$^{tm1b(KOMP)Wtsi}$
Cnot4$^{tm1b(EUCOMM)Wtsi}$	*Macrod1*$^{em1(IMPC)Wtsi}$	*Tomm20l*$^{tm1b(EUCOMM)Wtsi}$
Cog6$^{tm1a(EUCOMM)Wtsi}$	*Mamstr*$^{tm1b(EUCOMM)Wtsi}$	*Traf2*$^{tm1a(EUCOMM)Wtsi}$
Col24a1$^{tm1b(EUCOMM)Wtsi}$	*Mast2*$^{tm1a(KOMP)Wtsi}$	*Traf6*$^{tm2a(EUCOMM)Wtsi}$
Col4a3bp$^{tm1a(KOMP)Wtsi}$	*Mau2*$^{tm1b(KOMP)Wtsi}$	*Trappc10*$^{tm1b(KOMP)Wtsi}$
Coro6$^{tm1e(EUCOMM)Wtsi}$	*Mbd1*$^{em1(IMPC)Wtsi}$	*Trappc9*$^{tm1a(EUCOMM)Wtsi}$
Cpgi81$^{tm1.1(NCC)WCS}$*	*Mbl2*$^{em1(IMPC)Wtsi}$	*Trem1*$^{tm1(KOMP)Vlcg}$
Cpsf3$^{tm1b(EUCOMM)Wtsi}$	*Mcf2l*$^{tm1a(EUCOMM)Hmgu}$	*Trim21*$^{em1(IMPC)Wtsi}$
Cpt2$^{tm1b(KOMP)Wtsi}$	*Med22*$^{tm1a(EUCOMM)Wtsi}$	*Trim25*$^{tm2b(EUCOMM)Hmgu}$
Crim1$^{em1(IMPC)Wtsi}$	*Med23*$^{em1(IMPC)Wtsi}$	*Trim56*$^{tm1a(EUCOMM)Wtsi}$
Crlf3$^{em1(IMPC)Wtsi}$	*Medag*$^{tm2b(KOMP)Wtsi}$	*Trim65*$^{tm1b(KOMP)Wtsi}$
Crls1$^{tm1a(EUCOMM)Wtsi}$	*Metrnl*$^{tm1b(KOMP)Wtsi}$	*Trmt2a*$^{tm2b(EUCOMM)Wtsi}$
Csmd1$^{em1(IMPC)Wtsi}$	*Mettl24*$^{tm1a(KOMP)Wtsi}$	*Trp53rkb*$^{tm1a(EUCOMM)Wtsi}$
Csnk1g3$^{tm1a(EUCOMM)Wtsi}$	*Mgat4c*$^{tm1a(EUCOMM)Wtsi}$	*Trub2*$^{tm2a(EUCOMM)Wtsi}$
Ctr9$^{tm1b(EUCOMM)Wtsi}$	*Mir32*$^{(tm1)Brd}$	*Tuba3a*$^{tm1b(KOMP)Wtsi}$

Cttnbp2$^{tm1b(KOMP)Wtsi}$	*Mir96*$^{tm2.2(IMPC)Wtsi}$	*Tuft1*$^{tm1a(KOMP)Wtsi}$
Cutal$^{tm1a(EUCOMM)Wtsi}$	*Mir122*$^{(tm1)Brd}$	*Ube2d1*$^{tm3e(EUCOMM)Wtsi}$
Cxcr1$^{tm1a\ (EUCOMM)Wtsi}$	*Mir210*$^{(tm1)Brd}$	*Ubxn10*$^{tm1b(EUCOMM)Wtsi}$
Cxcr2$^{tm1a(EUCOMM)Wtsi}$	*Mir211*$^{(tm1)Brd}$	*Uevld*$^{tm1a(EUCOMM)Wtsi}$
Cyp2b13$^{tm1b(KOMP)Wtsi}$	*Mir342*$^{(tm1)Brd}$	*Umodl1*$^{tm1a(KOMP)Wtsi}$
Cyp2r1$^{tm1b(EUCOMM)Wtsi}$	*Mkrn2*$^{tm1b(KOMP)Wtsi/em1(IMPC)Wtsi}$**	*Uri1*$^{tm1a(EUCOMM)Wtsi}$
D630023F18Rik$^{tm1b(KOMP)Wtsi}$	*Mospd1*$^{tm1a(KOMP)Wtsi}$	*Usp11*$^{tm1(KOMP)Wtsi}$
D6Wsu163e$^{tm1b(EUCOMM)Wtsi}$	*Mpg*$^{tm1a(EUCOMM)Wtsi}$	*Usp20*$^{tm1a(EUCOMM)Hmgu}$
D7Ertd443e$^{tm2a(KOMP)Wtsi}$	*Mrm1*$^{tm2a(EUCOMM)Wtsi}$	*Usp30*$^{tm2b(EUCOMM)Hmgu}$
D930028M14Rik$^{tm1a(EUCOMM)Wtsi}$	*Mroh4*$^{tm1b(KOMP)Wtsi}$	*Usp37*$^{em1(IMPC)Wtsi}$
Dact3$^{tm1b(KOMP)Wtsi}$	*Mroh9*$^{tm1a(EUCOMM)Wtsi}$	*Usp5*$^{tm1a(EUCOMM)Hmgu}$
Daf2$^{tm1a(KOMP)Wtsi}$	*Mrps21*$^{tm1e(EUCOMM)Wtsi}$	*Vamp3*$^{tm2b(EUCOMM)Wtsi}$
Dap$^{tm1a(KOMP)Mbp}$	*Mrps5*$^{tm1b(EUCOMM)Wtsi}$	*Vps13a*$^{tm1b(EUCOMM)Wtsi}$
Dapk2$^{tm1b(EUCOMM)Wtsi}$	*Mybphl*$^{tm1b(KOMP)Wtsi}$	*Vps33b*$^{tm1a(EUCOMM)Wtsi}$
Dbn1$^{tm1b(KOMP)Wtsi}$	*Myh7b*$^{tm1a(KOMP)Wtsi}$	*Vps51*$^{tm1a(KOMP)Wtsi}$
Dcaf11$^{tm1a(KOMP)Wtsi}$	*Myo10*$^{tm2(KOMP)Wtsi}$	*Vps72*$^{tm1a(EUCOMM)Wtsi}$
Dcbld2$^{tm1a(KOMP)Wtsi}$	*Myo9a*$^{tm1b(EUCOMM)Wtsi}$	*Vwa3a*$^{tm1b(KOMP)Wtsi}$
Dcdc2b$^{tm1b(KOMP)Wtsi}$	*N6amt2*$^{tm1a(EUCOMM)Wtsi}$	*Wac*$^{tm1b(EUCOMM)Wtsi}$
Dclk1$^{tm1a(EUCOMM)Wtsi}$	*Nacc2*$^{tm2b(EUCOMM)Wtsi}$	*Washc2*$^{tm2b(KOMP)Wtsi}$
Dcn$^{em1(IMPC)Wtsi}$	*Nadk2*$^{tm1b(EUCOMM)Wtsi}$	*Wdr89*$^{tm1a(KOMP)Wtsi}$
Dctn4$^{em1(IMPC)Wtsi}$	*Nat10*$^{tm1a(KOMP)Wtsi}$	*Wdtc1*$^{tm1a(KOMP)Wtsi}$
Ddah1$^{tm2a(EUCOMM)Wtsi}$	*Ncf2*$^{tm1a(EUCOMM)Wtsi}$	*Wnt16*$^{tm2b(EUCOMM)Wtsi}$
Ddx42$^{tm1b(EUCOMM)Wtsi}$	*Ndufb8*$^{tm1a(EUCOMM)Wtsi}$	*Wrap53*$^{tm1b(EUCOMM)Wtsi}$
Ddx51$^{tm1a(KOMP)Wtsi}$	*Nebl*$^{tm1b(EUCOMM)Wtsi}$	*Xkrx*$^{tm1b(EUCOMM)Wtsi}$
Defb14$^{tm1b(KOMP)Wtsi}$	*Nek3*$^{tm1b(EUCOMM)Wtsi}$	*Xpnpep1*$^{tm1a(KOMP)Wtsi}$
Defb22$^{tm1a(KOMP)Wtsi}$	*Nek9*$^{tm1a(EUCOMM)Wtsi}$	*Xxylt1*$^{tm1a(EUCOMM)Hmgu}$
Defb30$^{tm2b(KOMP)Wtsi}$	*Nelfe*$^{tm1a(EUCOMM)Wtsi}$	*Ydjc*$^{tm1(KOMP)Wtsi}$
Dennd1b$^{tm1a(EUCOMM)Hmgu}$	*Nfkbil1*$^{tm1a(KOMP)Wtsi}$	*Yipf7*$^{tm1e(KOMP)Wtsi}$
Dennd1c$^{tm1b(EUCOMM)Wtsi}$	*Nhlrc2*$^{tm1a(KOMP)Wtsi}$	*Ypel4*$^{tm1a(EUCOMM)Wtsi}$
Dennd4c$^{tm1b(EUCOMM)Wtsi}$	*Nipsnap3a*$^{tm1b(KOMP)Wtsi}$	*Zbed5*$^{tm1b(EUCOMM)Wtsi}$
Denr$^{tm1b(KOMP)Wtsi}$	*Nme4*$^{tm1a(EUCOMM)Wtsi}$	*Zfp182*$^{tm1b(KOMP)Wtsi}$
Dffb$^{em1(IMPC)Wtsi}$	*Nmrk1*$^{tm1a(KOMP)Wtsi}$	*Zfp239*$^{tm1b(KOMP)Wtsi}$
Dhodh$^{tm1b(EUCOMM)Wtsi}$	*Npat*$^{tm1b(EUCOMM)Wtsi}$	*Zfp266*$^{tm1b(EUCOMM)Wtsi}$

Dhps$^{tm2a(EUCOMM)Wtsi}$	*Nrbp1*$^{tm3b(EUCOMM)Wtsi}$	*Zfp287*$^{tm1b(EUCOMM)Wtsi}$
Dhx33$^{tm1b(KOMP)Wtsi}$	*Nrde2*$^{tm2a(KOMP)Wtsi}$	*Zfp341*$^{tm1a(KOMP)Wtsi}$
Dhx35$^{tm1b(EUCOMM)Wtsi}$	*Nudt12*$^{tm1a(KOMP)Wtsi}$	*Zfp365*$^{tm1a(KOMP)Wtsi}$
Dip2a$^{tm2b(KOMP)Wtsi}$	*Nup85*$^{tm1a(KOMP)Wtsi}$	*Zfp408*$^{tm1b(EUCOMM)Wtsi}$
Dlg3$^{tm1a(EUCOMM)Wtsi}$	*Nutm2*$^{tm2b(EUCOMM)Wtsi}$	*Zfp616*$^{tm1b(KOMP)Wtsi}$
Dlg4$^{tm1e(EUCOMM)Wtsi}$	*Nxn*$^{tm1b(EUCOMM)Wtsi}$	*Zfp658*$^{tm1b(EUCOMM)Wtsi}$
Dlk1$^{em1(IMPC)Wtsi}$	*Oaf*$^{tm1a(EUCOMM)Wtsi}$	*Zfp719*$^{tm1a(EUCOMM)Wtsi}$
Dmgdh$^{tm1a(KOMP)Wtsi}$	*Oog2*$^{tm1a(EUCOMM)Wtsi}$	*Zfp719*$^{tm1b(EUCOMM)Wtsi}$
Dnah17$^{tm1e(KOMP)Wtsi}$	*Orc1*$^{tm1a(KOMP)Wtsi}$	*Zfp763*$^{em1(IMPC)Wtsi}$
Dnajc8$^{tm1b(KOMP)Wtsi}$	*Os9*$^{tm1a(EUCOMM)Wtsi}$	*Zfp791*$^{tm1a(KOMP)Wtsi}$
Dnase1l2$^{tm1.1(KOMP)Wtsi}$	*Osbpl3*$^{tm1a(EUCOMM)Wtsi}$	*Zfp84*$^{tm1b(KOMP)Wtsi}$
Dnmt3a$^{tm1a(KOMP)Wtsi}$	*Otud7b*$^{tm1b(EUCOMM)Wtsi}$	*Zfp879*$^{tm2b(KOMP)Wtsi}$
Dnpep$^{tm1e(EUCOMM)Wtsi}$	*Pam16*$^{tm1b(EUCOMM)Wtsi}$	*Zfyve28*$^{tm1b(EUCOMM)Wtsi}$
Dph6$^{tm1a(KOMP)Wtsi}$	*Pced1a*$^{tm1b(EUCOMM)Wtsi}$	*Zranb1*$^{tm1a(EUCOMM)Hmgu}$
Dpm1$^{tm1b(KOMP)Wtsi}$		

* Knockouts of multi-gene or regulatory regions:

Cluster 5N1: mmu-mir-25 (ENSMUSG00000065394), mmu-mir-93 (ENSMUSG00000065527), mmu-mir-106b (ENSMUSG00000065514)

ClusterXN1: ENSMUSG00000070106, ENSMUSG00000065613 ENSMUSG00000065473, ENSMUSG00000076041 ENSMUSG00000077111, ENSMUSG00000065456

Cpgi81: CpG island 81, Chr1:23255875-23257106 bp

** More than one mouse line has been phenotyped for these genes.

*** The Lmna allele is not an IMPC allele and has been described previously[62].

**** The Cgrrf1 ko strain has a mixed C57BL/6N; C57BL/6NTac background.

Supplementary Table 5: Key resources

REAGENT or RESOURCE	SOURCE	IDENTIFIER
Antibodies		
CD3ε Functional grade purified, clone eBio500A2	eBioscience	16-0033-86; RRID: AB_842782
CD3ε BV421, clone 145-2C11	BD Biosciences	562600
CD3ε BV785, clone 145-2C11	BioLegend UK Ltd	100232
CD4 PE, clone RM4-5	BioLegend UK Ltd	00511; RRID: AB_312714
CD4 BV510, clone RM4-5	BioLegend UK Ltd	100553 RRID:AB_2561388
CD4 BV786, clone RM4-5	BD Biosciences	563331
CD5 APC, clone 53-7.3	BD Biosciences	550035
CD5 BV510, clone 53-7.3	BD Biosciences	563069
CD8a APC, clone 53-6.7	BioLegend UK Ltd	100712; RRID: AB_312750
CD8α AF700, clone 53-6.7	BD Biosciences	557959
CD8α APC-H7, clone 53-6.7	BD Biosciences	560182 RRID:AB_1645237
CD11b BV510, clone M1/70	BioLegend UK Ltd	101245
CD11b PE-Cy7, clone M1/70	BioLegend UK Ltd	101216 RRID:AB_312799
CD11c BV786, clone HL3	BD Biosciences	563735
CD19 BV421, clone ID3	BD Biosciences	562701
CD19 PE-CF594, clone ID3	BD Biosciences	562291 RRID:AB_11154223
CD19 PECY7, clone ID3	BD Biosciences	552854
CD21/35 FITC, clone 7G6	BD Biosciences	553818
CD21/35 PE, clone 7G6	BD Biosciences	552957
CD23 BV421, clone B3B4	BD Biosciences	562929
CD24 APC, clone M1/69	BD Biosciences	562349
CD25 APC, clone PC61	BD Biosciences	557192
CD25 PE, clone PC61	BioLegend UK Ltd	102008 RRID:AB_312857
CD28 Functional grade purified, clone 37.51	eBioscience	16-0281-86;RRID: AB_468923
CD43 PerCP-Cy5.5	BioLegend UK Ltd	121224
CD44 FITC, clone 1B11	BD Biosciences	553133
CD44 FITC, clone IM7	BD Biosciences	561859 RRID:AB_10894581
CD45 Alexa 700, clone 30-F11	BioLegend UK Ltd	103128 RRID:AB_493715
CD45 e450, clone 30-F11	eBioscience	48-0451-82
CD45 eVolve™ 605 (Qdot), clone 30-F11	eBioscience	83-0451-42
CD45 eFluor450, clone 30-F11	eBioscience	48-0451-82
CD45R (B220) PeCY7, clone RA3-6B2	BioLegend UK Ltd	103222

CD45R (B220) AF700, clone RA3-6B2	BD Biosciences	557957
CD62L PE-CF594, clone MEL-14	BD Biosciences	562404 RRID:AB_11154046
CD62L PerCP Cy5.5, clone MEL-14	BD Biosciences	560513
CD86 PECY7, clone GL1	BD Biosciences	560582
CD95 PECY7, clone Jo2	BD Biosciences	557653
CD103 PE, M290	BD Biosciences	557495
CD115 APC, clone AF598	BioLegend UK Ltd	135510 RRID:AB_2085221
CD138 BV650, clone 281-2	BioLegend UK Ltd	142517
CD161 (NK1.1) BV421, clone PK136	BioLegend UK Ltd	108732 RRID:AB_2562218
CD161 (NK1.1) BV650, clone PK136	BioLegend UK Ltd	108736
CD317 BV650, clone 927	BioLegend UK Ltd	127019
F4/80 PerCP-Cy5.5, clone BM8	BioLegend UK Ltd	123128
Fc block	BD Biosciences	553142
GITR PE, clone DTA-1	BD Biosciences	558119
GL-7 AF647, clone GL7	BD Biosciences	561529
Gr-1 AF700, clone RB6-8C5	BioLegend UK Ltd	108422
Ig HRP, polyclonal	Dako	P0447
IgG (H+L) FITC, polyclonal	Invitrogen	626511
IgG1 HRP, clone X56	BD Biosciences	559626
IgG2a HRP, clone R19-15	BD Biosciences	553391
IgD BV510, clone 11-26c.2a	BD Biosciences	563110
IgD PerCP-Cy5.5, clone 11-26c.2a	BioLegend UK Ltd	405710
IgD AF488, clone 11-26c.2a	BioLegend UK Ltd	405718
IgG1 PE, clone A85-1	BD Biosciences	550083
IgM BV42, clone RMM-1	BioLegend UK Ltd	406518
IgM BV786, clone R6-60.2	BD Biosciences	564028
KLRG1 BV421, clone 2F1	BD Biosciences	562897
KLRG1 PE-Cy7, clone 2F1	BioLegend UK Ltd	138416 RRID:AB_2561736
Ly-51 PE, clone BP-1	BD Biosciences	553735
Ly6B FITC, clone 7/4	AbD Serotec	MCA771FB RRID:AB_324596
Ly6C AF700, clone AL-21	BD Biosciences	561237
Ly6C PerCP-Cy5.5, clone HK1.4	BioLegend UK Ltd	128012 RRID:AB_1659241
Ly6G APC, clone 1A8	BD Biosciences	560599
Ly6G V450, clone 1A8	BD Biosciences	560603 RRID:AB_1727564
MHC II I-A/I-E PE, clone M5/114.15.2	BioLegend UK Ltd	107608 RRID:AB_313323
MHC II I-A/I-E AF647, clone M5/114.15.2	BioLegend UK Ltd	107618
MHC II I-A/I-E FITC, 2G9	BD Biosciences	553623
MHC II I-A/I-E AF647, clone M5/114.15.2	BioLegend UK Ltd	107618

Vγ5 (aka Vγ3) FITC, clone 536	BD Biosciences	553229
TCRβ PerCP-Cy5.5, clone H57-597	BioLegend UK Ltd	109228 RRID:AB_1575173
TCRδ PE CY7, clone GL3	BioLegend UK Ltd	118124
TCRδ APC, clone GL3	BioLegend UK Ltd	118116 RRID:AB_1731813
Chemicals, Peptides, and Recombinant Proteins		
10mM HEPES	Life Signalling Technologies	15630056
Collagenase	Sigma Aldrich - Roche	11088858001
DNAase	Sigma	DN25
RBC lysis buffer	eBioscience	00-4300-54
EDTA (0.5 M), pH 8.0	Life Technologies	AM9261
Prolong Gold Mounting Medium	New England Biolabs	9071S
Zombie NIR Fixable Viability Kit	Biolegend	423106
BD FACSDiva CS&T Research Beads	BD Biosciences	655051
Ammonium thiocyanate	Sigma	A7149-100G
Nair™ moisturizing hair removal cream	Church & Dwight Co.	N/A
Acetone	VWR	20067-320
Fetal Bovine Serum	Gibco	FBS
Fetal Bovine Serum	Hyclone laboratories - Biosera	FB-1001/500
RPMI 1640	GIBCO - life technologies	21875034
RPMI 1640 (no phenol red)	GIBCO - life technologies	32404014
PBS 10x (neg for CA2+ and Mg2+)	Gibco	14200-067
PBS 10x (with calcium & Magnesium)	Gibco	14080-048
PBS, D'Beccos	GIBCO - life technologies	14190094
D-MEM (HG)	GIBCO - life technologies	41966029
DPBS	Sigma-Aldrich	D8662
Water	Sigma-Aldrich	W3500
Mounting Medium Dropper Vial 5mL	A. Menarini Diagnostics Ltd.	38015
2-mercaptoethanol	GIBCO Invitrogen	31350010
L-Glutamine	GIBCO Invitrogen	25030024

Recombinant murine IL-2	Peprotech	212-12-100
Penicillin/Streptomycin	Sigma-Aldrich	P4333
Sodium Pyruvate MEM	Sigma-Aldrich	11360039
Dextran sulfate, sodium salt	Affymetrix, Inc.	14489; CAS# 9011-18-1
Formaldehyde 4% solution	VWR international ltd	9713.5000
BSA	Sigma-Aldrich	A9056
Sigmafast	Sigma-Aldrich	P9187
LB	Oxoid	CM1018
Ampicillin	Roche	10 835 242 001
Tween 20	Sigma-Aldrich	P1379
Critical Commercial Assays		
Zenit ANA HEp-2 Cells (12 wells)	A. Menarini Diagnostics Ltd.	37806
FITC – QC Slide	A. Menarini Diagnostics Ltd.	38015
Cytotox 96 non-radioactive assay	Promega UK Ltd	G1780
Deposited Data		
3i statistical analysis	This study	www.immunophenotype.org
Raw and analyzed data	This study	www.immunophenotype.org
Experimental Models: Cell Lines		
P815 mastocytoma cell line	ATTC	TIB-64
HEp-2 cell lines, coated on slides	A. Menarini Diagnostics Ltd.	37806
Experimental Models: Organisms/Strains		
C57BL/6N wild type control mice	WTSI	
Knockout mouse strains as detailed in **Table S4**	WTSI	
Salmonella typhimurium M525 :: TetC	Gordon Dougan, WTSI	
Trichuris muris	Richard Grencis, University of Manchester	
Equipment		

Scil Vetabc hematology analyser	Horiba	http://www.horiba.com/uk/medical/products/animal-healthcare/haematology/scil-vet-abc-details/scil-vet-abc-12687/
BD LSR II flow cytometer (Blood)	BD Biosciences	RRID:SCR_002159; http://www.rockefeller.edu/fcrc/pdf/BD_LSRII_Brochure_SJ-0142-00.pdf
BD LSR Fortessa X-20 (Spleen, MLN, and bone marrow)	BD Biosciences	http://www.bdbiosciences.com/us/instruments/research/cell-analyzers/bd-lsrfortessa-x-20/m/1519232/overview
Leica SP2 confocal microscopes, 40x 1.25 NA oil immersion lens and 405 nm, 488 nm and 633 nm lasers (Ear epidermis)	Leica	https://www.leica-microsystems.com/products/confocal-microscopes/details/product/leica-tcs-sp2/
Leica SP5 confocal microscopes, 40x 1.25 NA oil immersion lens and 405 nm, 488 nm and 633 nm lasers (ear epidermis)	Leica	https://www.leica-microsystems.com/products/confocal-microscopes/details/product/leica-tcs-sp5/
Nikon wide-field TE2000U Microscope (ANA)	Nikon	TE2000U
Deltavision Elite widefield system based on an Olympus microscope, LED light source and CoolSNAP HQ2 camera (ANA)	GE Healthcare Life Sciences, Olympus	https://www.gelifesciences.com/en/us/shop/deltavision-elite-high-resolution-microscope-p-04420
Zeiss AxioPlan Microscope with a Plan Neofluar 5x/0.15 Ph1 objective and Moti Cam 10 camera (DSS)	Zeiss	https://www.zeiss.com/microscopy/int/home.html?gclid=EAIaIQobChMIj7KRv-mH4QIVybHtCh0C3w_OEAAYASAAEgJ2afD_BwE
Software and Algorithms		
R version 3.3.1 -3.5.2 and general data analysis packages (data.table, ggplot2, dplyr, igraph, MASS)	The R project for statistical computing	www.r-project.org

PhenStat_2.8 org.Hs.eg.db org.Mm.eg.db	BioConductor	www.bioconductor.org
RStudio 1.0.136	RStudio	https://www.rstudio.com
R code for reference range analysis, assessment of false positive rate	Anna Lorenc	https://github.com/AnnaLorenc/3i_heatmapping available on request
Flow Jo v1.10	Treestar	RRID:SCR_008520; http://www.flowjo.com
Cytoscape 3.6.1	Cytoscape	www.cytoscape.org
BD DIVA 7.0	BD Biosciences	RRID:SCR_001456; http://www.bdbiosciences.com/instruments/software/facsdiva/index.jsp
flowClean	Ryan Brinkman	Fletez-Brant et al 2016
UFO	Ryan Brinkman	available on request
flowDensity	Ryan Brinkman	Malek et al 2015
PRISM 6	Graphpad software	http://www.graphpad.com/scientific-software/prism/
Definiens developer	Definiens	www.definiens.com
ANA assay Fiji/ImageJ macro	Katherine Bull	www.immunophenotype.org
ANA assay Python scoring script	Katherine Bull	www.immunophenotype.org
Microsoft Excel 2010	Microsoft	https://www.microsoftstore.com/store/msuk/en_GB/home
Deposited Data		
3i statistical analysis	This study	www.immunophenotype.org
Raw and analyzed data	This study	www.immunophenotype.org
Other		
30 µm CellTrics filters	Partec Cell Trics	04-0042-2316
96 Well Clear V-Bottom Not Treated Polypropylene Microplate, Nonsterile	SLS	353263
Microtube MaxyClear PP clear 1.7 mL (Axygen)	Fisher	12756799
C-Tubes	Miltenyi Biotec	130-096-334
Superfrost R Plus #72, 26x76x1 mm (75 pieces)	VWR	631-0108
Cover Glass 22 x 40 Mm No. 1,5	VWR	631-1370